Structural characterization of epitaxial graphene

Memoria presentada para optar al grado
de Doctor en Ciencias Físicas por
Pablo Merino Mateo

Dirigida por:
Prof. Dr. **José Ángel Martín Gago**

Tutor:
Prof. Dr. **José María Gómez-Rodríguez.**

Madrid, Noviembre del 2014

Departamento de Física de la Materia Condensada y
Nanotecnología.

Universidad Autónoma de Madrid

"Hasta el infinito y mas allá"
B. Lightyear

A mi familia y seres queridos
y a todos los que habéis hecho posible este trabajo

Contents

Resumen

El estudio de grafeno crecido epitaxialmente sobre substratos monocristalinos tiene una doble relevancia: por un lado desde un punto de vista puramente técnico e industrial y por el otro desde el meramente científico. Diferentes substratos han sido propuestos para el crecimiento de láminas de grafeno de alta pureza con vistas a futuras aplicaciones prácticas. Estas aplicaciones abarcan desde membranas para desalinizar el agua hasta electrodos transparentes para pantallas táctiles o transistores de alta frecuencia.

Diferentes substratos han sido propuestos y estudiados para el crecimiento epitaxial de láminas de grafeno con bajo número de defectos. Entre ellos podríamos diferenciar dos subclases: los substratos metálicos y el carburo de silicio. En la presente tesis hemos estudiado ambos casos mediante técnicas avanzadas de caracterización superficial. Para ello ha sido necesario el uso de campanas de ultra alto vacio (UHV, por sus siglas en inglés) donde las muestras monocristalinas una vez preparadas pueden mantener su superficie libre de contaminantes durante un tiempo suficiente como para realizar los experimentos y así poder crecer las capas de grafeno sin injerencias de contaminación involuntarias. El UHV también es un requisito necesario para la mayoría de las técnicas de caracterización utilizadas, tanto técnicas de microscopía de efecto túnel de alta resolución (STM, del inglés) como de espectroscopia de fotoemisión. Los resultados experimentales han sido confrontados con simulaciones de primeros principios mediante el uso del funcional de la densidad electrónica (DFT de las siglas en inglés).

Grafeno sobre Pt(111). En esta tesis hemos elegido como representante de los substratos metálicos la superficie hexagonal (111) de platino. Sobre ella hemos depositado diferentes precursores (moléculas ricas en carbón cuya descomposición resulta en grafeno) para el crecimiento epitaxial de las capas grafénicas. Como precursores moleculares hemos usado tanto pequeños hidrocarburos como grandes moléculas policíclicas aromáticas. La deposición y subsecuente calentamiento a altas temperaturas (típicamente >1100K) de estos precursores resulta típicamente en el crecimiento capas de grafeno policristalino donde coexisten diferentes ángulos entre el grafeno y el substrato. Estos dominios rotacionales forman interferencias electrónicas con el substrato y forman, los llamados, Moirés. Se ha

abordado el estudio de qué rotaciones permitidas sobre el Pt(111) mediante una combinación de medidas de STM y el desarrollo de un modelo fenomenológico que se basa en la búsqueda de las mejores coincidencias entre posiciones atómicas de substrato y grafeno para todos los ángulos.

El modelo predice que existen 22 ángulos preferentes que forman 15 Moirés distintos y distinguibles, asimismo el modelo obtiene para cada ángulo de rotación el ángulo aparente del Moiré resultante – esto es la orientación relativa de la superestructura respecto al substrato- así como su periodicidad. Estos resultados coinciden con las medidas realizadas mediante STM y con las estructuras reportadas en la literatura. De entre todos los posible Moirés hemos estudiado mediante una combinación de imágenes de resolución atómica y simulaciones de DFT las dos estructuras que involucran un menor número de átomos, llamadas $(\sqrt{3}X\sqrt{3})R30^{o}$ y $(\sqrt{7}X\sqrt{7})R19^{o}$ debido a su conmensuración con el substrato.

Para investigar los mecanismos fundamentales que inducen la aparición de un numero finito de posibles Moirés hemos realizado un estudio extensivo de las regiones de enlace entre las islas de grafeno y los escalones de Pt(111). Estas intercaras forman estructuras 1-dimensionales donde los últimos átomos de carbono pertenecientes al grafeno se enlazan químicamente con los átomos de Pt mas exteriores de los escalones monoatómicos del Pt(111). Nuestro análisis sugiere que estas regiones de enlace son uno de los factores que determinan la orientación de las islas de grafeno.

Hemos realizado un estudio detallado de una de estas intercaras, más concretamente la heteroestructura formada entre grafeno con Moiré $(\sqrt{7}X\sqrt{7})R19^{o}$ y escalón monoatómico de Pt(111), para entender en profundidad los mecanismos que aparecen en este tipo de bordes. La comparación entre resultados experimentales y teóricos perfila para esta precisa estructura un escenario donde el grueso del estrés es absorbido en la mitad del Pt mediante la inducción de una compleja reconstrucción cristalina que sitúa algunos de los átomos de Pt muy lejos de sus posiciones “originales”. Sorprendentemente en conjunción con esta reconstrucción también aparecen unos estados electrónicos en el lado del grafeno que se ven constreñidos a una, y solo una, de las dos subredes del grafeno.

Por último, y para finalizar con el estudio de las estructuras de grafeno que aparecen en la superficie de Pt(111) hemos realizado un inventario de

todos los defectos que hemos ido encontrando en nuestras sesiones de STM. Este estudio no entra en detalle y pretende servir de "bestiario" descriptivo desde un punto de vista experimental para futuras investigaciones.

Grafeno sobre SiC(0001). Independientemente de todos estos trabajos, hemos estudiado las propiedades estructurales de las posibles reconstrucciones que aparecen en SiC(0001). Diferentes estructuras superficiales aparecen cuando calentamos este material a altas temperaturas. Una vez las muestras son calentadas a >1500K obtenemos una superficie rica en carbono organizado en hibridación sp^2. Calentamientos a mayores temperaturas inducen la aparición de multicapas (bicapa, tricapa…). En la presente tesis se ha realizado una caracterización exhaustiva del grafeno epitaxialmente crecido sobre SiC(0001).

El grafeno crecido de esta manera presenta propiedades muy similares de aquellas que presentan las muestras exfoliadas de grafito. Esto es una indicación directa de que la interacción del grafeno con el substrato es muy baja. Por este motivo G/SiC(0001) supone un excelente banco de pruebas para racionalizar las interacciones a escala atómica de distintos adsorbatos depositados sobre grafeno y entender las contribuciones debidas a la interacción entre moléculas discriminándolas de la interacción entre adsorbato y substrato. Normalmente la competición entre las interacciones intermoleculares y la interacción van der Waals substrato-adsorbato dirige la dinámica molecular, pero a veces la interacción con el substrato es más fuerte llegando a darse el caso de quimisorción de adsorbatos simples. En estos casos la hibridación de los átomos de carbono del substrato pasa de ser sp^2 a sp^3.

En la presente tesis hemos estudiado mediante técnicas de caracterización superficial y cálculos de primeros principios la adsorción e interacción de adsorbatos modelo con diferente fuerza de interacción adsorbato-substrato. Para ello hemos utilizado sistemas modelos sencillos que expresan independientemente la naturaleza de su interacción. Por un lado hemos estudiado las débilmente unidas moléculas de C_{60} y por el otro los covalentemente unidos átomos de hydrogeno.

Nuestros resultados demuestran que C60/G/SiC(0001) forma islas ordenadas exclusivamente unidas por interacciones van der Waals donde la interacción entre moléculas juega un rol primordial, mientras que el H/G/SiC(0001) quimisorbe encima de los átomos de carbono formando

dímeros, trímeros y pequeños clústeres bidimensionales cuya configuración geométrica está determinada por la red de panal de abejas del substrato. La comparación entre estos dos sistemas ideales revela que la interacción de los adsorbatos sobre grafeno puede ser tuneada en un amplio rango de intensidades desde una atracción mínima hasta un enlace sólido.

SiC en astroquímica. Por último, cabe señalar la motivación original de la presente tesis. Esta tesis surgió como una idea interdisciplinar del Centro de Astrobiología para emplear métodos y técnicas de física de superficies para entender problemas de astroquímica. Así, se trata de de combinar los conocimientos del grupo de investigación ESISNA con los del grupo del Prof. J. Cernicharo para estudiar la formación de moléculas policíclicas aromáticas (PAHs por sus siglas en inglés) en el espacio, más concretamente en el medio circumestelar e interestelar. Las regiones circumestelares de estrellas rojas masivas ricas en carbono son abundantes en granos de polvo de carburo de silicio (SiC). Esto se ha podido detallar mediante espectroscopía rotacional y vibracional usando telescopios terrestres y espaciales. Por otra parte, estas observaciones han revelado un medio interestelar rico en química en fase gas de atmósferas enrarecidas donde moléculas sencillas, tales como el H_2, CO, C_2H_2, HCN… y moléculas sorprendentemente complejas como la glicina (CH_2NH_2COOH), uno de los aminoácidos presentes en nuestros organismos, pueden ser detectadas mediantes este tipo de técnicas observacionales.

Uno de los grandes problemas abiertos en la astroquímica moderna es la extraordinariamente alta abundancia de PAHs. Este tipo de moléculas es considerado responsable de la aparición en los espectros infrarrojos de unas bandas difíciles de identificar de longitudes de onda entre 3 y 25 μm. La abundancia relativa de PAHs no puede ser explicada mediante las teorías actuales (tales como la polimerización acetilénica) debido a la baja frecuencia de colisión en las atmósferas interestelares entre las partículas constituyentes. Nuevos mecanismos de formación de PAHs interestelares son, por lo tanto, necesarios para poder explicar su relativamente alta tasa de presencia.

En la presente tesis proponemos una nueva vía de formación de PAHs basada en la descomposición de las capas de grafeno epitaxial sobre los granos de polvo interestelar de SiC. Los granos de SiC se forman cerca de la fotosfera de las estrellas y se grafitizan debido a las altas temperaturas ocurrentes en estas regiones del espacio. La presencia de hidrógeno atómico -disociado del molecular mediante procesos térmicos y de

fotodisociación ultravioleta- en esas regiones induce una corrosión superficial en las superficies de SiC que produce PAHs de distintos tamaños que posteriormente son eyectados a la fase gas. Todos los pasos de este proceso pueden ser reproducidos en ambientes controlados en tierra mediante campanas de UHV y pueden ser caracterizados mediante técnicas provenientes de la rama de física del estado sólido. Estos resultados abren nuevas líneas de investigación en la síntesis de PAHs y demuestran que determinados problemas de la astroquímica pueden ser abordados desde una metodología de ciencia de superficies.

Abstract

The study of epitaxially grown graphene on monocrystalline substrates posses a double relevance: first from a purely technical and industrial point of view and second from a purely scientific viewpoint. Various substrates have been proposed to grow high purity graphene sheets for future practical applications. These applications range from membranes to desalinate water, transparent electrodes for touchscreens or high-frequency transistors.

Various substrates have been proposed and studied for epitaxial growth of graphene sheets with low number of defects. They can be differentiated in two main subclasses: metal substrates and silicon carbide. In this thesis we have studied both systems using advanced surface characterization techniques. This is why it has been necessary the use of ultra high vacuum chambers (UHV) where, once single crystal samples are prepared, they keep its surface free of contaminants during a time large enough to grow the graphene layers without interference from unintentional contamination. The UHV is also required for most characterization techniques used in this thesis, such as high resolution scanning tunneling microscopy (STM) and photoemission spectroscopy. These experimental results have been confronted with first-principles simulations using the density functional theory (DFT).

Graphene on Pt(111). In this thesis we have chosen as representative of the metal substrates the hexagonal surface (111) of Pt, on which different precursors (i.e. carbon rich molecules whose decomposition results in graphene) have been deposited in order to grow epitaxial layers. We have used both, small hydrocarbons and large polycyclic aromatic molecules for this purpose. Deposition and subsequent heating at elevated temperatures (>1100K) of these precursors typically produces polycrystalline graphene where different angles between the substrate and graphene coexist. These rotational domains produce electronic interferences with the substrate and form the, so-called, Moiré patterns. The problem of which rotations are permitted in the G/Pt(111) system has been addressed in this thesis by a combination of STM images and the use of an original phenomenological model based in the search of the best coincident atomic positions between substrate and graphene for every angle.

The model predicts the existence of 22 preferred angles but only 15 distinguishable Moirés. The model also obtains for every rotation angle the resulting Moiré apparent angle - this is the relative orientation between the superstructure and the substrate- and the periodicity. These results are consistent with the STM measurements and with the structures reported in the literature. Among all the possible Moirés, we have characterized through a combination of atomic-resolution images and DFT simulations the two structures involving fewer number of atoms , namely (√3×√3)R30^{o} and (√7X√7) R19^{o} (like its commensuration with the substrate).

To investigate the fundamental mechanisms conducing to a finite number of stable Moirés we have made an extensive study of the binding regions between graphene islands and the Pt(111) steps. These interfaces consist of one-dimensional structures where the last carbon atoms belonging to graphene chemically bond with the outermost Pt atoms in the monatomic steps of Pt(111). Our analysis suggests that these binding regions are one of the driving factors determining the orientation of the graphene islands.

We conducted a detailed study of these interfaces, and among them, specifically the heterostructure formed between (√7X√7)R19^{o} Moiré and a monatomic Pt (111) step, so we can understand in depth the driving mechanisms appearing in these edges. The comparison between experimental and theoretical results for this precise structure depicts a scenario where most stress is absorbed in the Pt side by inducing a complex crystalline reconstruction that moves some of the Pt atoms far from their "original" positions. Surprisingly, in conjunction with this reconstruction, it also appears exotic electronic states on the graphene side. These states are constrained to one, and only one, of the two sublattices of graphene.

Finally, we finish the study of graphene structures on Pt(111) with an inventory of all the defective structures found during our STM sessions. This study is not as detailed as the previous ones and is intended to serve as a descriptive "bestiary" from an experimental point of view.

Graphene on SiC (0001). We studied the structural properties of all the possible reconstructions appearing on the SiC(0001) surface. Different surface structures appear when heating this material at high temperatures. Once the samples are heated to >1500K we obtain a carbon-rich surface organized in sp2 hybridization. Annealings at higher temperatures induce the appearance of multilayer (bilayer, trilayer...). In this thesis we have

performed a comprehensive characterization of epitaxial graphene grown on SiC(0001).

Graphene grown with this methodology exhibits properties very similar to those of exfoliated samples. This is a direct indication that graphene-SiC interaction is very faint. For this reason G/SiC(0001) seems an excellent testbed where to rationalize the atomic-scale interactions of adsorbates deposited on graphene and for understanding the different contributions arising from the intermolecular and the adsorbate-substrate interactions.

Typically, competition between intermolecular and van der Waals substrate-adsorbate interaction drives the molecular surface structures. However sometimes the interaction with the substrate can be much stronger and some simple adosorbates chemisorb on top of carbon atoms in the graphene lattice. In these cases, hybridization of the carbon atoms within graphene changes from sp^2 to sp^3.

In this thesis we have studied the interaction of adsorbates with graphene by means of surface characterization techniques combined with first principles calculations. We have used simple model systems expressing different strength in its substrate interaction. On one side we have studied the weakly interacting C_{60} molecules and on the other covalently bonded hydrogen atoms.

Our results show that C_{60}/G/SiC forms ordered layers exclusively bound by van der Waals interactions and where intermolecular interactions play an important role while H/G/SiC chemisorbs on top of the C atoms of graphene forming dimmers, trimmers and small clusters with geometrical configurations confined by the honeycomb lattice of the substrate. The comparison between these two ideal systems reveals that the adsorbate-graphene interaction can be tuned over a wide range of intensities from a weakly physisorption to a strong chemisorption.

Astrochemistry and SiC. Finally, it should be noted that the original motivation of this thesis was a surface description of the processes occurring in some regions of the interstellar space. This thesis appears as an interdisciplinary collaboration in the *Centro de Astrobiología* to use the techniques and methodologies of surface science in the understanding of astrochemical problems. In this direction we have put together the efforts of the ESISNA and Prof. J. Cernicharo research groups to investigate the synthesis of polycyclic aromatic hydrocarbons (PAHs) in the space, more

precisely in the circumstellar and interstellar regions. Circumstellar regions near carbon-rich red stars contain silicon carbide (SiC) dust grains. This has been observed by rotational and vibrational infrared spectroscopy using ground and space-based telescopes. On the other side, these observations revealed an interstellar medium rich in gas phase chemistry where simple molecules such as H_2, CO, C_2H_2, and HCN ... are found together with amazingly complex molecules such as glycine (CH_2NH_2COOH), one of the amino-acids present in our bodies.

One of the major problems in modern astrochemistry is the unusually high abundance of PAHs. These molecules are considered responsible for the appearance in the infrared spectra of bands with wavelengths between 3 and 25 microns. PAHs relative abundance cannot be explained by current theories (such as acetylene polymerization) owing to the low collision frequency in interstellar atmospheres. Finding new mechanisms of interstellar PAHs formation is necessary in order to explain the relatively high abundance.

In this thesis we propose a new PAHs formation mechanism from our experimental observations on epitaxial graphene hydrogen etching. SiC grains form near the photosphere of the star and graphitize due to the high temperatures occurring in these regions of space. The presence of atomic hydrogen – dissociated through thermal and ultraviolet photodissociation- in those regions induces corrosion on the SiC surfaces and produces PAHs of different sizes which are subsequently ejected into the gas phase. All the steps of this process can be reproduced in controlled environments with UHV chambers and can be characterized using solid state physics techniques. These results open new research lines in the PAHs synthesis and show that certain astrochemistry problems can be addressed from a surface science methodology.

Introduction and motivation

Nanotechnology, towards a controlled synthesis of new carbon structures

"There´s plenty of room at the bottom"

R. Feynman. December 29, 1959.

In 1959 Prof. Feynman used this sentence during a famous lecture in California to describe the real possibility of reducing the size of the computer circuitry down to its atomic limits. In this talk he speculated with performing atomic scale designed structures. He foresaw the possibility of using advanced methodologies for manipulating individual atoms as a source of performing synthetic chemistry. He even imagined the possible clinical applications of tiny functionalized nanoparticles inside the body used in health treatments. This talk is considered to be one of the earliest discussions about modern nanotechnology concepts. For the first time, the human beings considered the idea of manipulating the matter that surrounds us with atomic precision. These concepts were first pronounced as a dream. Nowadays, although still limited, they have become a real possibility opening an immense field of atomically controlled designs with new and stunning properties. Nowadays Si-based transistors are reaching its fundamental limitations as lithography techniques improve and single atoms (and molecules) are routinely controlled on top of particular atomically precise surfaces in laboratories around the world. The most immediate approach for producing these new nanostructures would be to fabricate them in a top-down approach, as we produce most of the goods that we profit in our everyday life. We can think to start with a macroscopic piece and *sculpting* it down, ideally until the atomic scale, and latter *mount* them together with others in a *nano-assembly-line*.

However, the most fascinating nanostructures that have ever been considered are not designed on purpose by humans but they appeared spontaneously on Earth. Living beings are the result of the sum of atomically precise nanometer scale structures, from DNA to peptides and proteins, that are 98% formed by only four elements: carbon (19.37%), hydrogen (10.0%), oxygen (65.5%) and nitrogen (3.2%). These structures are the result of a bottom-up process of self assembly that naturally

appeared on the surface of the Earth around 4 billion years ago. This strategy has proven to be very versatile for creating a vast inventory of macromolecules with different complex functionalities. If nature itself is capable of creating life out from “mud”, let us imagine what could be done by taking profit of the knowledge of the bottom-up processes of biology but using all the elements and strategies that nature did not have at hand.

Nowadays technologies are far from the fabrication of the on demand bio-functional architectures that R. Feynman envisioned 50 years ago. However some important achievements in the field of the nanotechnology have been developed. The invention of Scanning Tunneling Microscopy (STM) [1] resulted in the first controlled manipulation of single atoms [2] and the first self assembled structures were successfully produced through smart molecular designs [3]. In order to advance in the interdisciplinary field of nanotechnology simple model systems are needed to rationalize the different mechanisms and processes involved in the atomic scale nature. Several different interactions -such as electrostatic, magnetic, van der Waals or chemical bonding- normally appear together and compete on atomic scale systems. The study of model systems put apart the different contributions of the complex behavior of the quantum nature and unveils common behavior patterns across different processes. For this purpose carbon nanostructures are ideal systems of study.

Carbon nanostructures are atomically precise carbon-pure composites with reduced size –one of its dimensions is in the order of the nm-. Carbon nanostructures with different dimensionalities have attracted the attention of the scientific community because their simplicity and exotic properties. We will focus on the structures holding sp^2 hybridization. These structures comprise the 0D family of fullerene molecules [4], the 1D family of carbon nanotubes (CNTs) [5], and the 2D graphenic materials [6]. These atomic configurations have been proven to be stable and experimentally observed and have fostered significant scientific efforts from many branches of the science, such as chemistry, physics, or material science. Moreover. Some of these studies have been recognized with some important scientific prizes; the discovery of fullerenes in 1988 earned to H. Kroto, R. Curl and R. Smalley the Nobel Prize (NP) in Chemistry of the year 1996 and the discovery of graphene in 2004 earned to A. Geim and K. Novoselov the NP in Physics of the year 2010. The present thesis studies from a surface science point of view epitaxial graphene grown on single crystal surfaces.

Graphene: Introduction.

Graphene is a carbon allotrope consisting on an atom-thick single layer mesh ordered in a honeycomb lattice [7]. Its unit cell contains two nonequivalent carbon atoms and therefore in order to be fully described in we need to account for a hexagonal lattice with basis. This particular atomic structure yields graphene extraordinary electronic properties. In **Figure 0 1** we present a ball and stick representation in the real space of the atomic structure of graphene. In this figure we have marked the two lattice vectors and the sublattice "number" (sublattice A and B respectively) of every atom. As one can notice, every carbon atom has three first neighbors corresponding to the opposite sublattice.

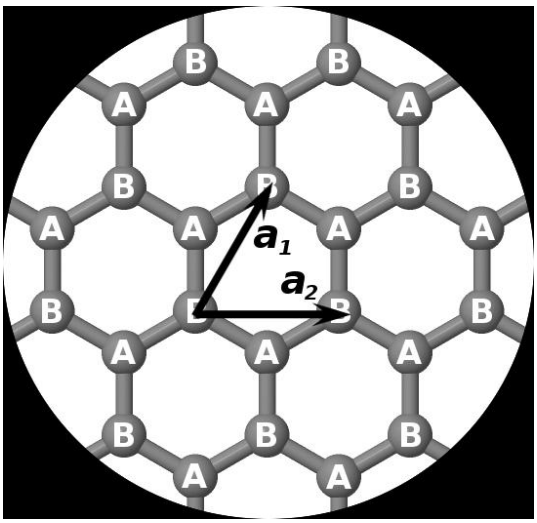

Figure 0 1: *Schematic ball and stick representation of the honeycomb lattice of graphene. The structure consists in two interpenetrating hexagonal lattices.*

The structure of graphene is not a Bravais lattice, it needs to be expressed as an hexagonal lattice with a basis. Choosing the appropriate axis of reference one can express the lattice vectors by the following form.

$$\boldsymbol{a_1} = \frac{a}{2}(3, \sqrt{3}), \qquad \boldsymbol{a_2} = \frac{a}{2}(3, -\sqrt{3})$$

Where $a = 1.42\,\AA$ is the carbon-carbon distance. The reciprocal lattice vectors are then

$$\boldsymbol{b_1} = \frac{2\pi}{3a}(1, \sqrt{3}), \qquad \boldsymbol{b_2} = \frac{2\pi}{3a}(1, -\sqrt{3})$$

This system´s electronic structure result so simple that can be correctly described under the tight binding approach. This calculation was first performed back in 1947 by P.R Wallace. The Hamiltonian for electrons considering that electrons can hop to nearest and near to nearest neighbor atoms under this theoretical treatment can be written as follows (assuming for convenience $\hbar = 1$) [7].

$$H = -t \sum_{\langle i,j\rangle,\sigma} \left(a^{\dagger}_{\sigma,i}\, b_{\sigma,j} + h.c\right) - t' \sum_{\langle\langle i,j\rangle\rangle,\sigma} \left(a^{\dagger}_{\sigma,i}\, a_{\sigma,j} + b^{\dagger}_{\sigma,i}\, b_{\sigma,j} + h.c\right)$$

Where $a_{\sigma,i}$, $a^{\dagger}_{\sigma,i}$ are respectively the annihilation and creation operators with spin σ in the A sublattice, and equivalent definitions for the B sublattice. The hopping parameters for the nearest neighbor electronic jump (hopping between different sublattices) are t=2.8eV and the one for nest nearest neighbors is t´= 0.6 eV. The energy bands can be easily derived from this Hamiltonian and result.

$$E_{\pm}(\boldsymbol{k}) = \pm t\sqrt{3 + f(\boldsymbol{k})} - t' f(\boldsymbol{k})$$

$$f(\boldsymbol{k}) = 2\cos\left(\sqrt{3}k_y a\right) + 4\cos\left(\frac{\sqrt{3}}{2}k_y a\right)\cos\left(\frac{3}{2}k_{xy} a\right)$$

The energy landscape and electron behavior that these equations depict are very interesting. Near the so-called Dirac points the energy dispersion can be considered lineal and therefore the effective mass of the electrons to be zero. These electrons behave as massless Dirac fermions [7]. In **Figure 0 2** we present the graphical representation of $E_{\pm}(\boldsymbol{k})$, and the magnified region of a single Dirac cone.

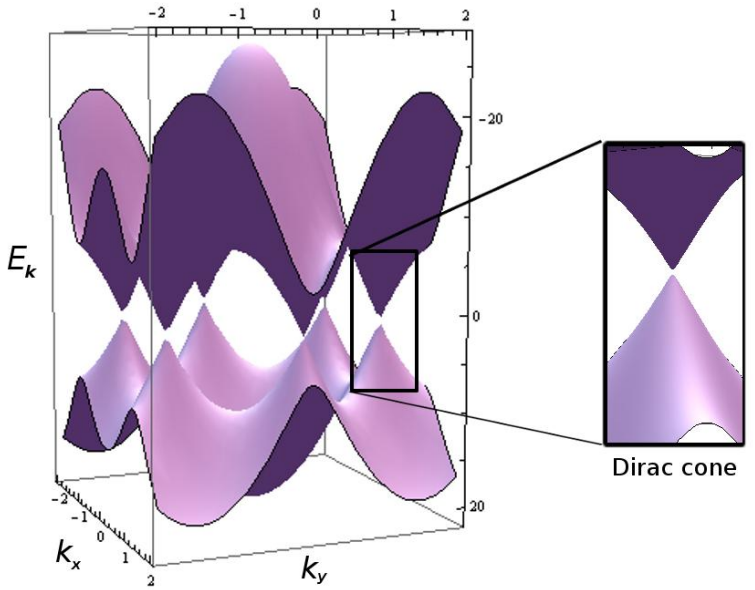

Figure 0 2: *Energy band dispersion for the graphene electronic structure. Right, closer look to the energy band near the k point in the reciprocal space known as Dirac point, and the so-called Dirac cones.*

This electronic structure is unique of 2D honeycomb materials and the resulting massless charge carriers are very interesting from a theoretical point of view as they behave like electrons accelerated to velocities near the light speed. The graphene discoverer A.K. Geim already noticed this behavior and remarked it in its famous sentence: *graphene … allows the investigation of relativistic quantum phenomena in a bench-top experiment* [8].

Graphene first isolation

Graphene was first isolated in 2004 by the group of K. Novoselov and A.K.Geim in Manchester from mechanical exfoliation of highly oriented pyrolytic graphite (HOPG) using a simple Scotch tape for removing the topmost layers of a commercial HOPG sample [6]. This technique is normally used for cleaning the HOPG samples prior to its use as a super-flat substrate and leaves clean fresh surfaces free of involuntary contaminants. Mechanical cleavage of HOPG can also performed in UHV conditions in

order to use the sample for advanced surface characterization. The brilliant idea here, was to look at the remnants attached to the Scotch tape and study its electronic properties. Showing the existence of the first purely 2D system. However, as A.K.Geim itself recognized it was first isolated long before by means of graphite oxidation [9]. The work of G. Ruess and F. Vogt ad later U. Hofmann and H.-P. Boehm on transmission electron microscopy (TEM) analysis of dried graphite oxide droplets in the 1950-1960s was probably the first time that single layer of this material was successfully isolated and studied. Actually the graphene name itself was first introduced by H.-P. Boehm et al. in 1986 deriving it from the word "graphite" and the suffix referring to polycyclic aromatic hydrocarbons "-ene" [9].

Every time we use a pencil it results very likely that we are creating micron-sized graphene crystals. Moreover, single layer graphite was long known in the surface science community as an involuntary contaminant appearing on many materials such as some metallic surfaces [10]. However it was needed that graphene electric properties were first experimentally described in order for all these studies to become relevant. Since graphene was discovered thousands of scientific papers have been devoted to the topic. This new material combined many interesting aspects. The previously discussed massless Dirac fermions, the first pure 2D material ever isolated, the strongest material and one of the best thermal and electrical conductors ever described. Graphene is a superlative material and it has focused the attention of many researchers around the globe.

Graphene production methods.

There are several production methodologies of graphene. Every of them have its advantages and drawbacks. The most important ones are.

-Mechanical exfoliation from highly ordered pyrolytic graphite (HOPG) [6], also known as the Scotch tape technique. This is the method that obtains freestanding samples, however the size and aspect of the samples is not well controlled and the production price is relatively high, as an experimented researcher has to look one by one the by-products of HOPG exfoliation searching for flakes with the precise optical absorbance .

-Epitaxial growth on silicon carbide by thermal annealing [11]. When heating SIC to high temperatures(>1500K) graphitic layers grow on the surface of the samples. This process is induced by Si depletion and C reorganization into the stable sp^2 adlayers. This method produces high purity areas of graphene on top of a wide gap semiconductor and it is the most promising for being used in future graphene based nanoelectronics.

-Epitaxial growth on metals by carbon assisted surface catalysis [12]. Graphene can be successfully grown on the hexagonal surface of most transition metals. The interaction between the metallic substrate and the graphene layer ranges from weak adsorption to strong chemisortion. This method has the advantage that is highly scalable in roll-to-roll mass production and the drawback that the resulting product consists normally in highly defective pollycrystalline films.

-Graphite oxide reduction through chemical methods [13]. Graphite oxide is a well known composite produced after HOPG sonication in an acid solution. The resulting product are highly dispersed carbon powder with a few percent of single layer planes. These sheets are, however, highly functionalized through –OH, -COOH,-O- and other oxygen rich groups. Reduction of this material yields to highly defective graphene layers that result very cheap to produce.

In the present work we focused on the two methods more suitable for surface science studies. These are the two epitaxial growths, on SiC and on metals, and more precisely weakly interacting metals.

Graphene on weakly interacting metals: Moirés

The less interacting metals are, in progressive order, Au, Ag, and Cu. However these metals are so little interacting that only very recently, and through smart advanced growth techniques graphene has successfully been grown on them [14] [15](no graphene on Ag has been reported as far as we know). The next metals in low reactivity would be, Ir, Pt and Pd. Graphene can be successfully grown on the highly-packed hexagonal surfaces of these metals either by annealing the carbon rich samples (carbon segregation) or through annealing the samples in the presence of an external carbon-rich molecular precursor. Early studies in the 1970s of "*single layer graphite*" [16] [10] on transition metal surfaces depicted a very rich landscape of graphitic

structures on weakly interacting metal surfaces. Several orientations of the graphene overlayers with respect to the substrate are permitted and the electronic interference between substrate and graphene produces a Moiré pattern. For weakly interacting metal surfaces several Moiré patterns with different angles and periodicities have been reported. The exact determination of these structures is difficult to find from a theoretical point of view as the number of atoms involved is very high. In the present work we have carefully analyzed STM images and combined them with some theoretical models in order to draw a full picture of the growth of graphene on weakly interacting metal surfaces.

Graphene on SiC: electronic effects

Silicon carbide is a wide bandgap semiconductor that is well suitable for high temperature, high frequency transistors [17]. Again, it was known the presence of "*single layer graphite*" on top of the hexagonal surfaces of this material long before isolation of mechanical exfoliated samples was achieved [11]. The surface of SiC passes through several surface reconstructions when annealed in vacuum before it develops graphene. Moreover annealing at higher temperatures (typically >1500K) induces the apparition of multilayer growth on the SiC(0001) Si-terminated face. Graphene grow on SiC(0001) expresses very interesting electronic properties; the electronic band structure is analogous to freestanding graphene and when inspected with local microscopy techniques, such as STM, it appears transparent or opaque depending on the used bias voltage – the honeycomb structure is "visible" only within a small range of scanning conditions. G/SiC(0001) presents quantum interferences between electrons of different sublattices and it exists the valley degree of freedom. All these characteristics makes G/SiC(0001) an ideal system to test the fundamental properties of this pure sp^2 compound.

Study of molecules on graphene

Graphene is supposed to be relatively inert to most atmospheric airborne contaminants, this is, low sticking coefficients towards O_2, N_2, and more importantly, H_2O molecular exposition. This is the result of a highly saturated electronic structure and a high crystallinity with low amount of

defects. The basal plane of graphene flakes normally interacts with condensed adsorbates through weak interactions, but some species can chemisorb on top of in-lattice embedded C atoms. Highly reactive atomic adsorbates, such as O or H, tend to interact strongly with the substrate while organic molecules and, more precisely, aromatic molecules tend to present a dominant intermolecular contribution into the force balance. We profited this quasi-free behavior of G/SiC(0001) to test the reactivity of graphene upon molecular deposition of selected adsorbates. In order to span all the interaction spectra we have studied the atomic scale structure of graphene functionalizated with two opposed species: atomic hydrogen and C_{60}. The behavior comparison between both systems will give insight into the adsorption mechanisms on graphene.

Thesis Outline

After introducing the experimental techniques used along this work we will present the results. The thesis is presented in two independent blocks, and the blocks are divided in chapters.

Graphene on Pt(111):

1. We have grown epitaxial overlayers by means of molecular epitaxy of carbon rich molecules. The precise role of molecular precursor- and its dissociation temperature- to form polycrystalline surfaces consisting in graphene patches with different orientations will be discussed.
2. In our search for understanding the stability of the different rotational domains we have developed a simple model that finds the best coincident lattice positions ,for both Pt(111) substrate and graphene overlayer, for every graphene twist angle. We will compare the predictions of the model with the experimentally observed Moirés to test the limits of our model and to reveal some critical aspects in the Moiré stability of G/Pt(111).
3. The atomic structure of the smallest observed –and predicted- Moiré, namely $(\sqrt{3}x\sqrt{3})R30^{o}$, is studied in detail

through the comparison between STM images and advanced DFT calculations.

4 (√7x√7)R19^{o} is the most commonly observed Moiré superstructure of G/Pt(111) for a wide range of growth conditions. In the present section we will present a detailed analysis of STM images together with calculations to fully determine the atomic configuration of this structure.

5 The relation between stable rotational domains and the bonding region between the metal substrate and graphene is discussed in this section. Nucleation and subsequent growth from the Pt(111) atomic steps is discussed and compared with our phenomenological model.

6 Among all the crystalline edges found in the experiments we have studied in detail the contact region between (√7x√7)R19^{o}-graphene and Pt(111) step edge. Theory predicts the apparition of exotic 1D states in the vicinities of the contact region and experiments show the existence of electronic inhomogeneities localized in this region.

7 Defective structures with different dimensionalities of G/Pt(111) will be introduced as strain relief mechanisms. The accumulated mismatch between substrate and overlayer produces high stress amounts that relax through the formation of atomic scale defects. A *bestiary* of these defects is presented and described in this section.

8 At last we will extract some conclusions out of our analysis of the G/Pt(111) system.

Graphene on SiC(0001):

1 Once we anneal the samples at 1450K the Si loss is so important that a carbon-rich atomic reconstruction appears. We normally obtain a surface where different reconstructions coexist. The dominating reconstruction is known as (6√3x6√3)R30^{o}/SiC(0001). The periodicity of this

structure under diffraction measurements differs with the periodicity measured with local techniques –quasi-6x6. We will present the less abundant quasi-5x5.
Single layer graphene is characterized by a combination of experiments and calculations. The exotic electronic properties that this system expresses are discussed.
Higher order graphene stacking, such as bilayer graphene, are briefly presented. With this section we end the characterization of the SiC(0001) surface reconstructions.

2 Hydrogen adsorbates deposited on graphene at 300K result a model system of chemisorbed structures on graphene basal plane. The interaction strength will be analyzed and the adsorption configuration of the hydrogen clusters appearing on the surface will be studied in detail by a combination of high resolution STM images and advanced DFT calculations.

3 We will compare the behavior of hydrogen adsorbates with that of C_{60} molecules deposited both at 300K and at 40K on the same single graphene surface. We will study the strength of the dominating intermolecular interaction through STM sequences of the dynamics of the C_{60} molecular adsorbates and after comparison with vdW-DFT calculations.

4 Finally we will point out the conclusions of our study on simple adsorbates on G/SiC(0001).

After all this considerations, general conclusions will be extracted out of the comparison of both graphene systems. Both are considered to be weakly interacting systems whose graphene epitaxial structures perform near-free behavior. However, we can notice that graphene grown on metals presents structural properties much more affected by the underlying substrate than those of G/SiC(0001).

Bibliography

1. Binnig, G.; Rohrer, H., Scanning tunneling microscopy. *IBM Journal of research and development* **2000,** *44* (1-2), 279-293.
2. Stroscio, J. A.; Eigler, D., Atomic and molecular manipulation with the scanning tunneling microscope. *Science* **1991,** *254* (5036), 1319-1326.
3. Ulman, A., Formation and structure of self-assembled monolayers. *Chemical reviews* **1996,** *96* (4), 1533-1554.
4. Kroto, H. W.; Heath, J. R.; O'Brien, S. C.; Curl, R. F.; Smalley, R. E., C60: Buckminsterfullerene. *Nature* **1985,** *318* (6042), 162-163.
5. Iijima, S.; Ichihashi, T., Single-shell carbon nanotubes of 1-nm diameter. **1993**.
6. Novoselov, K. S.; Geim, A. K.; Morozov, S. V.; Jiang, D.; Zhang, Y.; Dubonos, S. V.; Grigorieva, I. V.; Firsov, A. A., Electric Field Effect in Atomically Thin Carbon Films. *Science* **2004,** *306* (5696), 666-669.
7. Neto, A. C.; Guinea, F.; Peres, N.; Novoselov, K. S.; Geim, A. K., The electronic properties of graphene. *Reviews of modern physics* **2009,** *81* (1), 109.
8. Geim, A. K., Graphene: status and prospects. *science* **2009,** *324* (5934), 1530-1534.
9. Geim, A., Graphene prehistory. *Physica Scripta* **2012,** *2012* (T146), 014003.
10. Land, T. A.; Michely, T.; Behm, R. J.; Hemminger, J. C.; Comsa, G., STM investigation of single layer graphite structures produced on Pt(111) by hydrocarbon decomposition. *Surface Science* **1992,** *264* (3), 261-270.
11. Mårtensson, P.; Owman, F.; Johansson, L. I., Morphology, Atomic and Electronic Structure of 6H-SiC(0001) Surfaces. *physica status solidi (b)* **1997,** *202* (1), 501-528.
12. Batzill, M., The surface science of graphene: Metal interfaces, CVD synthesis, nanoribbons, chemical modifications, and defects. *Surface Science Reports* **2012,** *67* (3–4), 83-115.
13. Eda, G.; Fanchini, G.; Chhowalla, M., Large-area ultrathin films of reduced graphene oxide as a transparent and flexible electronic material. *Nature nanotechnology* **2008,** *3* (5), 270-4.
14. Martínez-Galera, A. J.; Brihuega, I. n.; Gómez-Rodríguez, J. M., Ethylene Irradiation: A New Route to Grow Graphene on Low Reactivity Metals. *Nano letters* **2011,** *11* (9), 3576-3580.
15. Bae, S.; Kim, H.; Lee, Y.; Xu, X.; Park, J. S.; Zheng, Y.; Balakrishnan, J.; Lei, T.; Kim, H. R.; Song, Y. I.; Kim, Y. J.; Kim, K. S.; Ozyilmaz, B.; Ahn, J. H.; Hong, B. H.; Iijima, S., Roll-to-roll production of 30-inch graphene films for transparent electrodes. *Nature nanotechnology* **2010,** *5* (8), 574-8.
16. Lang, B., A LEED study of the deposition of carbon on platinum crystal surfaces. *Surface Science* **1975,** *53* (1), 317-329.
17. Soukiassian, P. G.; Enriquez, H. B., Atomic scale control and understanding of cubic silicon carbide surface reconstructions, nanostructures and nanochemistry. *Journal of Physics: Condensed Matter* **2004,** *16* (17), S1611.

Chapter 1. Theoretical and experimental methods

Nanotechnology has become a new important discipline in Science. This multidisciplinary branch of knowledge combines results obtained within more “classical sciences”, such as physics, chemistry or biology, during the last 30 years, in order to study the behavior of the nature when nanometric scales come into play. A nanometer is a billionth of a meter (10^{-9} m), or 10 Armstrong (Å) and is approximately the size of a tetracene molecule [see **Figure 1 1**] i.e. four benzene rings merged together. Within this length scales physical objects must be studied under a quantum perspective; nature no longer behaves under the classical Newtonian laws but new intriguing and rather counterintuitive rules control the stability, kinematic and dynamic of a particle.

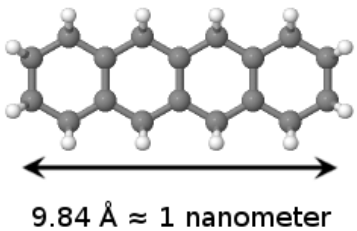

Figure 1 1: *Ball and stick model o a tetracene molecule whose lateral side measures approximately 1nm.*

The quantum theory –developed during the beginning of the century- formulates the atomic particles (in our case, mostly electrons) in terms of wavefunctions. Within this mathematical approach particles are no longer described in a deterministic frame, but they are characterized in terms of probabilities. The probability of, for example, an electron to be in a determined position is proportional to the modulus of the wavefunction in that precise position and deterministic particles become clouds of probabilities. Therefore measurements in the nanoscale need to take into account these “quantum world” effects and average the result of multiple single measurements.

A typical “quantum measurement” could be the determination of the lattice parameter of a crystal. This distance usually ranges in the order of the few Ås and to analyze it we study the pattern formed by diffracted X-Rays scattered out from the crystal. The X-rays interfere constructively or destructively depending on the crystallography of the sample. The quantum paradox arises when we compare the measures of single X-ray photons (i.e

one by one) with the overall landscape after billionths of single photon measurements. Single photons appear randomly distributed (appearing scattered even in regions forbidden by quantum mechanics) but when billionths are measured a clear diffraction pattern arises revealing the preferential and forbidden scattering directions. From this pattern the lattice parameter of the crystal can easily be extracted. Nanotechnology, and more precisely surface science, necessarily must take into account these quantum properties and limitations.

Modern surface science takes advantage of all the technical advances in order to study the superficies of the solids. The structural and electronic properties of these exterior regions normally behave similar to the bulk of the material but they are affected by the proximity of the vacuum interface. However some heterostructures and material´s surfaces can express properties very different from those of the hosting material and expresses very unusual and exotic properties. Surface science methodologies provide the control to study and model complex 2D systems and for understanding its atomic scale chemical-physical properties.

Several experimental techniques were used during the work performed in this thesis. Modern surface science supplies a handful of different techniques providing important parameters of the surface of the systems under study. Most of them can be subdivided in two main groups: experimental techniques using a “wave-like” probe (photons, electrons…), and experimental techniques using a sharp tip placed almost in contact with the sample as a probe. Among the first ones we find, LEED, LEEM, UPS, XPS, AES… and among the tip-based we find the AFM and STM, which where the main techniques used in this work.

In the following chapter, these experimental techniques and their theoretical fundamentals are described. The structure of this chapter will be as it follows: First, I will shortly introduce the theoretical frame for every different technique. Second, I will describe the particular implementation of every technique that has been used during these works. Third and last, I will shortly introduce typical results and the information that can be extracted out of them.

1.1. Scanning Tunneling Microscopy (STM)

In 1981 Gerd Binnig and Heinrich Rohrer invented the Scanning Tunneling Microscopy (STM) in their laboratory of IBM in Zurich. This new technique brought, for the first time, the possibility of observe atomic scale objects on atomically flat surfaces [1] [2]. This invention was awarded with the Nobel Prize in physics only 5 years later, in 1986 for "*for their design of the scanning tunneling microscope*". It permitted to study in real space the interactions occurring between atoms and molecules, while resolving them individually. STM also provided for the first time the possibility of moving single atoms in a controlled manner, placing them at your will, and study the structures formed after that [3]. It can be said that STM is the key discovery fostering modern nanotechnology; after its invention, for the first time the mankind was provided with a tool that could "touch" atoms one by one.

The STM is based in quantum tunneling of electrons through an energy barrier between a metallic tip and a conducting or semiconducting surface. In classical mechanics a particle with a certain energy ($E_{Particle}$) cannot surpass an energy barrier ($E_{Barrier}$) when $E_{Particle} < E_{Barrier}$. In quantum mechanics a particle has a non vanishing probability to go through a potential barrier higher than the energy of the considered particle. The quantum tunneling effect is this non negligible probability of the quantum wave-functions to surpass the energy barrier [4]. In **Figure 1 2** we see a schematic representation of the 1D tunneling effect.

The tunneling barrier between tip and sample is modeled by a potential with energy equal to the vacuum level (E_{VL}). An electron in the sample (or tip) with an energy, E, smaller than the barrier ($E < E_{VL}$), will satisfy the Schrödinger's equation. Neglecting thermal excitation the Fermi level is equal to the work E_f=-Ø. Applying a voltage bias, V, we can obtain a tunneling current I. Assuming the work functions of tip and sample to be equal and eV<< Ø we obtain a current value satisfying:

$$I \propto V\, \rho_S(E_F) e^{-2h\frac{\sqrt{2m\emptyset}}{\hbar}}$$

This means the value of the current is proportional to the: applied bias (V) and the local density of states (LDOS) of the sample´s surface at the Fermi level ($\rho_S(E_F)$); and exponentially dependent on the distance between sample and tip (h).

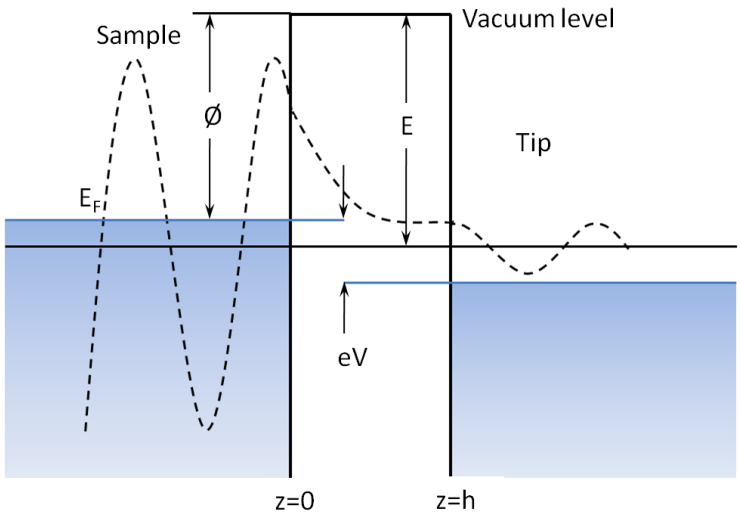

Figure 1 2: *Quantum mechanical energy scheme of tunneling between two ideal metals. [Adapted from J.Chen [2]]*

Due to the exponential behavior of the tunneling current with respect to the distance between tip and sample we can assume the main contribution to the current (up to 90%) coming from the tunneling through the last atom in the tip, and the vast majority (up to 99%) coming from the apex atom and its first neighbors atoms in the tip pyramid. Therefore by scanning a sharp tip on top of an atomically flat surface we can map de density of states of a sample´s surface. The spatial resolution can be estimated in terms of the radius of the apex (R) and the distance between tip and sample (*d*) to be $1.4\sqrt{d+R}$ [Å]. When using a sharp tip, a STM can achieve atomic resolution of metals and graphene [5].

ESISNA group hold three UHV operating STMs in their facilities. The ICMM laboratory has a variable temperature (40-300 K)STM (VT-STM) and a room temperature STM (RT-STM). The CAB laboratory has a RT-STM in its Spectroscopy and Microscopy on Surfaces (SMS) UHV chamber. They are all commercial instrumentation provided by Omicron GmBH and operated with Nanotec electronics. The **Figure 1 3** shows a model of the microscopes of our group. Sample and tip are respectively colored in red and blue, the tip is mounted on the piezoelectric tripod stage which is used to move it over the surface and scan. The whole STM is mounted on a magnetic bumper in order to minimize mechanic vibrations. In **Figure 1 4** we present

a picture of a real nc-AFM/STM instrument that is held out of vacuum for maintenance and reparation.

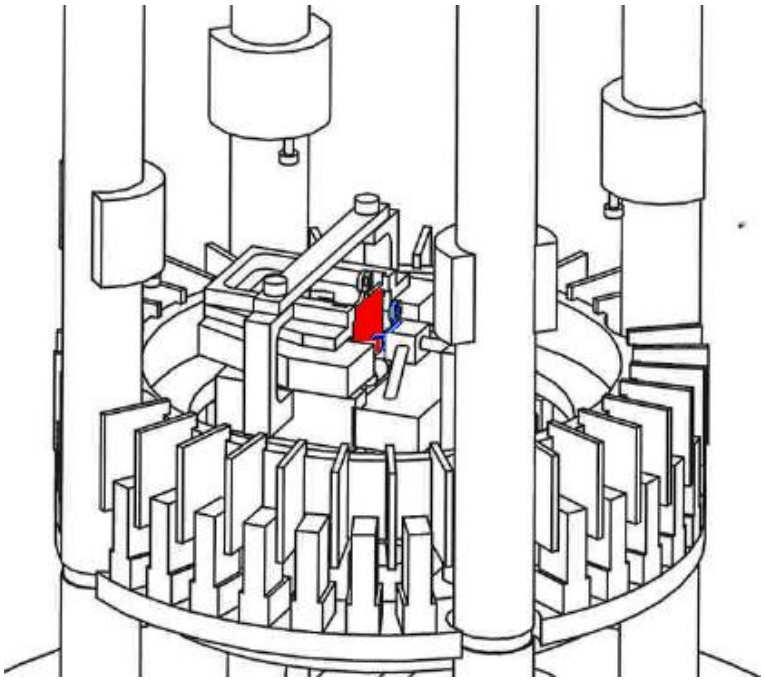

Figure 1 3: *Schematic representation of a UHV STM. The red colored platelet corresponds to the sample holder where the sample is mounted. The blue colored part corresponds to the scanning tip, mounted onto a piezoelectric tripod.*

The tip is controlled by a scanning feedback system. There are two major operation regimes: constant current and constant height. In the constant current mode the loop circuits measures the value of the tunneling current and readjust the voltage towards the piezos in order to keep the current constant. Therefore if the samples morphology makes the tunneling current to decrease, the feedback loop is going to push the tip closer to the sample in order to obtain the desired scanning current. This constant current regime is also known as topographic mode, as somehow it is related to the surface topographic landscape (supposing the changes in the LDOS to be small). On the other hand we have the constant height mode, where the tip is kept at fixed distance on the sample and changes in the tunneling current are mapped. In the present work both regimes were used.

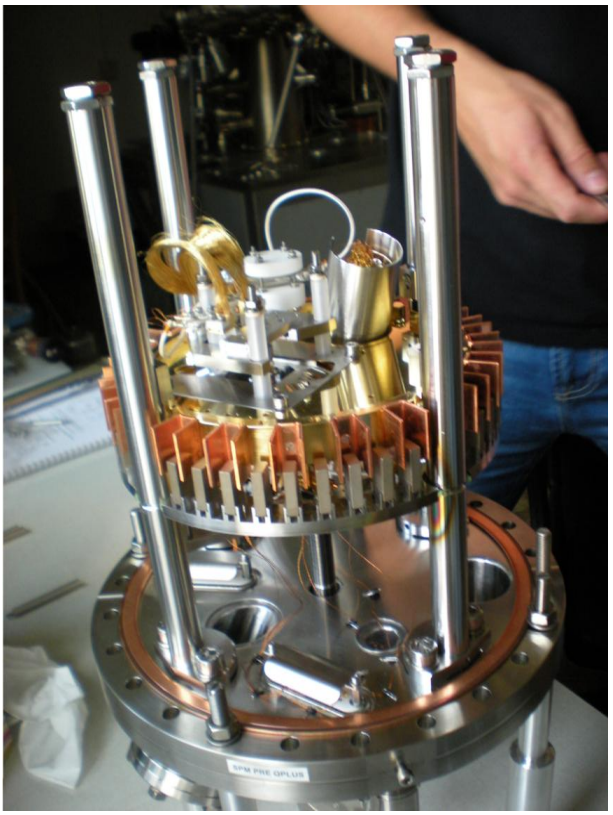

Figure 1 4: *Picture of a nc-AFM-STM instrument similar to the one depicted schematically in* **Figure 1 3** *but adapted to low temperature measurements.*

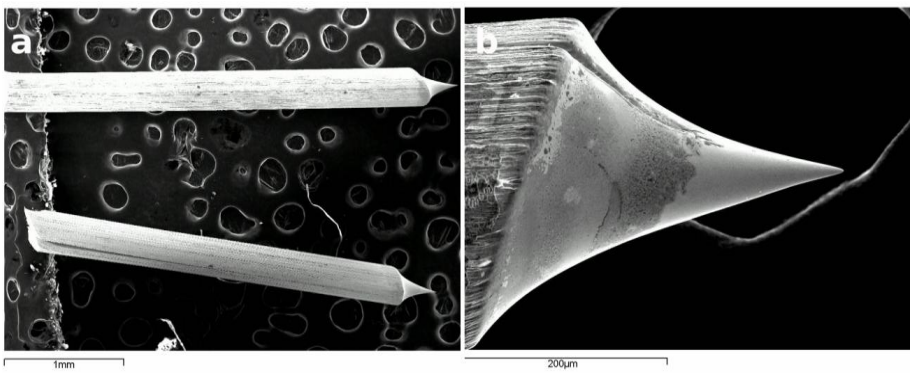

Figure 1 5: *SEM (scanning electron microscope) images of tungsten STM tips*. **a.** *Two tips, the scale bar represents 1mm*. **b.** *Apex of a single tip. The scale bar represents 200 µm.*

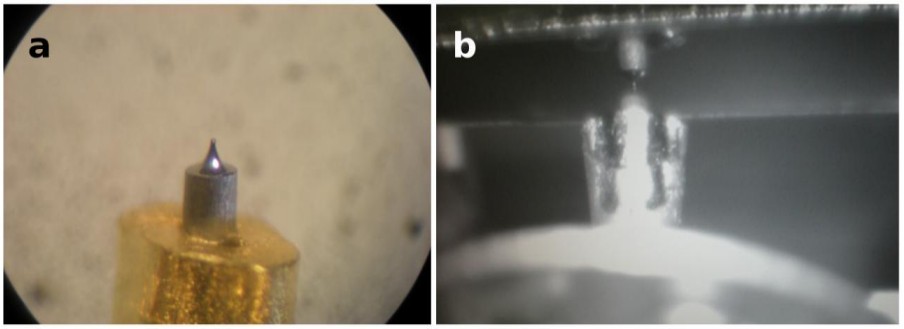

Figure 1 6 : *STM tips under optical microscope***. a.** *A commercial tip mounted onto a gold-coated tip-holder***. b***. A tip during scanning into the microscope. The reflecting surface corresponds to a SiC sample.*

In **Figure 1 5** we present scanning electron microscope SEM images of tungsten tips. These tips were done in-house by etching them into a NaOH solution though electrochemical methods. These tips are then mounted and approached through piezoelectric motors towards the surface. A picture of a STM during measurements can be seen in **Figure 1 6 : *STM tips under optical***

Figure 1 6 shows typical images of an STM. In these images there are fullerenes and graphene coexisting on the same region. When using a small bias (100mV) fullerenes look distorted because they have not a significant density of states (DOS) around the Fermi level and tip crashes with the molecule while trying to readjust the current to its nominal value. This is so, because they are molecules and therefore they only have a limited number of (more or less hybridized) molecular orbitals. On the other hand when imaging graphene at 100mV the contrast is mainly coming from the sp^2 overlayer, while, when imaging it at higher bias (200mV) the main characteristic are the subsurface features. This seems to indicate that graphene LDOS is mainly localized around the Fermi level while the subsurface states have states at higher energies. In our STM design the bias voltage is applied to the tip.

Apart from imaging, STM can be used in spectroscopic modes. In these working modes the feedback system is usually turned off and the tip is placed on top of a particular surface structure. There are several spectroscopies: I(z), z(V), I(V)… among them I(V) and its derivative study dI/dV are the most normally used. In this technique we measure the current (I) for a given voltage (V) and we measure it for a wide range of voltages. Supposing the DOS of the tip to be constant, it can be shown [6]

that dI/dV provides direct information about the LDOS of the sample. It can probe the occupied and unoccupied states of the material with atomic resolution. Curiously, the tips that are good for imaging normally have a sharp atomic orbital on the apex, which makes them very poor for STS. On

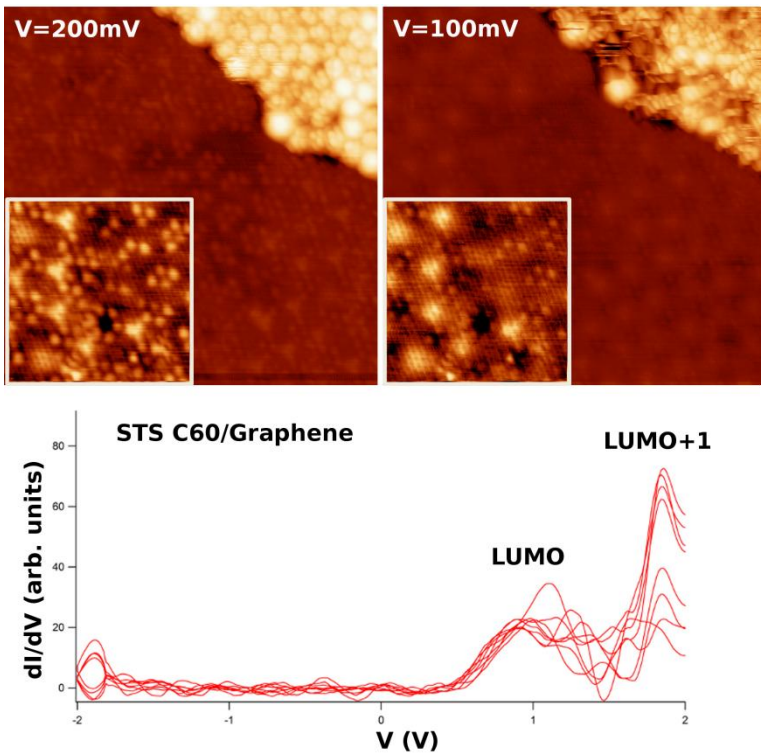

Figure 1 6: *upper part, STM images at two different bias of C_{60} molecules (upper right corner) and graphene showing differences with voltage. At 100mV the fullerenes do not have significant DOS and thus electrons from the tip cannot tunnel to them, while at 200 mV the fullerenes have more states but graphene instead does not, and therefore it looks transparent. Lower part, dI/dV spectrum of C_{60} molecules on SiC. The molecular orbitals in the unoccupied region of the energies are revealed at around 1V (LUMO) and 1.7V (LUMO+1).*

the other hand tips that have a blunt DOS on the apex might be good for spectroscopy, but they are normally useless for imaging.

1.2. Atomic Force Microscopy (AFM)

The main disadvantage of STM is that the sample under study must be conducting (or semiconducting) and as a consequence insulating materials cannot be analyzed. There are important systems, such as oxides (TiO_2, CeO_2…) and ionic solids (NaCl…), which are isolating. Moreover, the big organic molecular complexes, such as the ones relevant in biology (DNA, proteins, lipid membranes…) are not conductive. The AFM was invented by G. Binnig in 1986 in order to pass through this limitation. Shortly after Calvin Quate and Christoph Gerber developed the first instrument [7].

The AFM is similar to STM but the conductive tip is changed by a force sensor measuring the force between tip and sample ($F_{T\text{-}S}$). The tunneling current exponentially decays with increasing distance and has a very short range. Opposed to that, the $F_{T\text{-}S}$ has long-range and short-range additive contributions. Among the short range contributions the chemical forces are the most important; the main contribution arises from the formation of chemical bonds between atoms in the sample and the apex atom in the tip while scanning. Long-range forces can be attributed to a broader variety of effects such as: van der Waals contributions, electrostatic, magnetic forces and, when scanning in ambient conditions to the force of the meniscus of water formed between the sample and the tip [8] [9].

The force sensors are the central elements of the AFM [10]; they are the major difference with STM and they are the "spring" that measures the $F_{T\text{-}S}$. Nowadays there are two basic families of AFMs based in two different kinds of force sensors. The first family of AFMs is based in silicon microfabricated cantilevers; most of them have "diving-board" geometry with a small protruding pyramid on the opposite end. When using silicon cantilevers we exploit the reflectivity of the polished Silicon to place a focused laser beam just on the end of the cantilever that is reflected with a certain angle out from it. This laser will carry the signal of the deflection of the cantilever, which is proportional to the force. The laser beam needs to be properly focused in order to reduce its diameter to few μm and carefully directed to the cantilever. The reflected laser signal is directed to a photodiode (see **Figure 1 7**) normally divided into quadrants. Depending on which quadrant the laser illuminates we can extract the deflection of the AFM and readjust the tip with feedback loops to either go closer or farther from the sample.

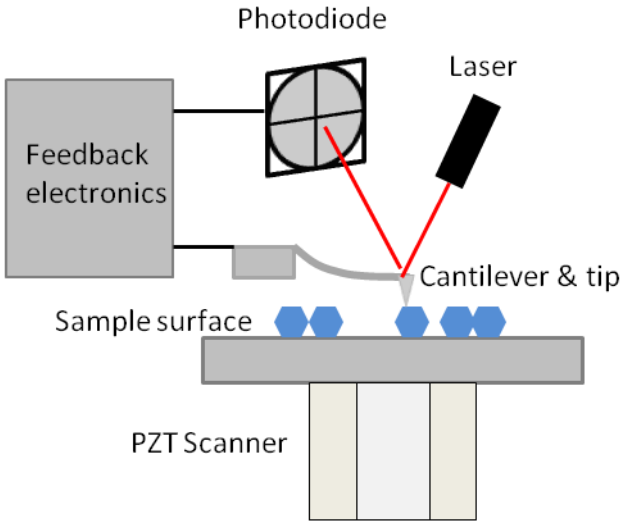

Figure 1 7: *Schematic representation of the working conditions of a regular laser-based AFM. The tip is placed near the surface scanning it. The reflected laser signal spots into a photodiode that traduces the light intensity variations to forces between tip and sample.*

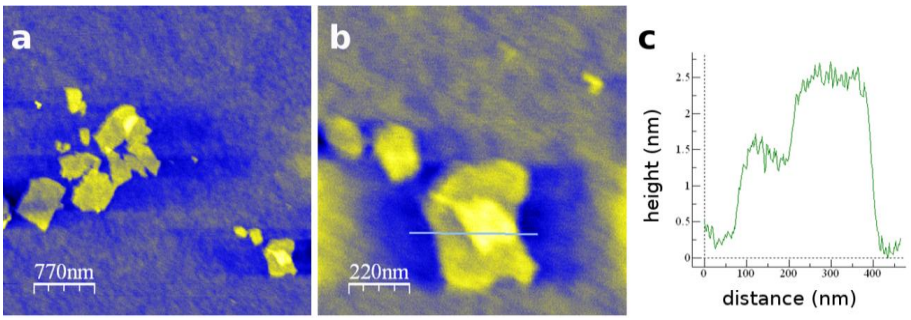

Figure 1 8: *AFM images of reduced graphene oxide onto a polished SiO_2 surface of native oxide on a Si wafer.* **a & b.** *Laser-based tapping mode AFM images of graphene oxide flakes.* **c.** *Height profile extracted from the* **b** *image, where it is marked with a light blue line.*

The second design of AFM was developed by Franz Giessibl around 1998 [11] [12]. The force sensor used in this implementation (see **Figure 1 9**) is a tungsten tip attached to the apex of a quartz tuning fork. Tuning forks are used as frequency standards in clocks because they have very sharp

oscillatory modes. In this configuration the $F_{T\text{-}S}$ is measured by the power needed to maintain the tuning fork in its resonance mode.

Figure 1 9: *Optical microscope image of a force sensor based on the measurement of the dissipation energy of a conducting tip placed on top of a quartz tuning fork.*

AFM can be operated in different modes. The static mode of AFM is very similar to the functioning of a regular STM. But most times AFM is operated in dynamic modes; within this mode, we force the tip to oscillate on the sample´s surface. By measuring the decrease in the amplitude of the oscillation we can extract the force between the sample and the tip. This so called tapping mode results less intrusive to the sample and is normally used for measuring nanostructures deposited on flat surfaces as they can be easily moved with other imaging modes.

1.3. Low energy electron diffraction (LEED)

The low energy electron diffraction (LEED) was first discovered in 1927 at Bell Labs [13]. Electron diffraction was predicted by L. de Broglie after his famous hypotheses in 1924 [14] and only 3 years later got its experimental confirmation, however its use in surface science for characterization had to wait more than 30 years to dispose of vacuum techniques permitting to keep a surface atomically clean for a sufficiently long period of time. LEED exploits the quantum nature of electrons that may behave as a particle and/or as a wave depending on how we observe them. The usual LEED apparatus (see **Figure 1 10**) consists in an electron gun irradiating collimated electrons onto a crystalline sample. The arriving electrons interact with the surface reflecting and diffracting. The interference between the diffracted electrons forms an intensity pattern characteristic of the topmost surface crystallography. This intensity pattern can normally be observed onto a fluorescent screen and results very useful for identifying surface structures and reconstructions as it is directly related to the 2D reciprocal lattice of the surface crystal symmetry. Because the

electrons have very low energy they are very weakly accelerated onto the sample; this yields a situation where these electrons mainly interact with the few topmost atomic layers of the sample. This extreme selectivity to the surface terminations together with its simplicity makes LEED an ideal technique for surface characterization prior to measurements through more complex methods, such as Surface X rays diffraction or SPM's.

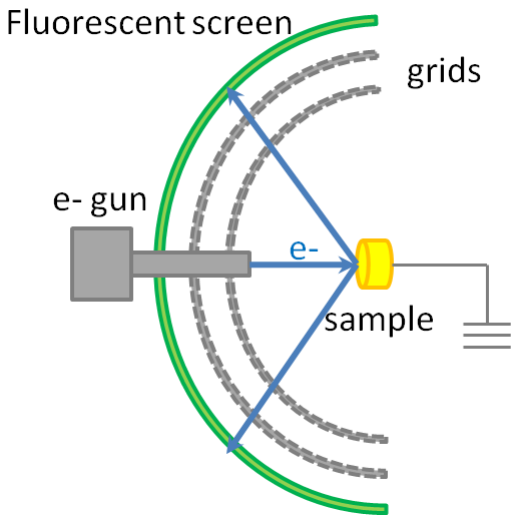

Figure 1 10: *Sketch of the basic components of a LEED device. The electrons from the electron gun are accelerated towards the surface and the reflected ones retarded and finally accelerated towards a fluorescent screen showing the interference LEED pattern.*

Depending on the nature of the sample different patterns can be observed. Simple metals normally relax its metal-vacuum truncation through out of plane relaxations and therefore they rarely show surface reconstructions. Thus 1x1 patterns of the different surface terminations (normally (111), (110), and (100)) are normally seen in the fluorescent screen after surface preparation; an exception to this rule could be the so called "herringbone reconstruction" of the Au(111) surface whose unit cell corresponds to 22x√3 [15]. On the other hand, semiconductors usually reconstruct in complex unit cells, consisting in several nonequivalent atoms per unit cell. Clean Si(111) reconstructs in a 7x7 supercell involving two different halves. The so called DAS model involves dimmer, adatoms and stacking faults [16].

Another interesting case is SiC(0001). This surface presents several surface reconstructions after been annealed at different temperatures. The as

receive sample is normally covered by a SiO_2 native oxide layer, but still presents a 1x1 LEED pattern. After annealing the samples at 1100K in the presence of a Si flux (normally a Si evaporator) it develops a sharp 3x3 pattern. Si depletion occurs if we anneal the sample to temperatures above 1150K; the surface and the surface stoichiometry varies progressively. The pattern passes from a $(\sqrt{3}x\sqrt{3})R30^{o}$, $(6\sqrt{3}x6\sqrt{3})R30^{o}$ to a graphene LEED patterns (see **Figure 1 11**).

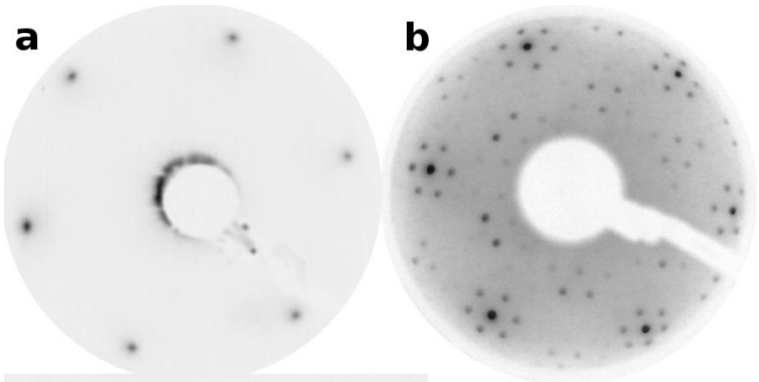

Figure 1 11:a. *LEED pattern of the clean 1x1 surface of Pt(111) at 130eV.* **b.** LEED *pattern of the* $(6\sqrt{3}x6\sqrt{3})R30^{o}$ *and graphene structure at 120 eV.*

LEED can also be used in a quantitative manner. The different nonequivalent points occurring into the pattern normally reflect with different intensity upon irradiation of electrons with different energies. Thus intensity versus voltage of the incident electrons curves can be plotted for every diffracted spot of the pattern. These curves can be also calculated numerically for different theoretically proposed surface atomic configurations permitting the use of LEED I(V) curves as a tool for unveil the average position of the atoms within the surface unit cell.

1.4. Low energy electron microscopy (LEEM) and X-ray photoemission electron microscopy (XPEEM)

This new kind of microscopy was developed during the 1960s by Ernst Bauer and collaborators but it was not completely developed until 1984 [17] [18]. It is based in the previously described physical phenomena of electron diffraction and thus only crystalline surfaces can be imaged. The usual

geometry of these instruments is the threefold symmetry depicted in **Figure 1 12**, the three columns are respectively called illumination column, imaging column and sample chamber [19].

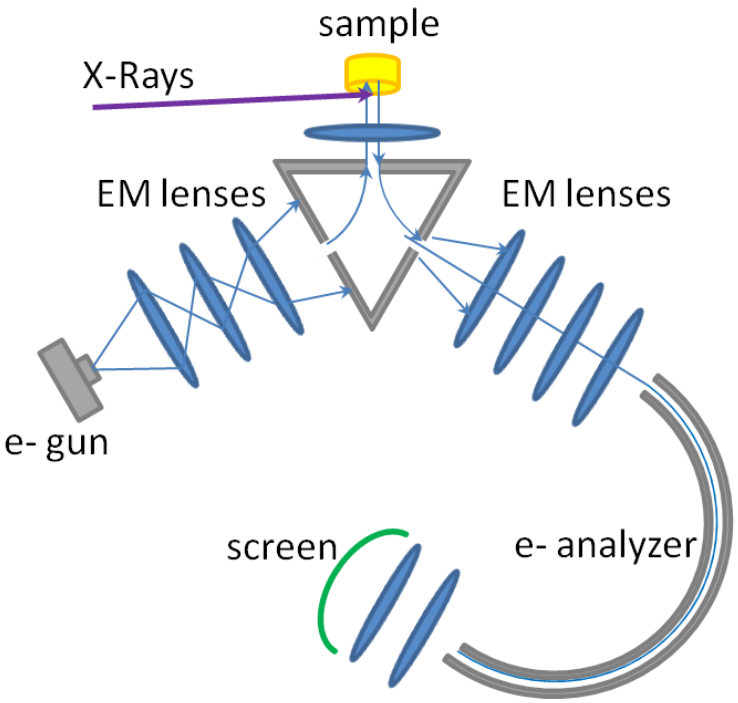

Figure 1 12: *Schematic representation of the usual geometry of a LEEM – PEEM apparatus. The tree-fold geometry allows to use the three different sides for illumination column, sample, chamber and imaging column respectively.*

Upon illumination of the sample with either electrons, UV photons from an Hg lamp or synchrotron radiation [20] the reflected or photoexcited electrons form on the objective a magnified image of the sample surface. Depending on the lens configuration we change from real (surface imaging) to reciprocal (LEED pattern) spaces. The electrons are later filtered by energy through a hemispherical electron analyzer and projected into a multichannel plate where the signal is collected. There are also filtering slits that can be placed in one of the reciprocal space planes in order to permit only one of the diffracted LEED spots to continue the optical path. When this slit is placed in, in the real space plane (imaging mode) we will only see contrast arising from the surface regions (normally atomic terraces) that contribute to that particular crystallographic phase/diffraction spot. If we place the slit allowing only the (0,0) diffraction spot to pass the slit we

enhance the contrast of the LEEM image; this imaging mode is normally called bright field mode, as all the crystalline phases contributing to the (0,0) diffraction spot are imaged. On the other hand, if we place the slit allowing only one diffracted beam (other than (0,0) spot) pass the filter we obtain in the imaging planes micrographs of the surface where the only intensity comes from the terraces that express that particular crystallographic reconstruction. This imaging mode is called dark field imaging.

1.5. Photoemission spectroscopy (PES): XPS, UPS

The photoemission spectroscopy is based in the photoelectric effect in which a free electron is extracted from an atom after absorbing a photon. This effect was first observed by Heinrich Hertz in 1887 [21] and fully understood after Albert Einstein famous paper in 1905 which made him deserve the Nobel Prize in Physics.

The effect can be described as follows; one bound electron absorbs a high energy photon, normally X-rays or ultraviolet, turning into a free electron of kinetic energy (E_K) (**see Figure 1 13**). The binding energy (E_B), the photon energy ($h\upsilon$) and the work function (Ø) fulfill the relation:

$$E_K = h\upsilon - E_B - \phi$$

Knowing the energy of the impinging photon and measuring the kinetic energy of the resulting free electron we can extract the energy of the former bound electron. For measuring the kinetic energy of the free electrons we normally use an experimental set up consisting in a cylindrical electron analyzer for energy filtering and an electron multiplier like a channeltron or a channelplate as a collector. The laboratory standard X-Ray guns normally have a double anode of Mg (K_α , $h\upsilon = 1253.6\ eV$) and Al (K_α , $h\upsilon = 1486.6\ eV$) and the usual UV illumination consist in an He lamp whose principal lines are He I $h\upsilon = 21.2\ eV$ and He II $h\upsilon = 40.8\ eV$. Synchrotron radiation can also be used as an illumination source; its main advantages are higher photon flux and better monochromacy, which combined increases the energy resolution up to a tenths of meV for XPS and few meV for UPS. Another big advantage is that we can tune the energy of the arriving photons in a continuous range and thus set a photon energy that maximizes the photoexcited electrons of the element under analysis.

Depending on the energy of the illuminating photon we will excite different bound electrons giving rise to different photoemission spectroscopies. Thus if we use X-rays, the electrons that are mainly excited result the core level electrons (XPS) while if we use ultraviolet electrons we will excite the valence band electrons (UPS) [22].

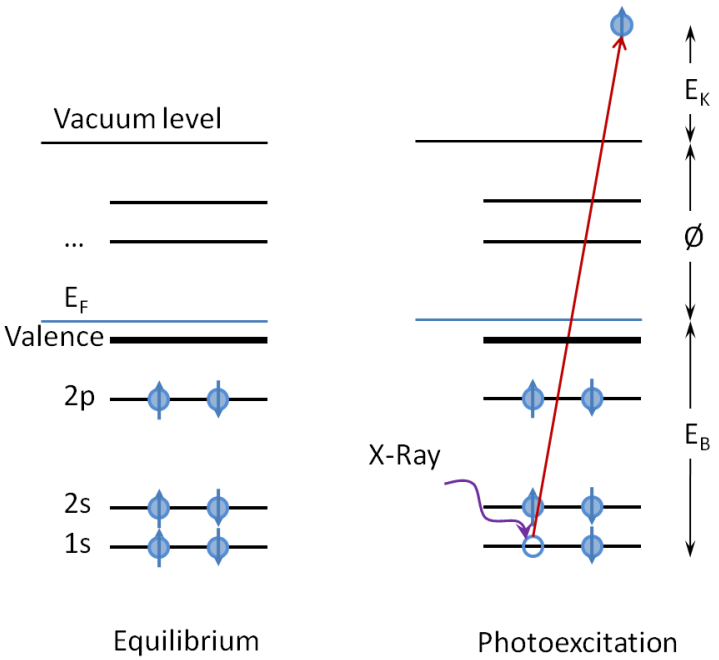

Figure 1 13: *Schematic representation of the photoelectric effect. The Sketch shows the working principles of XPS. A photon excites a core-level electron above the vacuum level. The kinetic energy of the outgoing electron is recorded and the binding energy can be calculated.*

XPS is a powerful technique for the characterization of the chemical species present on a surface. The characteristic energy values of the levels in every chemical element has been tabulated since the technique was developed, and complete inventories of the resonances appearing under standard X-Ray illumination are present in many handbooks [22] or web applications. XPS is not only sensitive to the chemical element but it is also sensitive to the electronic and chemical environment of the particular element. Small energy shifts (surface core level shifts or SCLS) from the nominal value of a particular state are normally attributed to different chemical bonding configurations, and thus to the electronic environments, of this element (see **Figure 1 14**). If we have, for example, a carbon (C) atom bonded in sp^2

configuration with three other C atoms the C1s peak will have its maximum at energy around 284.8 eV [23], while if we have C bonded to Si in the form of carbide (SiC) the C1s peak will appear shifted to lower energies around 283 eV. The XPS spectra were analyzed using the FITT program developed by Hyun-Jo Kim (Seoul National University). This program allows a fit of the peaks by convoluting Lorentzian and Gaussian contribution to the width of a specific core level.

UPS spectrum is a measurement of the valence band of a particular material. If this substance is conductive we will find electron populating levels around the Fermi level. Because the Fermi-Dirac distribution we will find a small quantity of electrons above it, as the thermal excitation makes these electron to spill over the Fermi level. On the other hand if the material is insulating we will find that no electrons are populating the Fermi level and we can very easily calculate the band gap as the energy difference between the last occupied electronic band and the Fermi level. However one must take care of charge effects that might be occurring and make the band gap appear distorted.

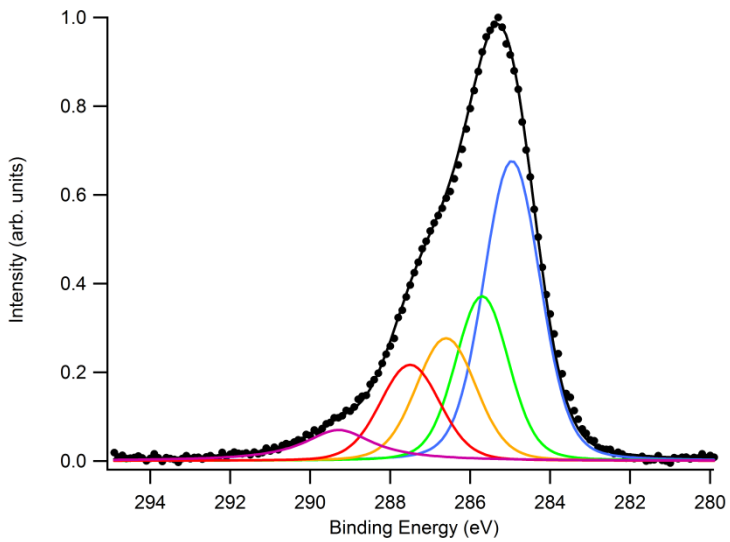

Figure 1 14: *XPS deconvolution of graphene oxide. The blue component, centered at 284.8eV corresponds to C in sp^2 configuration; the other components are assigned to different carbon oxidized species.*

1.6. Density functional theory (DFT)

In order to complement the experimental observations with a theoretical framework, density functional theory (DFT) calculations have been performed of most of the systems studied in the present thesis. Modern DFT was developed during the 1960s by P. Hohenberg, L. Sham and W. Kohn [24], among others, and made the last one to deserve the Nobel Prize in chemistry of 1998.

From a theoretical point of view we need to solve the Schröedinger equation of the many body system, finding its eigenvalues (energies) and its eigenfunctions (wavefunctions). In order to solve such a complex equation several approximations and strategies have to be taken. DFT proposes a new approach; instead of searching the wavefunctions we will search for the electronic density. The Hohenberg-Kohn theorem establishes that it exists a one-to-one relationship between the fundamental state and a particular electron density which calculates the energy functional [25]. This makes the system easier to calculate, as we change from a problem were we have 3N variables (being N the number of electrons in the system under study) to a problem where we have a quantity, the electronic density, which depends on only 3 variables.

There are many available calculation packages including DFT approximations, however from a practical point of view there are two main "schools". The difference between them comes from the choice of the mathematical basis used for describing the electronic density. On one side we have the description of the electronic states in terms of a plane wave basis; this set permits more precise calculations but it is more time computing consuming. Usual plane wave codes -as VASP or CASTEP- normally include the option of performing spin-resolved calculations. On the other side we can use a linear combination of atomic orbitals (LCAO) as a basis set. These calculations are normally less time consuming allowing exploring larger unit cells. The LCAO calculation does not normally include spin variables. In **Figure 1 15** we see the relaxation of the (√7x√7)R19º-G/Pt(111) unit cell with the FIREBALL code, this code is based on the LCAO approach.

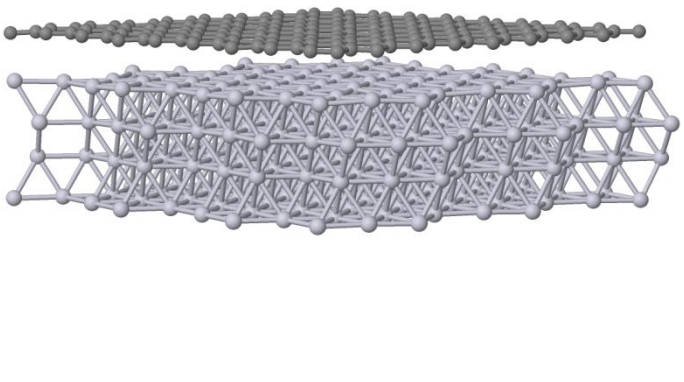

Figure 1 15: *Ball and stick model of the optimized relaxed structure of the (√7x√7)R19°-G/Pt(111) Moiré, where the grey spheres correspond to carbon atoms and the blue spheres to Pt atoms. The unit cell has been repeated four times to ease the visualization. The structure has been relaxed using the FIREBALL code.*

One of the most important outcomes that DFT brings for an STM experimentalist is the STM image simulation of the relaxed surface structures. For this purpose a metallic pyramid (normally W or another metal) is relaxed independently to be used as an STM tip. The FIREBALL package used in this work for this purpose uses the local-density approximation (LDA) and the Keldish-Green function formalism to calculate the tunneling current (J). The equation that describes J has the form:

$$J = \frac{4\pi e}{\hbar}\int_{E_F}^{E_F+eV} T_r[T_{TS}\rho_{SS}(E)D_{SS}^{R}T_{ST}\rho_{TT}(E-eV)D_{TT}^{A}]\,dE$$

Where T refers to the hopping matrix, ρ to the electronic density, and D to the probability of multiple scattering; and the suffixes S and T to sample and tip respectively.

The calculations shown in this thesis have been performed by the group of Dr. P. Jelinek, the group of Prof. R. Pérez – Dr. P. Pou and L. Rodriguez –, by the theoretical part of the ESISNA group – Dr. P. de Andrés, Dr. I. Martínez, Dr. C. González – and by Dr. Y. J. Dappe and Dr. E. Abad.

1.7. Vacuum instrumentation

a. Ultra High Vacuum (UHV) systems

Surface science did not develop until ultra high vacuum (UHV) pressure was accessible in the mid 1950s. UHV chambers result necessary in order to prevent the sample from getting contaminated from the residual gases present in the atmosphere within seconds; in order to ensure the cleanliness of the sample for periods in the order of 1 hour, an estimation of the minimal time we will need for performing our experiments, we will need to lower down the pressure to the range of 10^{-10} mbar. In fact, according to the kinetic gas theory, the number of particles striking a surface per square cm per second is [ERTL]:

$$\dot{n}_S = N_g \sqrt{\frac{RT}{2\pi M}} \approx 2.7 \times 10^{22} \frac{p}{\sqrt{MT}} \ (cm^{-2}s^{-1})$$

Where p is the pressure in mbar, M the molecular weight of the dominant specie of the residual gas, and T the temperature in K. Assuming M=28 and T=300 we have $\dot{n}_S \approx 10^6 p$ so we need a pressure lower than 10^{-6} mbar in order to keep the surface clean for a second. However another important factor that needs to be taken into account when calculating the deposition rates is the sticking factor of the adsorbate. This is the probability of an impinging molecule to remain fixed to the surface and ranges between 0 and 1. Depending on relative reactivity of surface and adsorbate an the substrate temperature we will have systems where very little of arriving molecules stick to the surface (S≈0), for example noble gases on metals, or where most of them get “glued” to the surface(S≈1), for example oxygen on semiconductors.

b. Si evaporator

There is not a unique way to build a Silicon evaporator. Here I will present the model that we constructed, adapted from the work of Johansson *et al*. on SiC [26]. This particular design is intended for SiC cleaning procedure. This needs high quantity deposition –around 1ML/s- of Silicon in order to keep the Si/C stoichiometry on the Si depleted SiC surfaces. Si depletion naturally occurs when heating SIC above 800C and these temperatures are needed for removing the native oxide layer that all commercial wafers came with.

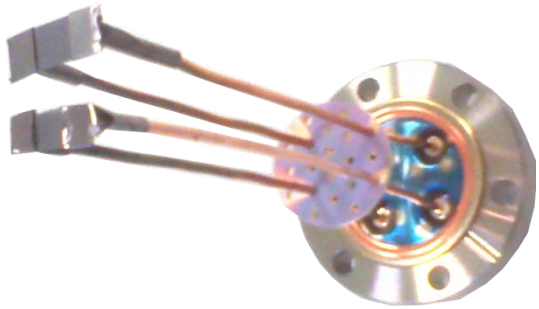

Figure 1 16: *Picture of a double Si evaporator. The copper wires end on Ta clamping a Si platelet. The two upper copper wires and the two lower ones form independent evaporators. Passing current though the Si piece causes the semiconductor to heat at temperatures around 1500K it evaporates material in the form of atomic Si.*

A picture of the design can be seen in **Figure 1 16**. It is very simple; it consist in a Si platelet of typically 1.5x0.5x0.1 cm^3, cut away from a Si wafer with a diamond tip, attached to a commercial UHV feedthrough with home-made Ta clamps for electrical contact. The operation mode consist as follows: first we apply 70V volts to the Si plate, this voltage fall makes the Si warm up but no current runs through the circuit. Once Si is warm, it starts conducting, and thus the circuit is governed by current. Typical parameters for getting SI evaporation consist in reaching 1550 ^oC on the platelet, which normally implies 15A, 4V with a partial pressure in the order of $5x10^{-10}$ mbar. Because the need of such high temperatures for Si evaporation it is very important to very carefully degas the device prior to exposure to the sample. The model presented in **Figure 1 16** has two independent evaporators one in the upper part and the other in the lower part of the image.

c. Molecular beam evaporator

The deposition of organic molecules needs a different strategy other than simple direct current annealing of the substance that we want to evaporate. For evaporating such molecules we introduce them into a home-made Ta crucible welded to two stainless steel or copper bars. Passing current through these bars we increase the temperature of the crucible.
The temperature of the molecules is controlled by a thermocouple welded to the Ta envelope (see **Figure 1 17**).

Figure 1 17: *Picture of the "head" of a home-made molecular evaporator. It consists in a Ta envelope, where the molecules are deposited, which is contacted by two cupper wires in order to close the circuit. Passing current trough the system makes the Ta to warm up and the molecules to evaporate. A thermocouple is spot-welded to the envelope in order to monitor the temperature.*

This approach results very clean and allows evaporation of a wide range of complex adsorbates. However, normally prior to its use the crucible is degassed into UHV above in order to desorb water and other contaminants that may alter the purity of the molecules. Then the Ta envelope is filled with the desired molecule and degassed again up to temperatures slightly above the evaporation temperature, in order to get rid of any possible impurity or chemical remnants that may be mixed with the molecules.
In this thesis C_{60} has been used. It was a commercial item bought to Sigma Aldrich with 99.9% purity. The typical evaporation temperature is 700-780K to obtain a rate of evaporation of around 0.1ML/min. During the deposition the pressure was always below $5x10^{-10}$ mbar.

d. H-cracker

Two independent designs of hydrogen crackers were used in the experiments to dissociate ultra pure molecular hydrogen. The H-flux atomic hydrogen source manufactured by TECTRA GmBH and a custom made H-cracker. The first design is based on the thermal molecular dissociation occurring when hydrogen passes through a tungsten capillary heated up to 2500K by electron bombardment. Its working characteristics are almost 100% cracking efficiency and zero residual ion current (no protons are created). Normal operating conditions, consisting typically of hydrogen partial pressure of 1×10^{-9} mbar, yields under typical pumping systems an atomic flux of 5×10^{13} atoms/cm^2 on a sample located typically at 10 cm.
The second hydrogen cracker used in the experiments is a homemade design. The cracking mechanism is analogous to that used in the quadrupole mass spectrometer (QMS). The gas enters the UHV chamber through a capillary whose end is placed in the proximity of a Faraday cell and a tungsten filament. The filament is used as an electron emitter and the

Faraday cell is positively charged (70V) in order to accelerate the electrons. The H_2 molecules are hit by the electrons in a process that cracks them down into atomic hydrogen.

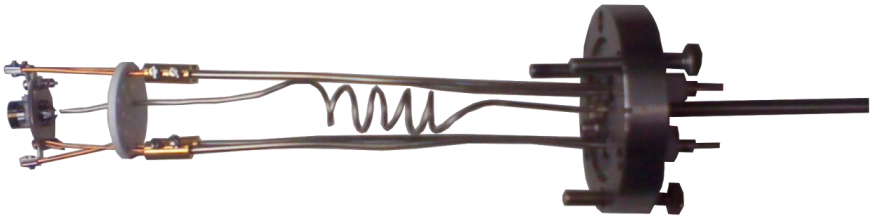

Figure 1 18: *Picture of our home-made H-cracker. The hydrogen is introduced through the serpentine ant the rest of Cu contacts serve to pass the high voltage as well as for passing current through the filament.*

1.8. Surface preparation

a. Pt(111)

Pt(111) single crystals were acquired to commercial firms. They present different geometries depending on the main technique that is going to be used. Thus for diffraction "fat" cylinders with relatively big (1 cm diameter) surfaces are normally used while for STM the geometry used in ESISNA laboratory is the "hat-like" where the surface, typically 5mm diameter, is smaller than the base and the sample can be tweezed with wires. The experiments were carried in ultra high vacuum environment with normal pressures in the low 10^{-10} mbar. The cleaning procedure of the Pt(111) substrate is a well established protocol consisting of three or more cycles of annealing the sample at 1200-1300 K in an oxygen atmosphere (typically 1-5 x 10^{-6} mbar) in order to remove from the surface all possible carbon contaminants, such as surface carbides and molecular adsorbates, in the form of CO and CO_2 which leaves the surface and is pumped away from the chamber.

After this procedure several cycles of argon sputtering and annealing are needed in order to obtain a clean surface well suitable for STM experiments. Normal sputtering parameters for Pt(111) are P_{Ar}= 1 x 10^{-5} mbar accelerated with 1.5kV, impinging the substrate and generating typical currents of 8-12 μA during periods of 10-15 min. After this procedure the sample surface strongly roughen, in order to "reorder" again the Pt(111) steps a strong-1200K- annealing in an extremely low – <5 x 10^{10} mbar- base pressure needs to be performed. The annealing step of the

cleaning procedure is shown as a picture taken through an UHV window in **Figure 1 19**.

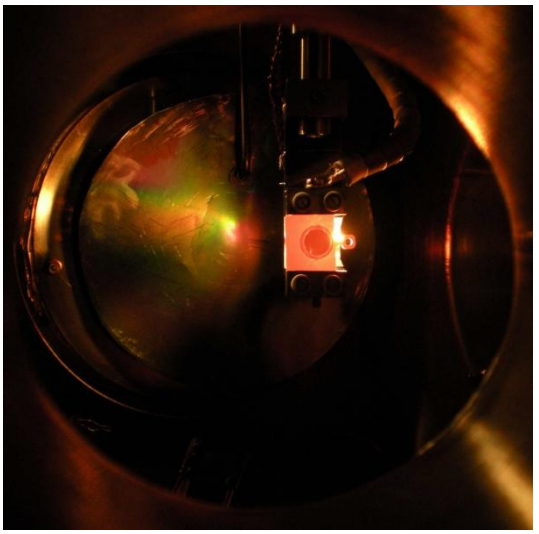

Figure 1 19: *Picture of the annealing of the Pt(111) sample. The red-glowing platelet is the sample holder irradiating visible light. The darker orange circle inside the glowing square is the Pt(111) sample at an approximated temperature of 1100K.*

After this cleaning procedure we obtain a sample exhibiting well developed (1x1) LEED pattern, and a surface morphology consisting inn clean Pt(111) terraces of 10-100 nm width, separated by monoatomic steps that typically run parallel to the Pt[1-10] direction. The Pt crystallizes in a face centered cubic (FCC) crystallography with a lattice parameter of 3.92Å. This yields a Pt(111) morphology of Pt atoms organized in a hexagonal configuration with a first-neighbor distance between atoms of 2.77 Å. The single step height is 2.26 Å; however as the sample ages it results more and more easily to observe multiple steps originated from processes of step bunching. In **Figure 1 20** we present STM images of the clean Pt(111) surface both at the atomic scale, as well as the parallel single-atom step terraces.

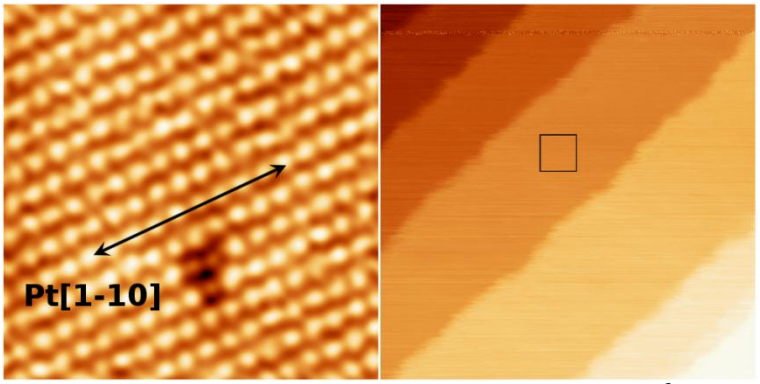

Figure 1 20: *STM images of clean Pt(111) surface*.**a**. *5x5 nm^{2}Atomically resolved high resolution image where every of the protrusions corresponds to a single Pt atom*. **b.** *50x50nm^2 image showing straight atomic steps, the small black sqare corresponds to the area comprised in the* **a** *image.*

b. 6H-SiC(0001)

SiC is a wide gap semiconductor that can be purchased to commercial firms in the form of wafers with different doping grades. Small stripes can later be cut apart from the wafer with the help of a diamond tip. These ready-to-mount samples have later been put on two different sample-holders: the usual Omicron standard which consist in a small Ta platelet with an adequate geometry for the vacuum tweezers, or the usual omicron sample holders for semiconductors, in which the sample is mounted between two electrical contacts, in order to pass a direct current through it so it can be annealed by direct heating. The preparation of the SiC(0001) was performed in ultrahigh vacuum, although it can be done in an inert atmosphere- such as Ar- with similar results. The first step of the preparation of SiC consists in removing the native oxide layer that is formed when the sample is exposed to the air and that protects the surface. For this process we developed a recipe consisting in a slow degas of the whole annealing stage keeping the pressure below 1x10^{-9} mbar up to a sample temperature of 1000-1100 K. The sample temperature is normally monitored using a infrared pyrometer with a emissivity set at 0.53 [27]. Once the sample is properly degassed we deposit Si at a rate of 1ML/s with the help of the Si evaporator that has already been introduced in this section. We can either maintain the surface at RT or at high temperature, but it seems more effective to do cycles of Si evaporation while annealing the sample at 1100K during 10-15 min (a picture of this process is shown in

Figure 1 21). After doing a cycle we normally check the sample with the LEED. The SiC(0001) sample just after being introduced in UHV exhibits a faint 1x1 pattern, after doing 5-10 cycles of Si evaporation while annealing the pattern changes to a sharp 3x3 one. It is important to notice that the appearance of the 3x3 pattern does not assure that the sample is well prepared for STM inspection, as the LEED pattern can appear even when the terraces are very small, or only a part of the surface is covered with the 3x3 reconstruction.

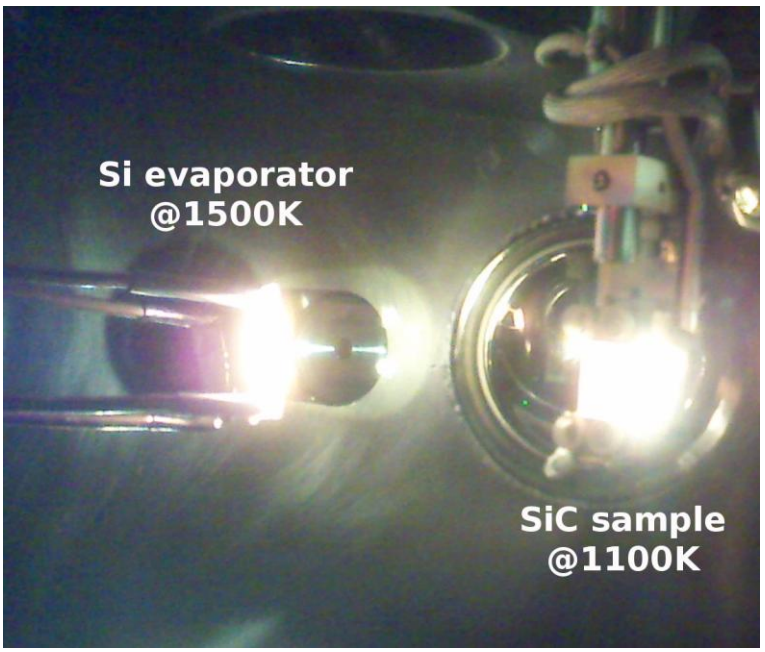

Figure 1 21: *Picture of the interior of the UHV chamber during the Si evaporation and SiC treatment. The Si evaporator is placed at the left of the image whereas the sample is on the right part of the image.*

Once we have the surface with a developed 3x3 surface periodicity we consider the sample well suited for preparing other surface reconstructions. This is performed by simple annealing to different temperatures. If we anneal the sample at 1200K we observe that the LEED pattern suddenly changes to a $(\sqrt{3}x\sqrt{3})R30^{o}$ structure; when inspected with STM we observe that the surface morphology has been strongly altered and a $(\sqrt{3}x\sqrt{3})R30^{o}$ periodicity appears. In case we increase the temperature to 1350K, Si depletion induces a stoichiometry where the most favored structure is the $(6\sqrt{3}x6\sqrt{3})R30^{o}$ surface reconstruction. Annealing beyond this temperature induced a Si loss so severe that graphitic phases are predominant.

Depending on the temperature we can control the number of graphene layers. This process is shown through a combination of the atomically resolved STM images of the same size in **Figure 1 22** and described in detail in the last part of this thesis.

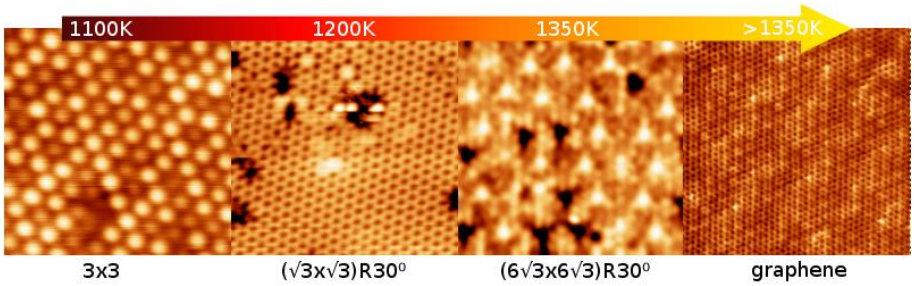

Figure 1 22: *Atomically resolved STM images of the SiC surface annealed at increasing temperatures. From left to right we pass ffrom the Si-Rich 3x3, (√3x√3)R30°,(6√3x6√3)R30° and finally graphene.*

1.9. Description of the experimental systems used in this thesis

During the realization of this thesis we have used up to 10 different experimental UHV chambers. However the most of this thesis have been performed in three of them, the chamber in *Centro de Astrobiología* (CAB), the chamber in ICMM and the chamber in FZU (Institute of Physics of the Academy of Sciences of the Czech Republic). The chamber in CAB (see **Figure 1 23**), consists of an UHV vessel equipped with a hemispherical electron analyzer, a LEED apparatus and a room temperature STM. The illumination sources are a double anode (Mg-Al) soft X-rays gun –for XPS studies-, a He UV lamp –for UPS - and a electron gun- for Auger spectroscopy -. The chamber in ICMM consists of a room temperature STM and a LEED instrument. The chamber in FZU consists of a UHV vessel with a LEED instrumentation with a channel-plate for LEED I(V) characterization and a variable temperature STM head modified to combine, STM measurements with Q-Plus nc-AFM measurements. All of them were equipped with quadrupole mass spectrometry, LEED, heating system, gas lines and free CF-ports where to mount the molecular evaporators.

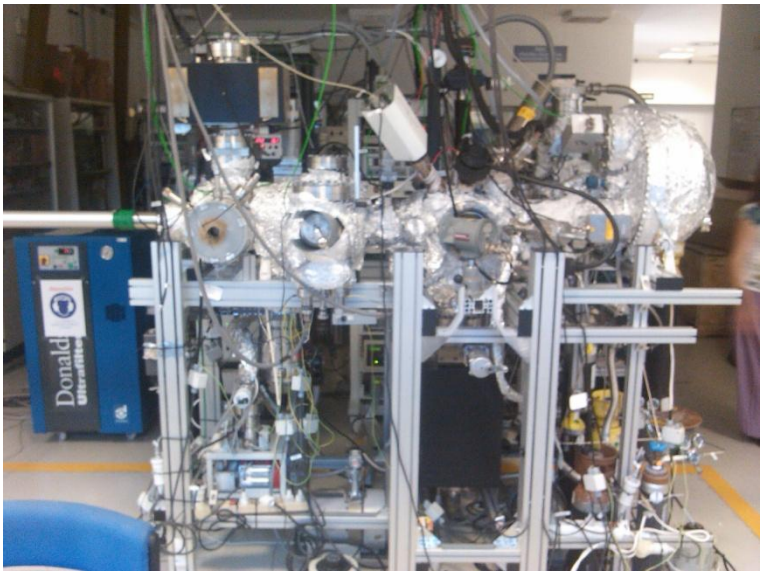

Figure 1 23: *Picture of the combined microscopy and photoemission chamber held by the Centro de Astrobiologia.*

The rest of the chambers used during this thesis were placed in synchrotrons radiation facilities and were designed for surface diffraction (ESRF ID03 and ESRF Spline), PEEM (ALBA-CIRCE) or high resolution XPS (Elettra-SuperESCA) or surface preparation prior to synchrotron measurements.

Bibliography

1. Binnig, G.; Rohrer, H., Scanning tunneling microscopy. *IBM Journal of research and development* **2000,** *44* (1-2), 279-293.
2. Chen, C. J., *Introduction to scanning tunneling microscopy*. Oxford University Press New York: 1993; Vol. 227.
3. Stroscio, J. A.; Eigler, D., Atomic and molecular manipulation with the scanning tunneling microscope. *Science* **1991,** *254* (5036), 1319-1326.
4. Cohen-Tannoudji, C.; Diu, B.; Laloë, F., Quantum Mechanics, 2 Volume Set. NewYork: John Wiley & Sons, Inc: 2006.
5. Binning, G.; Rohrer, H.; Gerber, C.; Weibel, E., Surface studies by scanning tunneling microscopy. In *Scanning Tunneling Microscopy*, Springer: 1993; pp 31-35.
6. Giaever, I., Energy gap in superconductors measured by electron tunneling. *Physical review letters* **1960,** *5* (4), 147.
7. Binnig, G.; Quate, C. F.; Gerber, C., Atomic force microscope. *Physical review letters* **1986,** *56* (9), 930-933.
8. Giessibl, F. J., Advances in atomic force microscopy. *Reviews of modern physics* **2003,** *75* (3), 949.
9. Giessibl, F. J., Forces and frequency shifts in atomic-resolution dynamic-force microscopy. *Physical Review B* **1997,** *56* (24), 16010.
10. MORITA, S. A.; WIESENDANGER, R. A.; MEYER, E. A., *Noncontact atomic force microscopy*. Springer: 2002; Vol. 1.
11. Giessibl, F. J., High-speed force sensor for force microscopy and profilometry utilizing a quartz tuning fork. *Applied physics letters* **1998,** *73* (26), 3956-3958.
12. Giessibl, F. J., Atomic resolution on Si (111)-(7× 7) by noncontact atomic force microscopy with a force sensor based on a quartz tuning fork. *Applied Physics Letters* **2000,** *76* (11), 1470-1472.
13. Davisson, C.; Germer, L. H., Diffraction of electrons by a crystal of nickel. *Physical Review* **1927,** *30* (6), 705.
14. De Broglie, L., Waves and quanta. *Nature* **1923,** *112* (2815), 540-540.
15. Narasimhan, S.; Vanderbilt, D., Elastic stress domains and the herringbone reconstruction on Au (111). *Physical review letters* **1992,** *69* (10), 1564.
16. Takayanagi, K.; Tanishiro, Y.; Takahashi, M.; Takahashi, S., Structural analysis of Si (111)-7× 7 by UHV-transmission electron diffraction and microscopy. *Journal of Vacuum Science & Technology A: Vacuum, Surfaces, and Films* **1985,** *3* (3), 1502-1506.
17. Bauer, E., LEEM basics. *Surface Review and Letters* **1998,** *5* (06), 1275-1286.
18. Tromp, R.; Mankos, M.; Reuter, M.; Ellis, A.; Copel, M., A new low energy electron microscope. *Surface Review and Letters* **1998,** *5* (06), 1189-1197.
19. Tromp, R.; Hannon, J.; Ellis, A.; Wan, W.; Berghaus, A.; Schaff, O., A new aberration-corrected, energy-filtered LEEM/PEEM instrument. I. Principles and design. *Ultramicroscopy* **2010,** *110* (7), 852-861.

20. Locatelli, A.; Aballe, L.; Mentes, T.; Kiskinova, M.; Bauer, E., Photoemission electron microscopy with chemical sensitivity: SPELEEM methods and applications. *Surface and interface analysis* **2006,** *38* (12-13), 1554-1557.
21. Hertz, H., Ueber einen Einfluss des ultravioletten Lichtes auf die electrische Entladung. *Annalen der Physik* **1887,** *267* (8), 983-1000.
22. Moulder, J. F.; Chastain, J., *Handbook of X-Ray Photoelectron Spectroscopy: A Reference Book of Standard Spectra for Identification and Interpretation of XPS Data*. Perkin-Elmer Corporatioon, Physical Electronics Division: 1992.
23. McFeely, F.; Kowalczyk, S.; Ley, L.; Cavell, R.; Pollak, R.; Shirley, D., X-ray photoemission studies of diamond, graphite, and glassy carbon valence bands. *Physical Review B* **1974,** *9* (12), 5268.
24. Kohn, W.; Sham, L. J., Self-consistent equations including exchange and correlation effects. *Physical Review* **1965,** *140* (4A), A1133.
25. Gilbert, T., Hohenberg-Kohn theorem for nonlocal external potentials. *Physical Review B* **1975,** *12* (6), 2111.
26. Johansson, L. I.; Owman, F.; Mårtensson, P., High-resolution core-level study of 6H-SiC(0001). *Physical Review B* **1996,** *53* (20), 13793-13802.
27. Kaplan, R.; Parrill, T. M., Reduction of SiC surface oxides by a Ga molecular beam: LEED and electron spectroscopy studies. *Surface Science* **1986,** *165* (2–3), L45-L52.

Chapter 2.
Epitaxial graphene on Pt(111)

Graphene is the material of the last decade. Its experimental discovery in 2004 in the laboratories of A. Geim and K. Novoselov in Manchester [1] has fostered an immense amount of scientific effort that has returned important outcomes in the form of an increasing amount of papers [2]and practical applications [3]. Several productions methods –apart from the originally proposed mechanical exfoliation of highly oriented pyrolytic graphite (HOPG) - have been proposed and achieved. Among the most important ones are the epitaxial growth techniques of graphene on single crystal surfaces; the result of these production methods result very promising for future applications as the quality of the resulting sheets is much better than the quality of the –normally used method in massive production - reduced graphene oxide layers, which usually exhibit a large amount of oxygen related defects.

Graphene consist in a single layer of C atoms bonded between them in a sp^2 orbital hybridization with trigonal planar geometry and C-C distance of 1.42 Å. The two atoms per unit cell yield a lattice constant of 2.46Å. It has exceptional mechanical and electronic properties [4], making this single layer graphite material simultaneously the world´s thinnest, strongest and stiffest material, and an excellent electric and thermal conductor [2].

Two kinds of electronically different materials are normally used as substrate: semiconductors (like SiC that will be discussed in chapter 3) or metals (among them is Pt, the subject of the present chapter of this thesis). Most metals develop graphene layers on its surface when annealed to high temperatures, typically 1000-1500 K, in the presence of an external source of carbon or by segregation of C dissolved in the metal [5 6]. The formation of graphene on metallic surface has been mostly studied on hexagonal surfaces, like the (0001) for the HCP crystallographic structures –Ru [7 8], Co [9 10], Re [11]- and the (111) for the FCC metals – Ni [12], Cu [13], Rh [14],Pd [15], Ir [16], Pt [17] and Au [18]- but it has also been observed to grow on non-hexagonal crystallographic surfaces such as Pt(100) [19 20].The interference between the hexagonal substrate and the honeycomb lattice of graphene give rise to Moiré superstructures of different periodicities for every transition metal. Depending on the reactivity of the substrate, the interaction strength can range from van der Waals physisorption to strong bonded chemisorption. Moreover, the interaction between the substrate and the overlayer drives the corrugation of graphene and the mean distance with the substrate [21]. Normally, when the interaction is not very strong different rotational domains appear [22 17 15] every of them with a different apparent angle and periodicity.

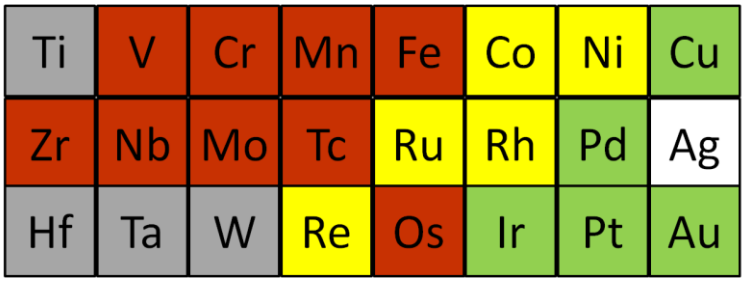

Figure 2 1: *Table of the carbon stability on transition metal surfaces adapted from Ref. 6. The color scale is as follows: Grey means the most favored C phase is a carbide, red means that carbon reactivity remains unknown, yellow and green means that C may grow as graphene layers on these surfaces; yellow means that only one orientation is normally obtained whereas different rotational domains (or Moirés) are found for the metals with a green color.*

Among the weakly interactive transition metal hexagonal surfaces, Pt(111) is a model substrate. Epitaxial graphitic layers on Pt(111) were discovered as soon as 1975 by B. Lang in its pioneering LEED study [23]. The first STM study of this system is also previous to the discovery of graphene: T. A. Land *et al.* reported in 1992 the presence of at least three different rotational domains, or Moirés, of "single layer graphite" on Pt(111) formed by hydrocarbon decomposition [24]. Later works have found a big amount of Moiré structures of graphene on Pt(111) with LEEM [25] or STM [26]. However the agreement between the different experimental observations is not good and different research groups have described different orientations between graphene and Pt(111). To clarify this complex system, G/Pt(111), we have performed a combined theoretical-experimental approach. Our results are described in the sections below.

2.1. Growth of G/Pt(111) in UHV

The graphene growth process is schematically reproduced in **Figure 2 2**. This process is based in the deposition at room temperature (300K) of big aromatic molecules, such as fullerene (C_{60}) [27] or $C_{60}H_{30}$ [28], following by an annealing at typical temperatures of 1100-1200K that induce a thermal decomposition of the precursors. Other variants of this method have also been put down, such as the use of small hydrocarbons precursors (in our case propane, C_3H_8) or the deposition of the carbon rich molecules on the hot samples. All these variants result to be successful to form graphene. The fact that most recipes success in the formation of graphene on Pt(111) indicates that this is a thermodynamically favored process and that Pt(111) is a good catalyst for this reaction.

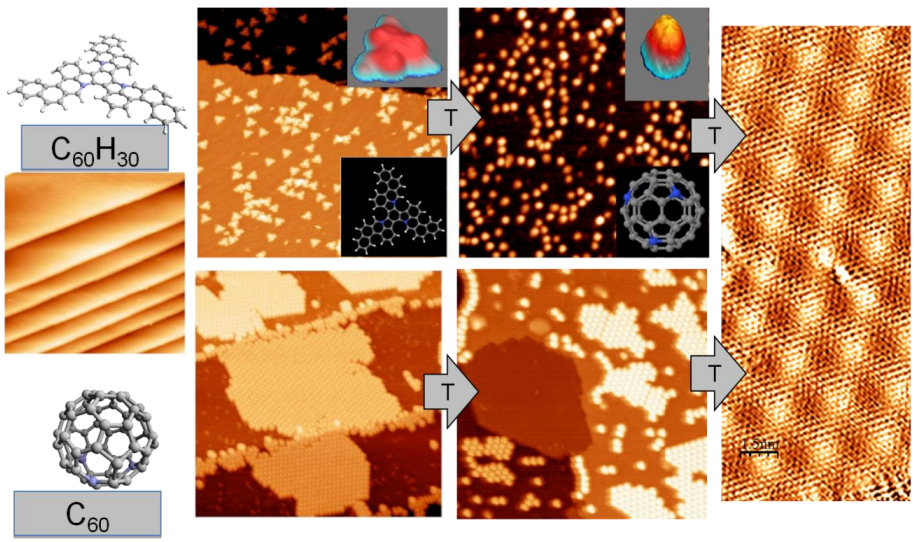

Figure 2 2: *Schematic representation of the process of graphene formation on Pt(111). The C-rich molecular precursors, such as $C_{60}H_{30}$ or C_{60} , are deposited on clean Pt(111) and annealed. Different intermediate states appear upon annealing, but annealing at a sufficient high temperature always yields to graphene formation. The different stages are represented by STM images.*

The standard experiments were carried out in a UHV chamber provided with a commercial room temperature Omicron scanning tunneling microscope and a low-energy electron diffraction system. The base pressure was $1x10^{-10}$ mbar and Pt was cleaned by the conventional

procedure of repeated cycles of argon sputtering and annealing. As usual the first annealing cycles were made in an oxygen atmosphere of $1x10^{-5}$ mbar in order to remove carbon impurities. Commercial C_{60} (provided by Sigma Aldrich, 98 % of purity) were used for the sample preparation. The fullerenes were degassed during hours at 715 K and the sublimation temperature was 725 K. Fullerene deposition rate was calibrated according to previous STM experience and it was estimated to be around 0.4 ML/h. After sample cleaning, C_{60} was evaporated for 30 min. keeping the sample at room temperature. Then sample was later annealed by electron bombardment up to 1200 K in order to decompose the C_{60} molecules. Temperatures were measured using a commercial IR pyrometer. The use of large poly-aromatic hydrocarbons as carbon precursors for graphene growth permits better control of the coverage fraction and induces the apparition of islands with several different orientations.

After this treatment the sample is transferred to the instrumentation in order to be investigated. The LEED pattern is normally checked prior to STM measurements. The diffraction pattern characteristic of G/Pt(111) consist of the one of clean Pt(111) summed with a ring-shaped circle located out of the 1x1 pattern indicating the presence of multiple orientations of a superficial structure with a lattice parameter of 2.4 Å (See **Figure 2 3**).The ring indicates rotational disorder of the graphene layers.

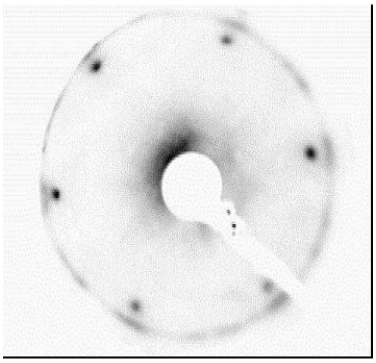

Figure 2 3: *Typical G/Pt(111) LEED pattern with an energy of the incident electrons of 80 eV. Dots correspond to Pt(111) 1x1 pattern and the ring-shaped structure results from diffraction of graphene domains with different orientations.*

After checking the graphene growth with the LEED, the sample is transferred to STM, where flat, homogeneous terraces of graphene layers

are found together with clean Pt regions. Images were recorded using topographic and current modes with typical bias of -2000…2000 mV and currents of 0.1..2 nA although some images were taken with currents up to 4 nA. WSxM software was used for data acquisition and image analysis[29]. We also used homemade drift correction software for hexagonal lattices in order to avoid possible errors introduced by sample movement during scan. This software corrects the images for a given unit cell keeping the fast scan axis distances as the reference one.

One of the main advantages of growing graphene out of big aromatic molecules decomposition, instead of using acetylene or other small hydrocarbons, is that one can easily control the coverage. The use of these molecules and low temperature annealing- but above dissociation temperature- induces the growth of a richer amount of different Moiré superstructures; this is a richer polycrystalline epitaxial graphene sample. Higher temperatures lead to surfaces with a lower number of graphene phases.

Graphene on Pt(111) forms pseudoperiodic structures, Moiré superstructures. A Moiré is the secondary pattern created by the interference of two overimposed lattices. This phenomenon is not only characteristic of graphene overlayer, but it also appears in a wide range of physical phenomena. However, it is very important for graphene grown on transition metal surfaces as it results the main structural motif normally observed in STM investigations. A good example of these systems could be the Moiré appearing on G/Ru(0001) [8]. Normally, only one Moiré superstructure is observed in the G/Ru(0001) system with a periodicity of C(11x11)/Ru(10x10) extracted from local experiments. The determination of the origin of the topological corrugation appearing in the STM images of this superstructure fostered deep investigations in order to discriminate the electronic and topographic contributions. Nowadays it is well accepted that graphene interacts strongly with the Ru(0001) surface in some parts of the superstructure unit cell inducing high structural buckling. On the other hand several graphene Moirés are spotted on the surface of Pt(111) and the interaction between the metal and over layer is considered to be very weak.

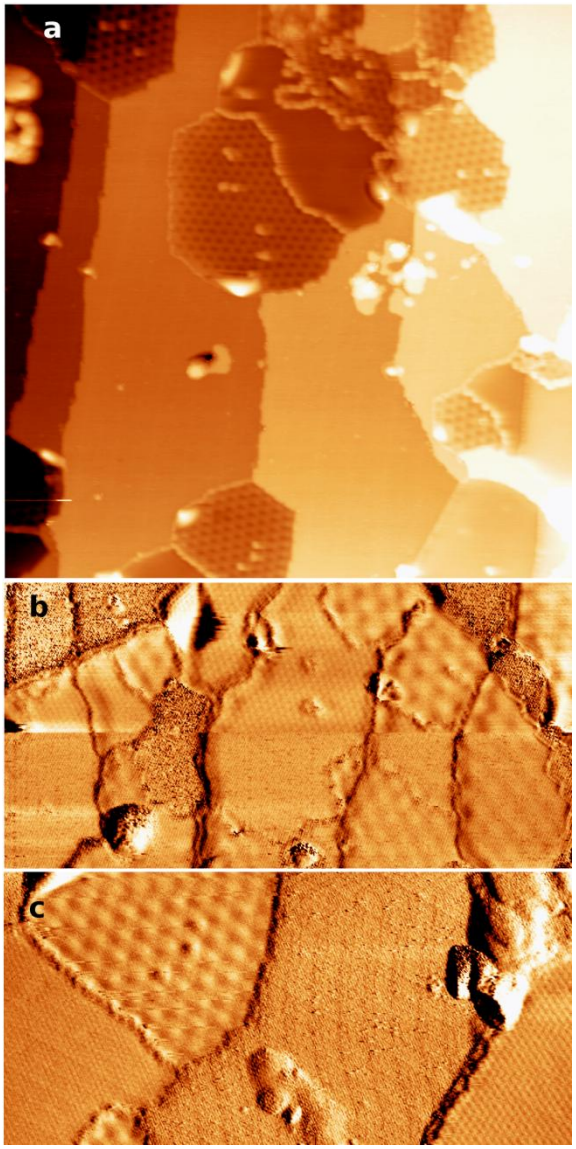

Figure 2 4: *STM micrographs of the G/Pt(111) systems formed using C_{60} as precursors at 1150K.* **a**.*100x100 nm^2 topographic image, V=400mV, I=0.2nA. The flat regions correspond to clean Pt(111) surface whilst the hexagonal corrugated regions correspond to the Moiré superstructures with different apparent angles.* **b**. *50x25 nm^2 signal error image, V=300mV, I=0.1nA . The smooth regions correspond to graphene with different rotational domains, whereas the clean Pt(111) regions look spiky in these imaging mode.* **c**. *50x25 nm^2 signal error image, V=-100mV, I=2 nA.*

Figure 2 4 shows STM images for submonolayer coverage where several domains are imaged on clean Pt(111) regions. Graphene forms different regions with superstructures characterized by the angle between the graphene rows and the Pt [1-10] surface direction. On the surface we found graphene regions with small periodicities ratio (i.e. (√3x√3)R30° and (√7x√7)R19°) coexisting with larger Moiré superstructures. The study of hundreds of atomically resolved STM images of G/Pt(111) prepared following the recipe before revealed a system surprisingly rich in graphene superstructures, in contrast, for example, with the G/Ru(0001) system where mainly a single domain is developed. In **Figure 2 4** we see images where neither the Pt(111), neither the graphene are atomically resolved. Instead, we are able to resolve the periodicity and apparent angle –this is the angle formed between the Pt[1-10] and the Moiré superstructure- of the resulting Moiré superstructures. This is so, because we can estimate the directions of the Pt rows, i.e. Pt[1-10], with the directions of the atomic Pt steps, that normally run parallel to these highly packed directions. It is important to remember that the images shown in this chapter are all obtained at room temperature.

However in some cases we obtain atomic resolution of graphene in addition to resolving the Moiré superstructure and, in exceptional cases - normally when using small tip-sample distances- we obtain atomic resolution of the clean Pt(111) surface. In **Figure 2 5** we show high resolution images of G/Pt(111); in **Figure 2 5 a** we see three different graphene domains coexisting with unresolved clean Pt whereas in **Figure 2 5 b** we see three different Moirés and atomically resolved Pt(111).

Although the coverage can be controlled by the deposition time of carbon-containing precursors and full monolayer growth can be achieved, we focused our work in the submonolayer coverage regime, as it seems to develop larger amount of superstructures. The large quantity of graphene Moirés developed on Pt(111) makes this system an ideal testbed for further molecular deposition. 1-3-5 Triazine deposition on G/Pt(111) showed that the (mostly electronic) Moiré corrugation does not takes an important role in the formation of ordered self assembled monolayers or in the molecular diffusion [30]. Further studies can use G/Pt(111) as a *graphene laboratory* and a source of surface templates of different sizes.

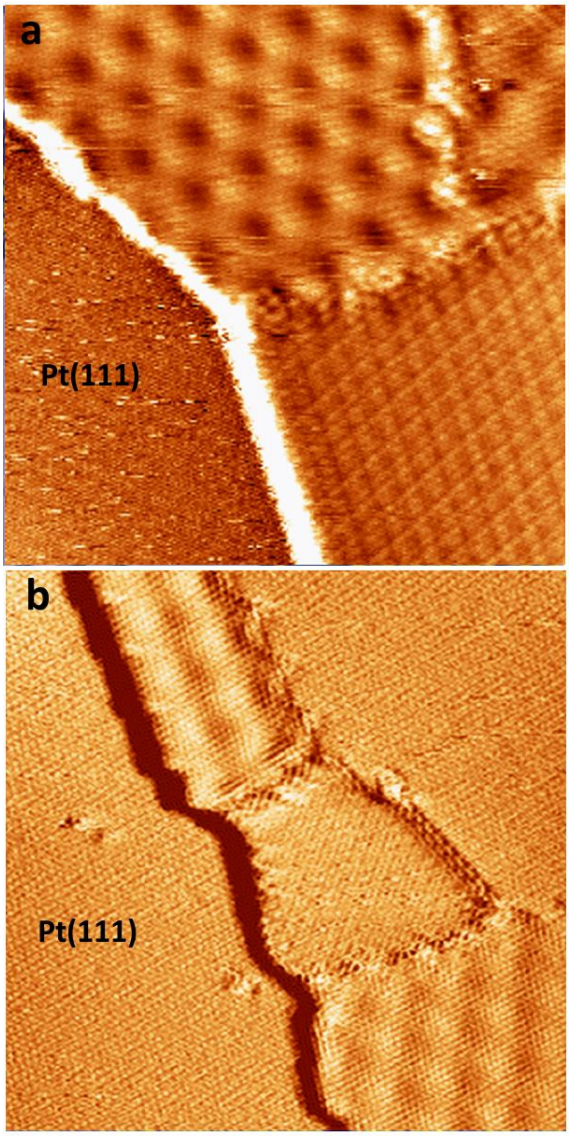

Figure 2 5: *Constant current STM images of submonolayer graphene domains on Pt(111). Different graphene superstructures coexist together with clean Pt regions.* **a***.14x14 nm^2, V=100 mV, I= 2 nA.* **b***. 20x20 nm^2, V=10 mV, I=3.9 nA*

2.2. Strain-driven Moirés of G/Pt(111): Phenomenological model

To describe these coincidence structures we developed a phenomenological model based on geometrical considerations. The model that we propose is illustrated in **Figure 2 6**, where the black spheres correspond to a graphene lattice lying on a single Pt layer (blue spheres) oriented with the Pt[1-10] surface direction along the horizontal axis. After superimposing both atomic networks, with a relative angle between them denoted as Φ (called from now on crystallographic angle, which in the figure is the one formed between black-dotted line and crystallographic Pt[1-10] direction), we observe a nearly-coincidence, i.e. a minimum distance between the carbon and the Pt spheres right below (enlarged in the inset at the top right of the image). The Moiré unit cell is then defined by these two orange points together with the atom at the origin (black lines); the Moiré forms another angle with the Pt[1-10] crystallographic direction that we will call Ω, the apparent angle of the Moiré. The distance between these nearly coincident points, namely the mismatch between the graphene and the substrate, is never zero, but in some cases it is very small. Thus, each Moiré superstructure can be defined by the two angles described above, Φ and Ω, and by the size of the superperiodicity, L, associated with it. It is worth noting that the analysis of an atomically resolved STM image on a Moiré provides with the periodicity, L, but Ω and Φ values can only be precisely determined in small graphene islands (images as the ones shown in **Figure 2 5 b**) where atomic resolution on the substrate and layer is obtained simultaneously. Moreover, L and Ω may be coincident for some superstructures, only differing in the Φ, and therefore usually undetectable in the STM images.

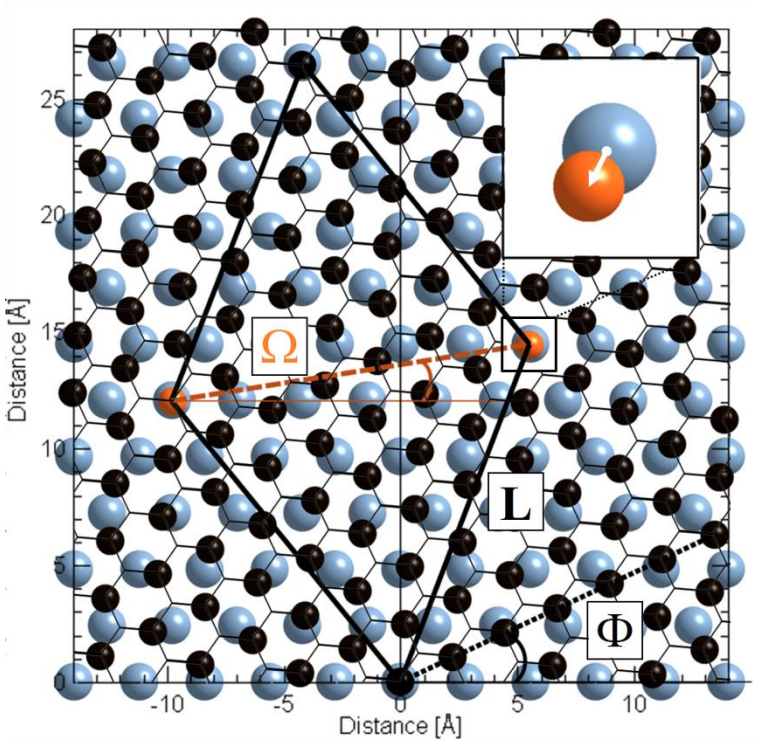

Figure 2 6: *Diagram of the model represented for the ζG/Pt(111) superstructure. Pt atoms are represented by blue spheres whereas the hexagonal lattice of graphene is represented by black spheres. The angle between the black dotted line and the Pt [1-10] surface direction (x axis) represents the crystallographic angle, Φ, which is equal to 25.1° for this particular case. The orange spheres are the carbon atoms with the lowest mismatch, which define the Moiré unit cell for a given Φ indicated by the black rhombus. The angle between the orange dashed line and the Pt [1-10] direction is the Moiré apparent angle (Ω). The white arrow in the inset represents the mismatch.*

We describe the system by two overlaid hexagonal lattices corresponding to Pt (with lattice parameter a_{Pt}= 2.775 Å) and graphene (a_G = 2.46 Å). These are built from the same origin although we checked that the conclusions are independent of the considered origin. To represent graphene we used a simple hexagonal lattice instead of the honeycomb, as we are only

interested in crystallographic coincidences. Nevertheless we also tried honeycomb lattice models with identical results. This counterintuitive result arises from the fact that the honeycomb lattice can also be described as two hexagonal networks shifted one from each other. As we only study crystallographic coincidences we restrain the possibility that the atom of the origin and the coincident position belong to the different hexagonal lattices of the honeycomb one. However, if we allow them, these extra coincidences gives rise to semi-periodicities, which offer no information about the real crystallography of the system and it can be seen as another proof of the non-equivalence between the two atoms of the graphene unit cell.

Thus, we define the position of any atom in the Pt(111) surface using a single vector defined for each lattice point by two integers n and m: $\mathbf{a}^{Pt}{}_{n,m}$. Similarly, we define the vector for the graphene lattice: $\mathbf{a}^{gr}{}_{i,j}(\Phi)$. Where i and j are integer numbers and Φ is the crystallographic angle. This vector is the result of the product of a rotation matrix and the lattice vector. Now we compare both lattices by defining the mismatch, **Δ**:

$$\left|\Delta_{i,j}^{n,m}\right| = \left|\mathbf{a}_{n,m}^{Pt} - \mathbf{a}_{i,j}^{gr}(\phi)\right|$$

So for every Φ and any given graphene and platinum positions the mismatch defines the difference vector between them. The aim of the model is to find for every Φ the i,j,n,m values that minimize the modulus of **Δ** (see **Figure 2 6**) among all possible pairs. It usually exists a particular pair of lattice positions (ij; nm) that presents an extremely good coincidence where atomic positions almost overlap, giving a $\left|\Delta_{i,j}^{n,m}\right|$ value close to zero and consequently they are good candidates to determine the Moiré parameters for that particular crystallographic angle. Therefore the strain of the superstructure comes, in our model, only from the strain of a single pair at the coincidence position. We applied the rotation transformation ranging from 0^o to 30^o with intervals of 0.05^o on the graphene grid and we numerically analyzed the distances between any point in the Pt(111) lattice and any other in the graphene lattice (i.e. the mismatch) searching for the smallest possible mismatch for each angle Φ. Because of the symmetry of

the system, this angular range covers the entire range of possible situations. We selected for every Pt lattice point the corresponding closest graphene lattice position. Among these values, we searched the pairs of points with a minimum mismatch for a particular Φ angle. We found that within this angular range there is usually an angle, Φ_m where $\left|\Delta_{i,j}^{n,m}\right|$ is at its absolute minimum and therefore at Φ_m the mismatch is the lowest

These curves follow a parabolic-shaped behaviour, as indicated in **Figure 2 7**, and can be regarded as existence or stability curves. Following the upward dispersion of one of those curves, there is a point where two adjacent curves cross. On the boundaries of this angular interval the solution 'jumps' to another pair of i'j',n'm' lattice points with a different minimum $\Phi_{m'}$ (corresponding to another parabolic curve). **Figure 2 7** top represents those stability curves, *i.e* the relative mismatch as a function of Φ (we define relative mismatch as the strain of the graphene unit cell: **Δ** /a_{gr}). As the minima of the curves correspond to the angle Φ_m where the mismatch between the coincident points is minimized, the minimum of each parabola should correspond to a superstructure, being the modulus of the associated graphene vector the periodicity of the resulting Moiré (L), showed in **Figure 2 7** bottom as a function of Φ. We assume that the real system tries to accommodate the graphene overlayer with an angular orientation that accumulate the smallest strain, which depends on the mismatch of the best coincident position, as a consequence only the structures at the minimum of the stability curves will be found at the surface. Because our model only takes into account the coincident positions neglecting the rest of atoms, it suggests that the main interaction between the graphene and the substrate comes from the matching points. As we will see in the section **2.5** these results are in good agreement with the nucleation theory of graphene on Pt steps and subsequent growth where the crystallographic angle is determined by this strong bonding region.

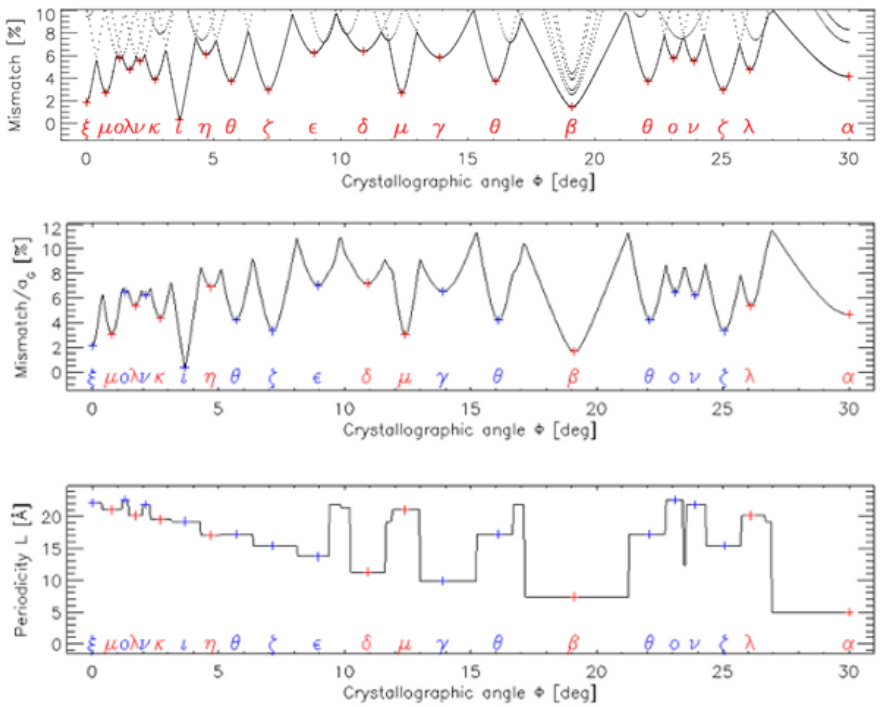

Figure 2 7: *Figure caption. (top) Relative mismatch vs. crystallographic angle (Φ). The solid line indicates the minimum mismatch for the given angle .The dashed lines correspond to coincidence pairs with the lowest mismatc. The blue crosses indicate the stable structures of the model with positive mismatch (tensile stress), while the red ones represent the negative mismatch (compressive stress) phases. These phases are labelled with an associated Greek letter underneath. (bottom) Periodicity, L vs. crystallographic angle Φ.*

We have denoted the calculated strain-mediated Moiré superstructure with Greek letters from the smallest periodicity - αG/Pt(111) to the biggest - oG/Pt(111). This model predicts the existence of 22 stable superstructures. However, only 15 of them are discernable with non-atomic resolution STM images, because for some of them, both their periodicity (L) and the apparent angle (Ω) are the same. All the structural parameters of the phases for the case of Pt are listed in **Table 1**. For a particular lattice

position defining a Moiré, we can have two types of mismatch.**Δ** can be either positive or negative. In the first case, the C-C distance might try to expand in order to commensurate the surface and therefore the layer will be under tensile stress, whereas in the second case the graphene layer may tend to decrease their size leading the layer to compressive stress and introducing in the system either a reduction of the C-C bond or the emergence of out of plane configurations. We have represented in **Figure 2 7** the domains under tensile or compressive stress using labels in blue and red colour respectively.

We have represented in **Figure 2 7** the result of this calculation with a cutoff of the periodicity set to 23 Å since it is the largest periodicity we have found in the STM experiments. The cutoff is an important parameter in our model because it delimits the maximum radius from the origin of the model where lattice positions are taken into account, constraining the L of the resulting solutions. In **Figure 2 8** we show a schematic representation of all the Moirés that come out from our model organized from left to right and up-down by the crystallographic angle.

Figure 2 9 shows the result of classifying all the theoretically found structures in a periodicity vs. apparent angle plot. Every one of the 15 different superstructures of fig. 4a has been represented in the fig. 5 by a rhomboidal tick. On the same plot we have marked the different experimental Moirés found after analyzing about hundred different graphene domains. The total normalized area for every domain is represented by a 2-D Gaussian. **Figure 2 9** shows that all the experimental determined structures can be associated to the 15 predicted ones. Interestingly, the more intense experimental points, which are proportional to their frequency of appearance, are related to the lowest values of the relative mismatch in the stability curves and therefore to the lowest strains (see **Table1**).

G/Pt(111)	Periodicity (Å)	Φ_m(deg)	Ω (deg)	Mismatch/a_{gr} (%)	Strain of the supercell (%)
α	4.9	30	30	4.7	2.36
β	7.4	19.1	19.1	1.7	0.57
γ	9.8	13.9	13.9	-6.6	-1.66
δ	11.3	10.9	0	7.2	1.57
ε	13.7	9	0	-7	-1.26
ζ	15.4	25.1	8.9	-3.3	-0.53
ζ	15.4	7.2	8.9	-3.3	-0.53
η	17	4.7	25.3	6.9	1
θ	17.2	16.1	16.1	-4.2	-0.6
θ	17.2	22.1	16.1	-4.2	-0.6
θ	17.2	5.7	16.1	-4.2	-0.6
ι	19.2	3.7	30	-0.4	-0.05
κ	19.5	2.7	21.8	4.4	0.56
λ	20.1	26.1	13.9	5.4	0.66
λ	20.1	1.7	13.9	5.4	0.66
μ	21	0.8	6.6	3.1	0.36
μ	21	12.4	6.6	3.1	0.36
ν	21.9	2.1	19.1	-6.2	-0.7
ν	21.9	23.9	19.1	-6.2	-0.7
ξ	22.1	0	0	-2.1	-0.23
ο	22.5	1.3	12.2	-6.5	-0.71
ο	22.5	23.1	12.2	-6.5	-0.71

Table 1: *Stable superstructures of G/Pt(111) extracted from the model together with their important structural parameters, ordered with increasing periodicity, L. The strain is defined as mismatch*a_G/L.*

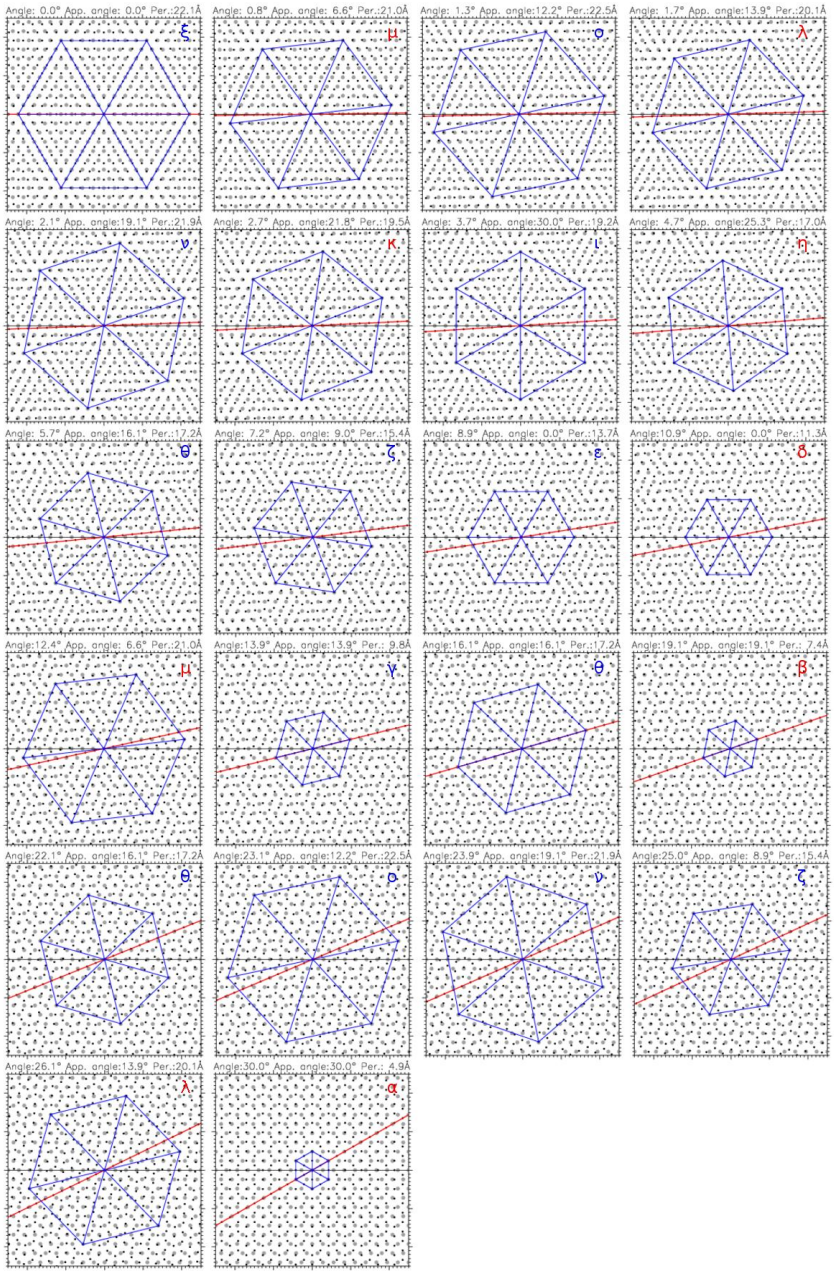

Figure 2 8: *Schematic representation of all the stable Moirés coming out from our model. The crystallographic angle, apparent angle and periodicity appear above every scheme. The order of appearance corresponds to increasing crystallographic angle.*

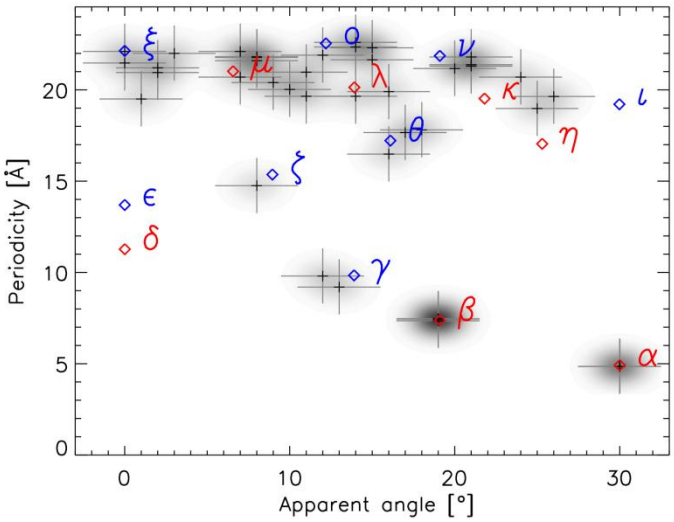

Figure 2 9: *Periodicity vs. apparent angle for measured STM images of graphene islands (crosses) together with the predicted Moirés (rhomboidal ticks and Greek letters). The vertical and horizontal grey lines are the error bars of the experimental determination of periodicities and Moiré angles in STM images, respectively. 2D Gaussian shapes with intensity proportional to the experimental count of finding a Moiré with a given angle and periodicity are superimposed. The interpretation of the figure can be seen as a histogram where the colour intensity of a point is proportional to the occurrence of a structure.*

The agreement between the experimental domains found with STM images and the theoretical phases predicted with our model is very good. In fact, all the experimental phases can be related to a theoretical minimum. **Figure 2 9** shows that there only exist three exceptions that we have not found in the experimental STM sessions. The ιG/Pt(111) is in our model the structure holding the lowest mismatch (see **Figure 2 7** top). Thus, following our previous discussion it should be the most stable phase, and consequently, also the most commonly observed one. However, we have never identified it. This does not mean that it does not exist, but that its stability (evaluated by its probability of appearance) is not connected to the relative mismatch. Indeed this structure was atomically imaged by Sasaki *et al*. [31]

Moreover, we have never observed the superstructures labelled as δ and η. This can be related to their high value of the mismatch (see **Figure 2 7**top), which would lead to less stable structures and therefore less frequently observed. It is remarkable that both structures hold values of the relative mismatch around +7%, and therefore this could be taken as an approximative upper limit of the compressive strain that can be accommodated in the layer.

This model also predicts the formation of Moirés on other hexagonal surfaces different than Pt. We have calculated the stability curves for the hexagonal faces of Ir, Ni, Co, Cu, Pd, Rh and Ru finding the most stable phases after our model correspond to the ones reported in literature. Thus, in Ir(111) 4 Moirés have been reported [22] and 6 superstructures were recently observed on Pd(111) [15]. We have reproduced the four reported periodicities, their crystallographic and apparent angles for Ir(111) and five out of six for Pd(111). Moreover the stability curves (as the one shown in **Figure 2 7**) calculated for Ir and Pd predict superstructures holding minimum mismatch for various angles that have not been reported. We suggest that the use of polycyclic aromatic hydrocarbons as graphene precursors and low temperature annealing may lead to the formation of other unreported phases, as in the case of Pt(111).

At first glance, the domains exhibiting compressive stress shall stretch or experience out-of-plane configurations, whereas the ones submitted to tensile stress might try to enlarge the C-C bond distance. Thus, the measured corrugation for the Moirés with negative mismatch (blue labels in **Figure 2 7**) shall be exclusively correlated to electronic effects. However the relation between the sign of the mismatch and the nature of the experimentally determined corrugation (electronic or topographic) should be treated carefully since other processes can eventually favour the emergence of topographic corrugations in the tensile-strained Moirés. Full DFT calculations for these particular structures combined with good-quality STM measurements could confirm this point.

The good agreement of our model with the experimental data for all transition metals suggests that the weak interaction between the Pt(111)

surface and graphene is sufficient enough to force the system to accommodate into some fixed number of orientations, which minimizes the relative mismatch. The existence of phases with large mismatches leads to the question of how the stress is released throughout the superstructure unit cell. It seems obvious that mismatch accumulation will lead, sooner or later, to interrupt the order of the Moiré unit cell, and therefore they would not be stable. Phases as γ would never be observed because, after a few unit cells, the coincidence structure would disrupt. However, this is not the case and for instance this particular structure is found in extended domain sizes, indicating a full release of the stress within the periodicity of the Moiré. Therefore our model confirms that the stability of the Moiré structures on TM surfaces emerges by the interplay of the local interaction between single C and TM lattice positions, likely due to a favourable adsorption structure, as it has been proposed for Ru by DFT calculations [32] [33]. This is the reason why our model fits better to the relative mismatch than to the total strain of the superstructure (**Δ**/L) and therefore, some high strained phases in the superstructure present relatively high occurrence, like γ or ε phases.

We would like to remark that although most of the stress seems to be relaxed within the Moiré unit cell, this has not a clear relation with the crystallographic unit cell, and some of them could be incommensurate superstructures. The analysis of the commensurability of a superstructure cannot be performed with our geometrical model. Nevertheless, the simplest explanation can be that it exists a second order (or higher) Moiré unit cell with a lower mismatch, longer periodicity and possibly a different apparent angle. The real system would tend to relax completely inside this crystallographic supercell. Atomically resolved images of large regions of the same superstructure could confirm this point.

2.3. Structure of (√3X√3)R30°, αG/Pt(111), or $(2x2)_G$

A different way to release stress is to induce a reconstruction on the Pt(111) surface. We have found that the formation of an ordered network of Pt vacancies at the outermost layer leads to an energetically stable structure compatible with the STM images for the (√3X√3)R30°, or αG/Pt(111) structure [27].

We find that the (√3x√3)R30° structure appears in large areas sometimes covering the whole terrace length (up to 100 nm). The (√3x√3)R30° phase coexists with Moiré regions of different periodicities in the form of crystalline islands (see **Figure 2 10 a**), and it has never been found isolated [24]. **Figure 2 10 c** shows a detailed STM image where the atomic features forming the (√3x√3)R30° reconstruction are clearly identified. These images are characterized by bright points and depressions aligned along the [11-2] surface crystallographic direction. This structure exhibits in the STM images a large atomic corrugation, ranging from 0.60 to 0.15 Å, about 5 times higher than those we obtained for the corresponding Moiré regions in the same conditions (< 0.1 Å). Since electronic effects are important in the image appearance, the atomic assignment of the STM features shown in **Figure 2 10 c** is not trivial and requires the use of first-principles calculations. After trying many different structures (including lateral shifts in the graphene layer, extra carbon atoms, and vacancies in both layer and surface) our best-fit model is depicted in **Figure 2 10 b** and **c.** In this model one surface Pt atom is missing per (√3X√3)R30° unit cell, and the rest of the Pt atoms are alternatively in top or hollow positions with respect to the graphene layer.

Our DFT calculations show that graphene binds more strongly to the platinum surface in the presence of vacancies. The interaction becomes three times larger (-0.60 eV/per unit cell), and the bond length between the C near a top Pt shortens to 2.28 Å (see **Figure 2 10**, side view). The remaining seven C atoms in the unit cell relax outwards, producing a maximum buckling in the C layer of Δz = 0.2 Å. The outermost Pt layer goes from expansion to -8.1% contraction, while deeper layers stay around ±1.0% their bulk-like distances. For the simulated STM images we needed to include multiple scattering terms in order to obtain a good agreement with the experimental observations.

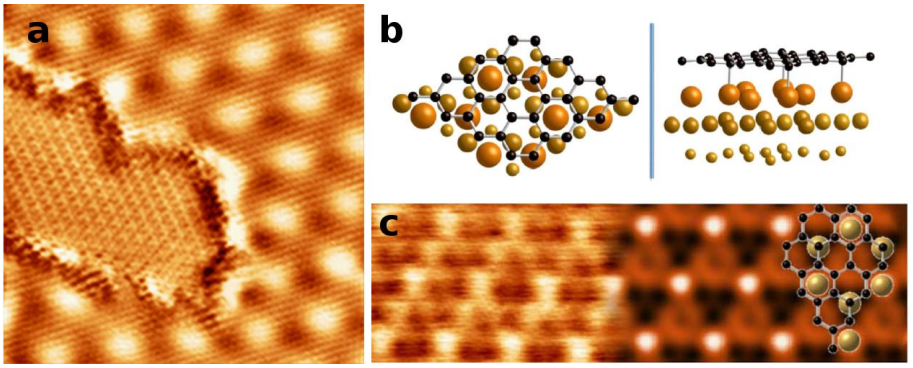

Figure 2 10: a. *12.4x12.4 nm^2 STM image showing an island of atomically resolved (√3x√3)R30º or αG/Pt(111) inside a bigger domain of μG/Pt(111) Moiré.* **b**. *Top view (left) and side view (right) of the structural model derived from DFT calculations for the (√3x√3)R30º reconstruction. Smaller sizes on the orange spheres represent deeper atoms*. **c**. *STM images (V=0.1 V) for the (√3x√3)R30º experimental (left) and DFT best fit simulation (right). A schematic atomic model of where the Pt vacancy network is placed has been overlaid.*

From an experimental point of view this graphene orientation is one of the most commonly observed superstructures occupying an area of around 10-15% of the graphene area while it has a relative big strain as deduced from our phenomenological model (see **Table 1)**. The strain of the supercell, defined as the mismatch divided by the periodicity of the supercell is 2.36%, making this structure the most unlikely to be stable of all the superstructure that came out from our model. We believe that the surface reconstruction through an ordered vacancy network is an atomic mechanism that stabilizes the system in an energetically more favored atomic configuration.

The formation of vacancies on metallic surfaces upon C_{60} deposition -normally followed by a soft annealing- is a well known process in a wide range of transition metals. It was first discovered after investigations by means of surface X-ray diffraction on the (√13x√13)R13.9º reconstruction of C_{60}/Pt(111) [34], but the mechanism was previously proposed for the (6x6)-C_{60}/Al(111) [35] reconstruction. Since that discovery, many experimental and theoretical efforts have successfully been performed in the search of atomic vacancies on metallic surfaces. Nowadays it is believed that the formation of vacancies on close-packed metal surfaces upon C_{60} deposition is the rule rather than the exception [36]. The formation of vacancies

structures might also be a mechanism of stress relaxation in some graphene superstructures and determined rotational domains, as in the case of (√3x√3)R30^{o}-G/Pt(111) and the reason why some Moiré structures are more common than others.

2.4. Structure of (√7X√7)R19º, βG/Pt(111), or $(3x3)_G$

The most commonly observed graphene superstructure on Pt(111) is the (√7X√7)R19º Moiré. This Moiré is very characteristic as it is one of the small periodicity (7.4Å) and it corresponds with a graphene $(3x3)_G$ commensuration. Again, this is only the average distance and because it is a pseudo-periodic structure these numbers must be taken with caution. In **Figure 2 11** we present four STM images of this Moiré obtained under different tunneling conditions (more precisely, different bias voltages). It results clear that this structure shows a bias dependence under STM imaging. The closer we are to the Fermi level, the narrower the bright pockets. This behavior might be an indication of the graphene-metal interaction as a similar behavior has been observed for the highly interacting system G/Ru(0001) [8]. It is important to recall that the interaction between G and Pt has been described to be much smaller than for Ru [21]. Nevertheless freestanding graphene would never present a hexagonal symmetry disruption in its density of states that could yield to the observed bias dependence behavior, and therefore we can conclude that in this rotational domain some small G-Pt interactions is occurring.

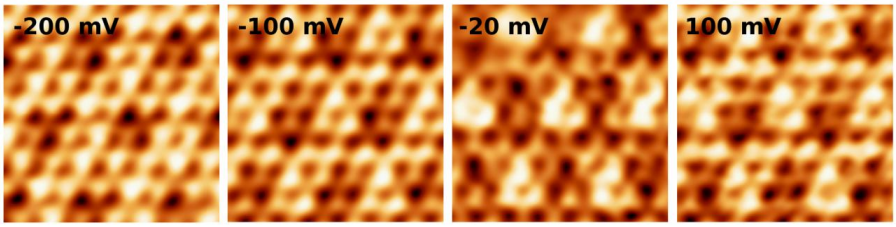

Figure 2 11: *Series of 2x2nm² STM images of the (√7X√7)R19º Moiré taken at different bias voltages. The bias is written in the upper part of the image. The bias dependence is clearly seen as the bright pockets get narrower near the Fermi level.*

We have also performed DFT calculations of this system, these calculations involve a large number of atoms and thus they are vey time computing consuming. The theoretical framework used for this system is as follows: First the graphene unit cell of periodicity (√7X√7)R19º on Pt (111) is set free to relax with regular DFT under the FIREBALL package. Once the system´s energy minimum is found (i.e. the calculation converges) we use the relaxed structure as the departure point for calculating the van der Waals corrections. When these two steps are performed we consider that the system correctly includes all the physical interactions. Van der Waals

corrections results in a decoupling of the graphene layer from the substrate and an increase in the G-Pt distance up to the final value of 3.1Å where the layer stabilizes and a geometrical buckling of the graphene layer of 0.16 Å. In **Figure 2 12 a** we present an extended representation (i.e. four times repeated the unit cell) of the resulting structure together we a simulated STM image of the resulting structure. We can observe that the simulated STM image reproduces the $(3x3)_G$ periodicity perfectly and that the agreement with the experimental imagers is fairly good.

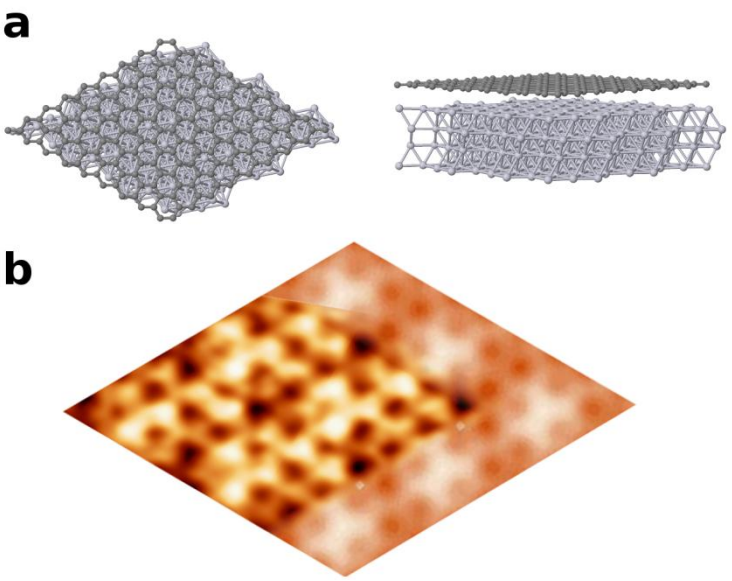

Figure 2 12: *Extended structure of the (V7XV7)R19^o Moiré.* **a***. Ball and stick model of four contiguous unit cells .***b***. Simulated STM image at 0.1V bias for the extended structure where the $(3x3)_G$ periodicity is clearly resolved together with an experimental image taken at 0.1V.*

In the next sections of the chapter we will describe the G-Pt edge where this Moiré nucleates and we will discuss how the strong chemical bond between the outermost graphene atoms and the Pt atoms in an atomic step determine the growth of this Moiré.

2.5. Edges between graphene and Pt(111) steps and its relation with Moirés

THE FOLLOWING STM IMAGES ARE REPRESENTED IN FALSE COLOR TO EASE THE DATA INTERPETRATION. IN THIS COLOR SCHEME, BLUE REGIONS STAND FOR CLEAN Pt(111) REGIONS WHILE GREY REGIONS STAND FOR GRAPHENE.

Graphene theoretically is a 2D infinite material. However in real systems this is not feasible and the layer is finite. The terminations of the flakes –the graphene edges- rarely are amorphous and normally present large straight regions following some crystallographic directions. The most common endings of graphene edges are the so called zig-zag and armchair endings, this is true for graphene from HOPG [37] and also for epitaxial graphene on metals [25]. In **Figure 2 13** we present an example of these terminations. Moreover, when growing epitaxial graphene on metal substrates we have the possibility to study not only the edges "flying freely" on the lower substrate terrace (*step-like* edges) but also those bound to the upper terrace of the substrate (*border-like* edges).

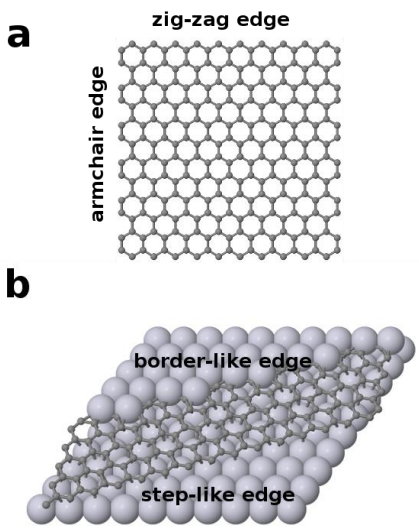

Figure 2 13: *Schematic representation of the different graphene edges.* **a***. zig-zag and armchair .***b.** border-like, bounded to the uppermost terrace and step like, lying on top of the bottom terrace.*

The –rather good- agreement between our phenomenological model presented previously, and the experimentally found Moiré superstructures needs a deep discussion in order to find out the physical processes that are involved in the stability of the Moirés. In principle the validity of the model might suggest that the whole pseudo-unit cell of the Moiré is an entity energetically favored entity over any form of incomplete supercell. We can establish this from the scientific fact that epitaxial graphene islands are normally holding full unit Moiré unit cells on their boundaries, rather than amorphous termination. Although we can also find islands terminations finishing in incomplete unit cells (see for example the upper domain of **Figure 2 5 a**) the rule is that islands are hexagonally shaped. This might indicate than there are pinning points in the unit cell where some atoms of graphene interact strongly with the substrate. Recent high temperatures STM investigations during graphene growth on Rh(111) show that it exists a growth mechanism where the graphene layer increases its area by discrete adding of single Moiré unit cells. Another way to see it is that they grow following the crystallographic directions of the Moiré [38], thus opposed to the dendritic growth of , for example surface carbides [39].

Although the stability of the Moiré pseudo-unit cell might be favored over other possible configurations through pinning points or areas of interaction within the Moiré, it remains the question of why, and how, does the graphene form rotational domains on Pt(111) and other metals. On most hexagonal transition metal surfaces graphene grows with a crystallographic angle of 0^{o}, this means that the graphene and the substrate crystallographic directions are aligned and the resulting superstructure accumulates the stress of the difference between the lattice parameters of G (2.46 Å) and the surface Moiré lattice constant in a configuration typically of the form $(n \times n)_{Pt} - (n+1 \times n+1)_{G}$. This, so called aligned Moiré, also exists on the Pt(111) surface as the ξG/Pt(111) phase or $(8x8)_{Pt} - (9x9)_{G}$ structure ,but it is not as common as, for example, on Ir(111) or Ru(0001) where most of the experimental results refer to this aligned Moiré superstructure. The question of why the graphene layer acquire a non-zero angle results non trivial. In principle, it might be possible that the rotation arises from thermo dynamical effects during annealing. Then when the annealing is turned off the layer evolves to the crystallographic angle corresponding to the local minimum closest to its angle.

A second possible explanation of why our simple model works is not related to kinetic effects but rather to energy considerations of the atomic bonding configurations during the nucleation of the graphene islands. It is not clear

whether or not graphene nucleates with the same mechanism on different metal surfaces and several mechanism have been theoretically and experimentally proposed [39] [40]. However it is established that nucleation on step edges is one of these possible mechanisms. Moreover the bonding between the island and the graphene edge seem to determine the periodicity of graphene on Ir(111) [41]. In the present section we will demonstrate that this is also occurring for the case of G/Pt(111) and that our phenomenological model can be seen as a model for determining the possible stable edge structures and thus the most likely Moirés to be formed.

STM analysis of several G-Pt(111) edges reveal that the –rather large- amount of stable Moiré superstructures on Pt(111) can be correlated to the crystallographic border edges of the graphene islands. Rotational domains seem to nucleate on Pt steps through chemical bonding of the outlying atoms of the graphene islands with the Pt atoms on the substrate step. This strong binding fixes the particular orientation which determines the crystallographic angle. The sheet thus continues its growth with this direction.

Analogous to the standard notation used for nanotubes, we can denote the crystallographic interfaces with a couple of chiral vectors (defining a chiral vector as for nanotubes: two integers n and m denote the number of unit vectors along the two crystallographic directions of the surface crystal lattice) one for Pt and other for the graphene (edge). With this notation, the step shown in **Figure 2 14** between Pt and G, can be denoted as $(1,2)_{Pt}(3,0)_{G}$ (see the eye guide in the inset); this is the interface between the (√7x√7)R19°-G/Pt(111) Moiré (also called $(3x3)_{G}$, or □G/Pt(111)) and a Pt step. Other Moirés-Pt interfaces have different pairs of vectors in the form $(n,m)_{Pt}(i,j)_{G}$. We believe that any stable Moiré must possess a combination of vectors satisfying our phenomenological model [17]. Thus our model results in a first approximation of the possible pairs of existing chiral vectors which minimize the strain and thus the most likely to be stable. However we have noted that some defective zones in the G-Pt interface might appear obscuring the crystallography of both, the edge and the Moiré of the island that is attached to it.

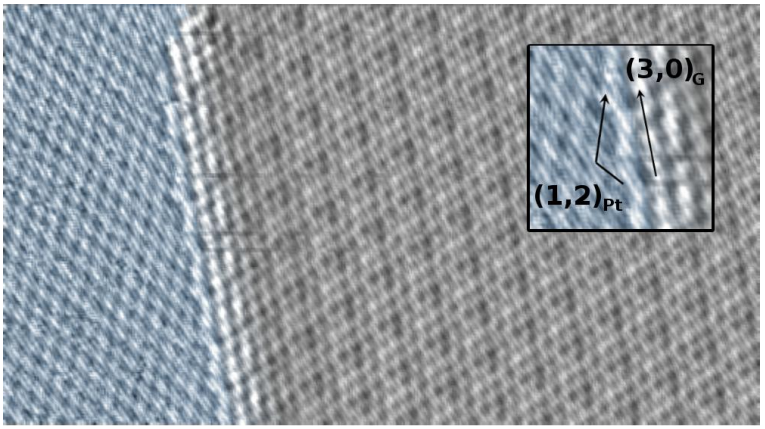

Figure 2 14: *High resolution, atomically resolved, STM micrographs of the 6G/Pt(111)-Pt(111) interface. These crystalline edges are energetically favored and might be determinant in the orientation of the possible Moiré superstructures. 12.6 x 6.8 nm^2, V=40.2mV, I=5.2 nA. The inset shows the chiral vectors of this particular edge.*

The study of the crystallographic parameters of the Moiré superstructures by STM images is a difficult task, because simultaneous atomic resolution in both graphene and metal surface is required. It is important to notice that normally STM images lack the information about the commensurability of the Moiré superstructures. Even though we could say that near the graphene-Pt interface the structure is commensurate, nothing could be said about zones far apart from the edges, as the accumulation of mismatch will either disrupt the long range order of the Moiré superstructure or induce defects – such as, for example, ripples, vacancies, or domes- formation. In **Figure 2 15 a** we see a small epitaxial graphene island grown attached to a Pt step; as usual, it is hexagonally shaped and it appears with part of its area inside the upper Pt step, indicating some form of mass transport during graphene growth. Looking carefully to the lower left part of the image we see what does look like a graphene nanobubble. The mismatch strength accumulated in such a small island promotes the formation of a 6x3nm^2 nanobubble.

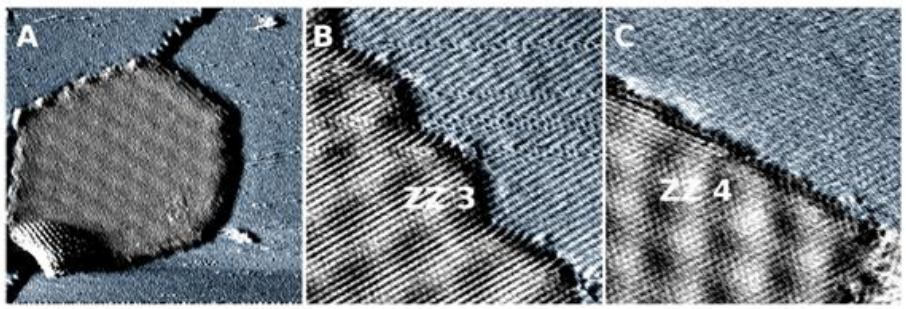

Figure 2 15: a.*STM image showing a graphene island, a nanobubble can be seen in the lower part. 34x34nm^2, 1.9nA, 100mV.* **b.** *Detail of a crystalline edge with a graphene zig-zag termination, 10x10 nm^2, 3.94nA, 10mV.* **c**. *Detail of a crystalline edge with a graphene zig-zag termination, 10x10 nm^2, 3.94nA, 10mV.*

Figure 2 15 shows STM images of 3 border-like resolved crystalline edges giving rise to other Moirés superstructures. **Figure 2 15 b** and **c** correspond to moiré patches of ξG/Pt(111) and μG/Pt(111) respectively. Using the chiral vector notation introduced before, these edges correspond to these pairs of chiral vectors: $(8,0)_{Pt}$ $(9,0)_G$ for **b** and $(7,1)_{Pt}$ $(8,1)_G$ for **c**. These edges involve large number of atoms, and they escape the capabilities of regular DFT calculations (contrary to the edge in **Figure 2 14** that will be discussed in detail later). However, optical inspection gives some interesting information about morphology and stability aspects of these bigger G-Pt edges. At a first sight it seems graphene ends preferentially on a zig-zag configuration. Hence the Pt atoms adopt the configuration that yields the maximum G ending in zig-zag configuration as possible; this leads to a situation where the graphene crystallographic directions are parallel to the Pt outer atoms and thus the last carbon atoms in the graphene flake are in a zigzag configuration.

Figure 2 16 illustrates this point. In this figure we have schematically reproduced edges similar to ZZ3 and ZZ4 of Fig. S5, another hypothetical ZZ edge (called ZZX) and an amorphous edge. Graphene prefers to stabilize its edges by maximizing the number of the -energetically favored- zigzag edges. The amount of the armchair regions needed in the interface (marked in the figure by a red oval) depends on the angle between G and Pt (and therefore the angle between the Moiré and the Pt). We observe that the more often found graphene edges are those which have maximized the number of zigzag units versus the armchair, thus, in Fig. S6, ZZ4 will be

preferred versus the A edge (although both are rotated of 6º). A termination is exclusively observed in defective regions of the G-Pt edge. (like A2 in fig. 2)

The fact that the system tends to maximize the number of C atoms ending in zig-zag configuration for a given edge has an interesting secondary effect. This tendency in the edge stability induces, in the overall distribution, Pt edges ending parallel to the apparent angle of the Moiré. This means that if we ignore the local relaxation of individual Pt atoms, the overall imaginary line delimitating the interface between graphene and Pt is parallel to the Moiré high symmetry axes. This might look simple, but involves that –normally, and in absence of defects- the Pt-Graphene edge is not parallel to the graphene crystallographic directions or to the Pt ones. This can be very useful for determination of the structure of unknown rotational domains with large scale STM or AFM images, even when the periodicity of the Moiré is not resolved. One has to measure the angle between the G-Pt edge and the clean Pt steps, then go to the list of Moirés and find which of them possess that particular apparent angle. However, one has to be very careful if using this method for Moiré determination, as –according to our model- there are normally more than one Moiré with a similar apparent angle, i.e. there are more than one rotational domains with different crystallographic angles yielding Moirés with different atomic structure but the same apparent angle [17].

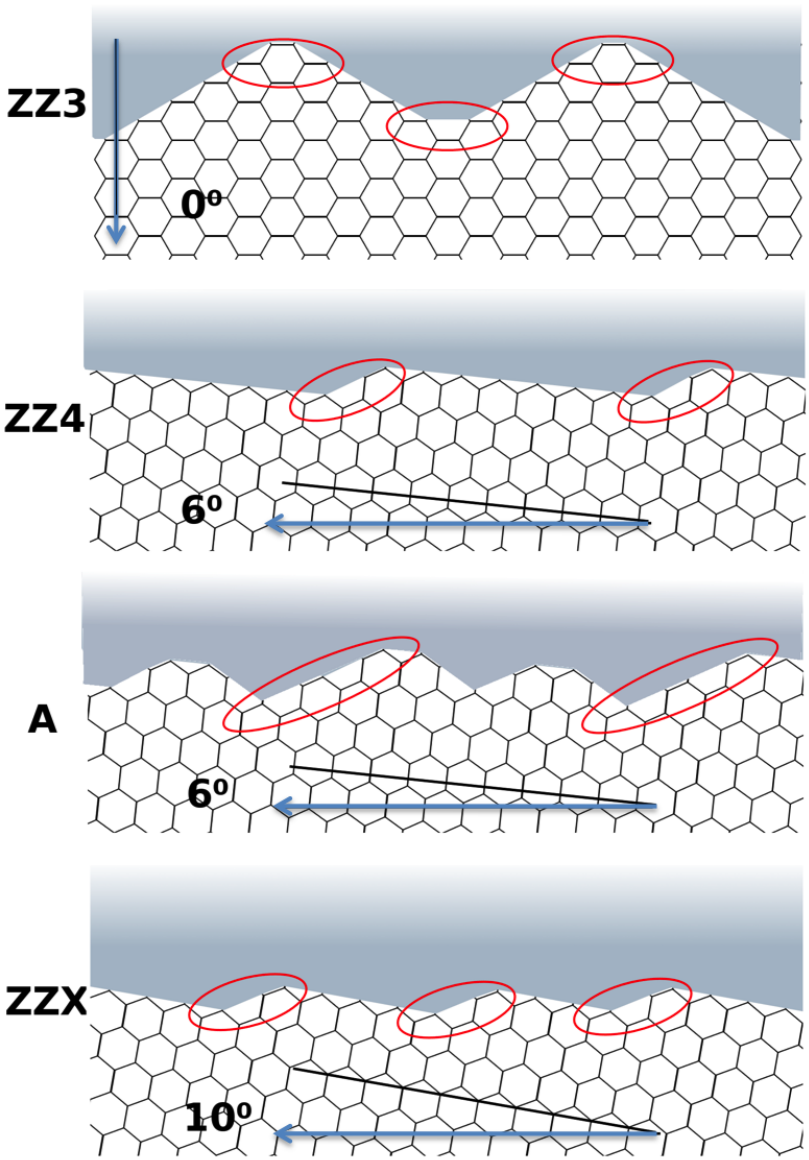

Figure 2 16: *Schematic model of the preferred graphene termination of border-like at the G-metal interface. The blue side corresponds to the Pt region, with crystallographic direction, indicated by a blue arrow, along the horizontal (except for ZZ3, where it is along the vertical). The graphene tends to adopt zigzag configurations by minimizing the number of armchair unit cells for a given crystallographic angle with respect to the Pt surface. Armchair configurations are marked with red ovals.*

The case of the edges between (√7x√7)R19º graphene and Pt described in the next section has the –rather rare- chance that the apparent angle and the crystallographic angle are both the same, i.e. 19º,and thus it wrongly seems that the edges are parallel to the crystallographic directions of graphene. The cases of **Figure 2 15 a** and **c** or the cases of the islands shown in **Figure 2 17** are the rule. The edges run parallel to the Moiré *crystallographic* directions – if one can talk of crystallography of a Moiré-. One can notice that the edge shown in **Figure 2 15 b** is an exception; In this interface the Moiré runs parallel to the edges of the small triangular protrusions appearing at the interface but seems perpendicular to the overall landscape of the edge. We believe this because the Moiré is the so called ξG/Pt(111) or $(8x8)_{Pt}$ –$(9x9)_{G}$, and is the exceptional case of the aligned Moiré (where the crystallographic angle is 0). According to the rules that we observe for the rest of Moirés the *normal* edge would be an structure running parallel to both Pt[1-10] and the graphene high symmetry axis in straight line. This structure would be straight both in Pt and G and might accumulate high amounts of strain yielding to a highly unstable structure. The edge then might thus relax in the peak protrusion that can be seen in **Figure 2 15** to minimize its energy.

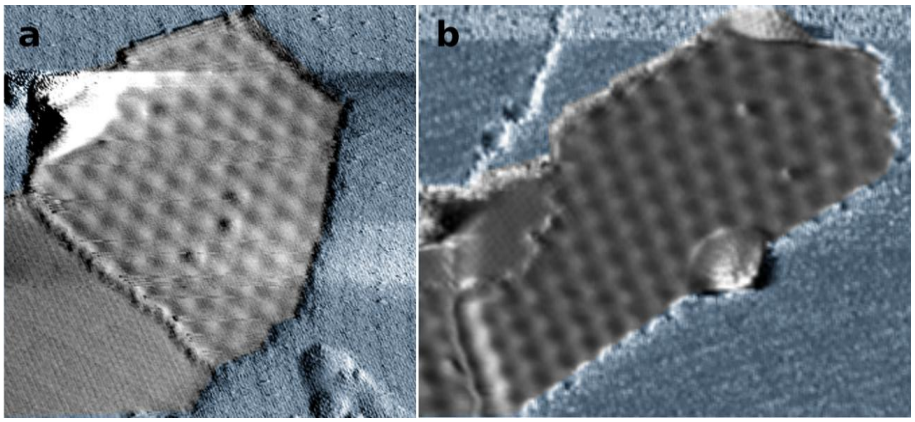

Figure 2 17: *STM images showing graphene edges running parallel to their Moiré apparent angles. Nanobubble or graphene folds can be seen in the islands.* **a***.30x30nm², 2nA,-100mV.* **b***.30x25nm², 1nA, 50mV.*

The apparent angle of the Moiré is the same than the angle of its edge in most cases, it exists a relationship between the growth of a determined

Moiré and the crystallographic border-like edges and they may be an important factor in the determination of the permitted orientations of graphene epitaxially grown on Pt(111). However it is important to notice that other kinetic effects, such as the formation of defects or folds due to the shrinking occurring during the cold-down after the growth annealing (arising because the differences in thermal expansion coefficients between graphene and the substrate) may take also a role in the determination of the atomic configuration of the final shape of the edges.

2.6. 1D sublattice electronic states in (√7x√7)R19º G-Pt(111) boundaries.

Among all the crystallographic edges that we have experimentally determined it exists one that we have analyzed in detail. This is the case of the lateral interface between (√7x√7)R19º G/Pt(111) and Pt(111). This Moiré reconstruction is the second smallest of all the possible on Pt(111) and thus it is affordable for first principles calculations. Understanding the connection of graphene with metal surfaces is a necessary step for developing atomically-precise graphene-based technology. Combining high resolution RT-STM experiments and DFT calculations we have unambiguously unveiled the atomic structure of the boundary between a graphene zigzag edge with (√7x√7)R19º, or βG/Pt(111) and a Pt(111) step. This graphene edges minimize their strain by inducing a 3-fold edge-reconstruction on the metal side. Moreover we have determined the theoretical electronic structure and we have found the existence of an unoccupied electronic state localized in the edge C atoms of one of the two graphene sublattices. This state extends few angstroms, thus few unit cells, inside the graphene layer.

The exceptional electronic properties of exotic graphene structures with a dimensionality lower than 2 has recently attracted the attention of the scientific and technological community as possible basic components in future atomically-controlled graphene-based nanoelectronics [12] [42]. The breaking of the 2D periodicity in the presence of topological defects or in strain relief structures modifies significantly its electronic properties [43] [44] [4] [6]. In particular, graphene nanobubbles have been suggested to present pseudo-magnetic associated landau-levels [42], electronic one-dimensional edge states have been revealed to be localized in graphene nanoribbons [45] and missing atoms have been proposed as a source of carbon magnetism [46]. Thus, these recently developed nanoarchitectures could open the door to tune the electronic transport properties of graphene-based electronic devices by ribbon, boundary or defect engineering.

Graphene edges, rich in exotic properties, are central to this effort. Electronic transport through grain boundaries of polycrystalline graphene [47] or graphene nanoribbons (GNRs) has been extensively studied [48] [49]. Theory predicts that the electronic properties of the edges can be tuned by the orientation of its ending (zig-zag, armchair, mixed), possible reconstructions (pentagonal, heptagonal and higher order rings), and their chemical functionalization (normally H passivation) [50] [51]. Electron microscopy

experiments were the first to provide a structural characterization of graphene edges with atomic resolution using either aberration-corrected TEM images [52] or scanning transmission electron microscope (STEM) [53]. STM measurements based on graphene patches deposited on different substrates [45 54 55 56] added the possibility to correlate the structure with the local electronic properties. Even though atomic resolution was achieved in those experiments, STM was unable to reveal the details of the edge termination due to the interaction with the substrate. Only recently, Zhang et al [57] have shown that hydrogen plasma etching of the nanoribbons induces hydrogen-terminated rough edges that lie flat on the substrate and where different endings (zigzag, armchair, chiral) can be resolved. STM experiments based on graphene islands grown directly on a metallic substrate [41] offer the possibility to study not only the edges "flying freely" on the lower substrate terrace (*step-like* edges) but also those bound to the upper terrace of the substrate (*border-like* edges). Although this study was able to show a correlation between the atomic corrugation at the graphene edges with the Moire pattern of Gr/Ir, an atomically precise description of graphene contacts with metallic substrates was still missing.

In this section we provide a combined experimental-theoretical atomistic description of the contact region formed along the interface in a graphene-metal heterostructure and we unveil its electronic properties. We have been able to obtain high-resolution STM images of atomically resolved *border-like* edges of (√7x√7)R19^{o} graphene on a Pt(111) step. We have combined these detailed experimental results with DFT simulations to fully characterize the atomic structure of the Pt-graphene edges and to understand their electronic properties. This approach reveals the presence of 1D electronic highly localized state in one- and only one- of the graphene sublattices. Theory predicts, and constant height STM images confirm, that this state is mainly confined on the first carbon atomic lines of the edge.

The topographic STM image on **Figure 2 18 a** shows a graphene island which grows attached to the upper part of a Pt(111) step. The usually straight Pt step-edge has been altered from its original shape during the graphene growth. In this image, half of the graphene island is embedded in the upper terrace, adjusting itself to the crystallographic directions of the substrate. This morphology indicates significant mass transport of Pt atoms during graphene growth and differs from the structures reported for graphitization on other metal surfaces, such as Ir(111) [16] or Ru(0001) [7], where graphene grows over the metal steps without altering the metal substrate.

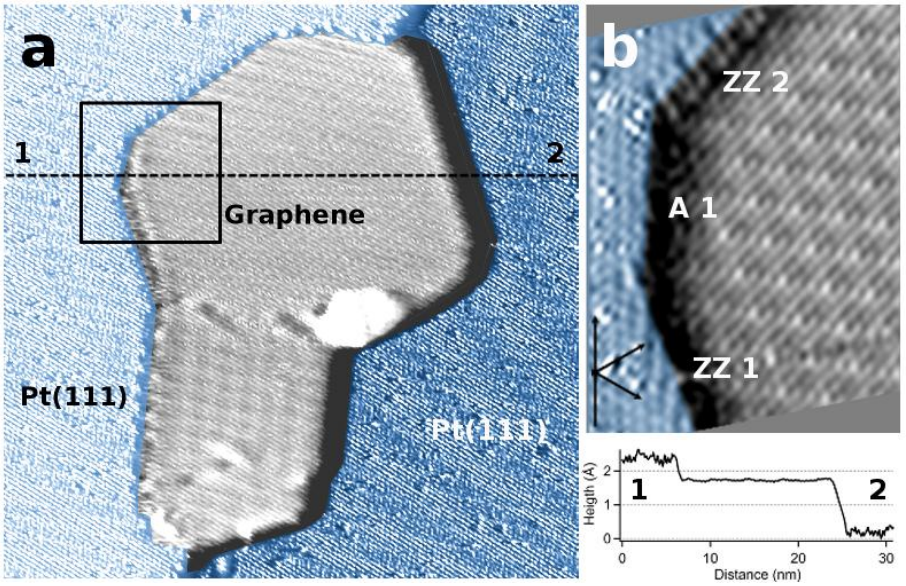

Figure 2 18: a. *Topographic STM image (31x31nm^2, sample voltage V_s = 100mV, tunneling current I_t = 3.9nA) showing a graphene island embedded in a Pt(111) terrace exhibiting three different Moirés.* **b**. *Drift corrected current (signal-error) STM image (6x8nm^2, V_s = 42mV, I_t = 2.5nA) displaying a detailed view of three border-like edges of the squared region in* **a***). Black arrows indicate the [1-10] Pt crystallographic directions.* c. *Topographic profile corresponding to the dashed line marked in (***a***).*

Focusing now on the structure of the island, three different rotational domains of graphene separated by non-periodic grain boundaries can be clearly identified. The upper domain in **Figure 2 18 a** corresponds to (√7x√7)R19^o , $(3x3)_G$, or βG/Pt(111). Its cryrstallographic angle is 19.1^o with respect the surface [1-10] crystallographic direction, which in the image runs parallel to the vertical direction, and it exhibits a superstructure periodicity of 7.38 Å [17]. The middle domain is rotated 8^o and present a periodicity of 12.6 Å; it most likely corresponds to εG/Pt(111). Finally, the lowest domain is small in size and unfortunately, we were not able to attain moiré resolution to deduce the graphene orientation.

The upper (√7x√7)R19^o domain exhibits an polygonal shape with four *border-like* and four *step-like* edges [41]. In order to enhance the resolution on the graphene boundaries we have recorded current-error STM images.

Both, STM topographic and current-error images show the same atomic features on the same positions, but the latter mode allows an enhanced resolution. In **Figure 2 18 b** we see the high resolution current-error STM image of the region marked with the black square in **Figure 2 18 a** (drift corrected for avoiding thermal distortions of the image), we achieved atomic resolution not only on the Pt(111) terrace and the island but also on the interface. In this particular region, we find three different *border-like* edges where graphene binds to platinum atoms of the step edge.

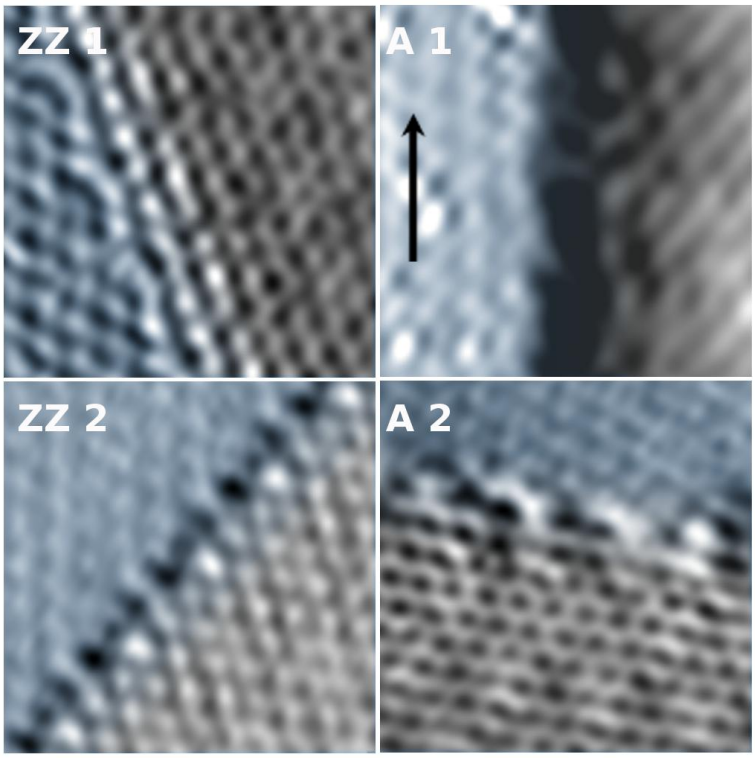

Figure 2 19: *Atomically resolved current (signal-error) STM images of: ZZ1) the zigzag edge number 1; I_t = 5.2nA, V_s = 38mV; A 1) the amorphous edge number 1; I_t = 2.4nA, V_s = 42mV, the arrow indicates the Pt[1-10] direction; ZZ 2) the zigzag edge number 2; I_t = 3.8nA, V_s = 47mV; and A 2) the amorphous edge number 2; I_t = 5.2nA, V_s = 38mV. Blue/grey regions are identified by the lattice symmetry to be Pt/G respectively. A boundary region of 3-4 atomic rows is also clearly observed with atomic resolution. These images have been drift corrected and FFT filtered.*

High-resolution current signal-error STM images allow a systematic characterization of all of the different border-like edges on the (√7x√7)R19º graphene Moiré shown in **Figure 2 18 a**. These results are shown in Figure 2 19, where edges have been labeled as ZZ (for a zig-zag graphene ending) and A (for an amorphous or armchair configuration). Border A1 is parallel to the [1-10] Pt crystallographic direction while borders ZZ1 and ZZ2 run along the [3,-2,-1] and [1,-3,2] directions respectively, forming 19º and 41º degrees with the [1-10] direction. A1 and A2 edges present a disordered structure whereas the other two, ZZ1 and ZZ2, are crystalline at both sides. A2 border presents a mixture of armchair and zig-zag termination.

Edges ZZ1 and ZZ2 show regions that can be unambiguously assigned to Pt and G (blue and gray colored areas on Fig. 2, respectively) and a boundary area, of 3-4 atomic rows, where the atoms although clearly visible cannot be directly ascribed to Pt or C (gradient colored area). Only *Ab-initio* simulations based on DFT for a similar graphene flake attached to a Pt step allow a full understanding of these edges. **Figure 2 21** shows the main results of these calculations performed by the Scanning Probe Microscopy Theory & Nanomechanics Group of the UAM. Starting from different initial structures for the G-Pt interface, we have obtained a stable configuration where the stress induced in the graphene-Pt junction has been relaxed with a rearrangement of the outermost Pt atoms of the single-atom step (see **Figure 2 21 a** and **b**). The unit cell of our system involves three non-equivalent Pt atoms directly bonded to graphene. To ease the visualization we have marked them with blue, red and green colors. These Pt atoms undergo both out-of and in-plane displacements. The red Pt atom on Fig. 3 protrudes 0.65 Å out of the Pt terrace plane and it moves in plane from its original position ~1 Å towards the graphene forming a bond with an unsaturated C edge atom. As a result a hole is created on the Pt side. This can be visualized in **Figure 2 21 a** as the vacant region beneath the red Pt atom. The blue and green Pt atoms also passivate one outermost C atom each but they show lower strains and displacements, the more significant being the -0.15 Å out-of-plane displacement (inwards relaxation) of the blue atom on **Figure 2 21**.

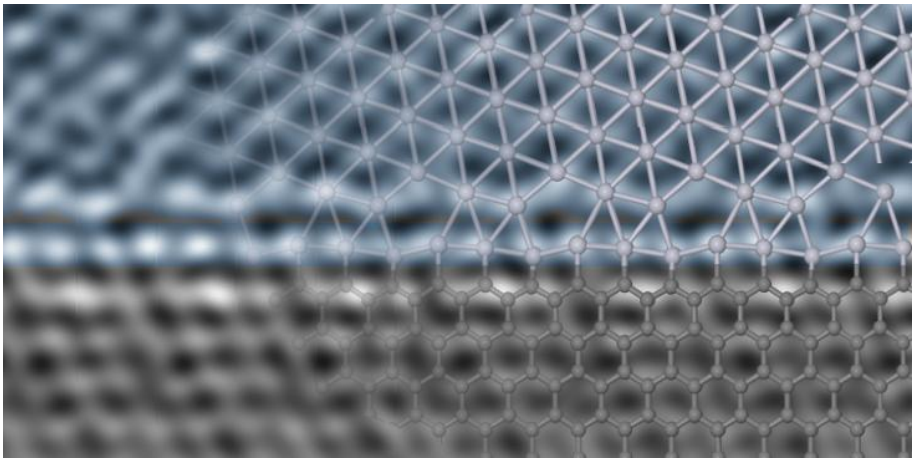

Figure 2 20: *Ball and stick model of the DFT relaxed structure compared with the false colored STM image. The atomic positions of the calculations reproduce with great accuracy the protrusions in the STM images.*

This atomic structure mimics with great accuracy the atomically resolved experimental STM images (see **Figure 2 20** and **Figure 2 21c**). The strain induced on the Pt side is localized mainly on the outermost Pt atoms and only slightly propagate to the 2nd Pt row. While free-standing zigzag edges should undergo reconstruction, no relevant rearrangement is observed on the graphene side in the theoretical results. The three external C atoms of the zigzag edge are covalently bonded to the metal step, keeping their graphene-like positions. This covalent interaction between graphene and Pt, already theoretically proposed for Cu, Co and Ni(111) surfaces [40] [58] [59] and observed with STM on G/Ir [41], passivates the graphene dangling bonds and stabilizes the zigzag structure [58]. Our calculations have found another stable configuration where the stress is relaxed on the graphene edge instead of on the Pt side, although with worse matching with the experimental images.

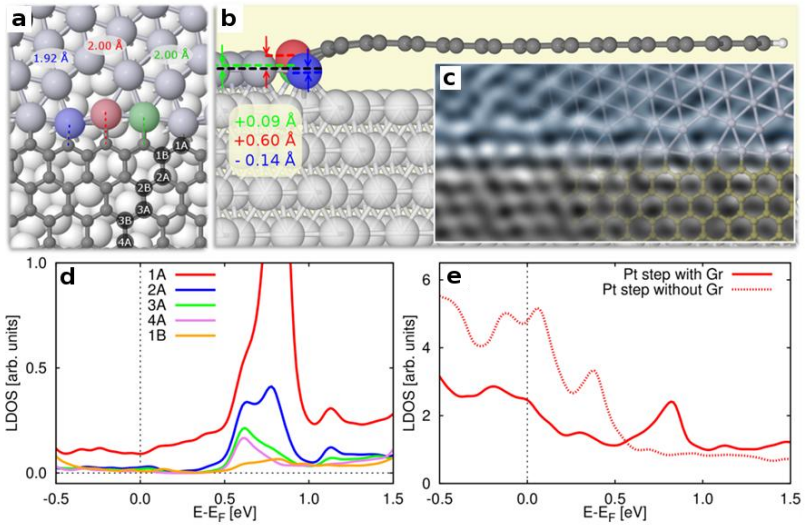

Figure 2 21: a *and* **b**. *Ball-and-stick model of the atomic configuration of graphene on the Pt(111) step edge calculated with DFT. Bond distance,* **a**, *and out of plane displacement,* **b**, *of the Pt edge atoms are indicated.* **c**. *Overlay of the relaxed structure with the STM image for edge ZZ1.* **d**. *Local density of states (LDOS) for the 1st (red), 2nd (blue), 3rd (green) and 4th (pink) rows of carbon atoms belonging to the same sublattice and for the 1st (orange) one of the other sublattice. An electronic state at +0.8 eV above E_F is clearly observed only in one sublattice and is mainly localized on the edge row.* **e**. *Local density of states (LDOS) for the Pt atoms at the edge of the step that are bonded to the C atoms (solid red) versus the same atoms in a step without a graphene flake attached (dashed red). The same localized electronic state shown in* c *can be observed in the Pt atoms of our Pt-C system but is absent in the bare Pt step*

The good match between the calculated atomic structure and the experimental STM images motivate us to characterize the electronic structure at the edges by calculating the local density of states (LDOS) associated to this nanostructure. **Figure 2 21 d** shows the calculated LDOS for the first carbon rows. A localized state ~0.8 eV above the Fermi level, with a FWHM of 0.2 eV, is found at the carbon atoms bonded to Pt. This state decays strongly in intensity when moving away from the edge. Furthermore, it is exclusively localized in one sublattice: the LDOS of the neighboring C atoms (orange curve in **Figure 2 21 d**), belonging to the other sublattice, does not show any trace of this state. The position of the peak with respect to the Fermi level and the decay length are similar to the ones

associated with a single atom vacancy on graphene on Pt [60]. Looking at the Pt side of the edge, we have found that the LDOS projected on the Pt row closer to the interface shows a peak at the same E_F+0.8 eV energy. This peak is not present in the LDOS of the pristine Pt step, indicating that the G-edge state spreads out inside the Pt (see **Figure 2 21 e**). Our calculations do not show any magnetism associated with the G-Pt edge. Free-standing graphene edges are characterized by the presence of a localized state at the Fermi level, which is responsible for the magnetic moment predicted for this system. In our case, both the charge transfer and the strong G-Pt interaction broaden this peak and shift it towards positive energies. As a consequence, the magnetic moments are quenched, similarly to the case of point defects on G/Pt [60].

This electronic state has to be reflected in the empty-states STM images, and this is indeed experimentally observed. In **Figure 2 22 a**, we show a topographic STM image where a modulation of the intensity parallel to the border-like edge is clearly visualized. The distance between the lines corresponding to the maxima is 2.4 Å (see the height profile in **Figure 2 22 b**), as corresponds to the fact that the edge state is exclusively confined in one of the two sublattices. Experiments show that after 4 lines the state fully disappears. This state, decaying away from the interface and localized in one of the sublattices, is also visible in the STM image of the ZZ2 edge in **Figure 2 21**.

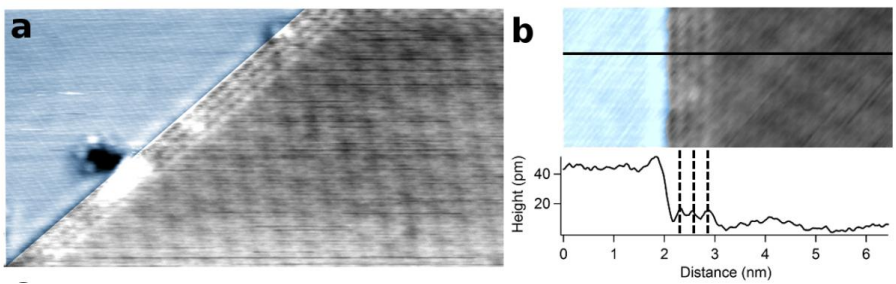

Figure 2 22: a. *13.4x6.9 nm^2 Topographic STM image of a border-like edge where an excess of charge is visualized parallel to the interface in the first three rows of graphene V_s = 51mV, I_t = 4nA.* **b**.*Detail of such 1D states and height profile*.

Interestingly this state is localized both in energy and real-space. It goes vanish as we move out of the interface. Therefore it can be considered as 1D electronic states associated to each of the graphene sublattices. These electronic states confined in specific sublattices of the graphene structure open new opportunities to future atomically precise graphene based electronics and valleytronics [61] [62]. For instance new multichannel nanowires could be built by contacting the opposite sides of a graphene flake with two different border-like edges. These atomically precise nano-leads will excite respectively each one of the two graphene sublattices, allowing two-ways atomically controlled transport via these independent electronic states (see **Figure 2 23** for a schematic proposition of a multichannel graphene nanowire).

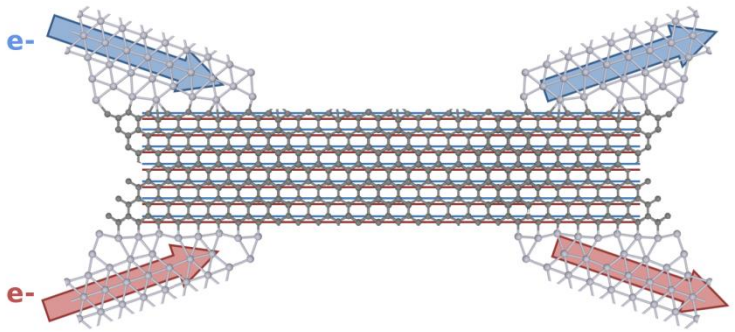

Figure 2 23: *Sketch showing a possible two-channel conductor using a G nanoribbon and atomically precise G-Pt contacts.*

2.7. Strain relief mechanisms: 0D,1D and 2D defects.

In the present section we change the topic from the metal-graphene heterostructures to the structures appearing inside the C layer upon forces unbalanced. It is the second law of thermodynamics that dictates the presence of a certain amount of disorder in crystalline materials. Moreover the production methods normally yield to some quantities of impurities and defects in the crystals [63]. Here we will try to shed some light on the defective atomic mechanisms we have found on the G/Pt(111) surface that leads to strain relief. The difference in the lattice constants between the graphene –or Moiré periodicities- and the substrate makes that the every Moiré superstructure accumulate a relatively high quantity of strain. The graphene layer will try to release these unbalanced forces through a variety of atomic scale defects – atomic vacancies, line defects…- or nanoscale defects – such as graphene-graphene grain boundaries, twisting of the moirés, carbide structures or nanobubbles.

This is not intended to be a rigorous study of all the possible defective structures that might appear on graphene, as this might be an enormous experimental task but rather a "*bestiary*" of all the structures observed during our STM experiments that yielded in strain release. We will divide the graphene defect into three different subgroups depending on its dimensionality therefore we will have, 0D defects, 1D defects, and 2D defects. However this must be take care with caution, as this is an artificial separation and there are structures that it can be assigned to more than one of these subgroups.

Figure 2 24 shows two independent 0D defects coexisting on the same sheet of graphene. This figure intends to show that the atomic scale defects can adopt more than one atomic configuration depending on how many C atoms are missing or where is/are this/these missing atom/s inside the Moiré unit cell.

The 0D defects can be divided in four groups according to previous work [63]:

1-Point defects: such as the so called Stone-Wales defect consisting in the restructuration of 4 hexagons inside the graphene layer into 2 pentagons and 2 heptagons without adding or removing any atom.

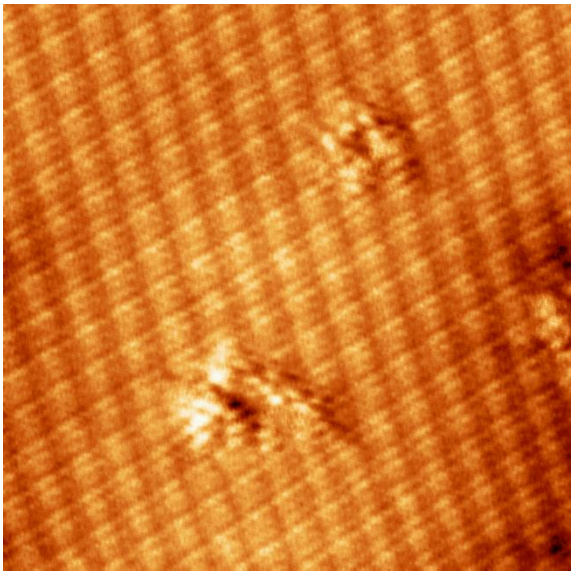

Figure 2 24: *STM images showing two 0D defects on graphene on Pt(111). These structures are present in small patches of graphene with high strains.12x12nm, 100mV, 1nA.*

2- Single vacancies: One missing atom induces the apparition of the characteristic Jahn-Teller distortion which leads to the formation of a five-membered and a nine-membered ring. This defect has been experimentally observed by means of STM on HOPG [46] (whose topmost layer posses mechanical properties similar to free-standing graphene). Analogous experiments on G/Pt(111) [60] -a supposed weakly interacting metallic substrate- induces a severe modification on the configuration of the defects through chemical bonding between the unsaturated C atoms and the substrate

3- Multiple vacancies: The simplest of them are the divacancies. These structures have been studied theoretically in detail [64] and experimentally studied by means of TEM [65]. Higher order vacancies involving more than two missing C atoms are likely to induce curvatures in the graphene layer and therefore forming domes and other sort of topological defects.

4- Foreign adatoms: The saturation of one π bond in graphene by an impinging atom has been observed on G/Ir(111) exposed to atomic H. In this particular case it seems that H adatoms tend to organize forming clusters on the positions of the Moiré superlattice [66]. Another possibility is

that the foreign adatom substitutes a C inside the graphene lattice. This possibility is very interesting in order to dope graphene [67] [68].

In **Figure 2 25** we show three different point defects found in our STM sessions of the G/Pt(111) system. We have to point out that obtaining atomic resolution of these defects at room temperature it is not an easy task and the results must be taken with caution. Moreover, the absence of theoretical calculations for comparing with the experimental results makes the present morphological analysis a preliminary approach to the understanding of these structures. However we believe that the quality of the image is good enough to try the interpretation of these structures through comparison with other studies. **Figure 2 25 a** shows a single atom defect, we believe this defect consists on an heteroatom –most likely a N atom coming from the residual gas in the chamber- incorporated into the graphene layer. We believe this is a N vacancy because in case it was a C vacancy a relaxation would be expected and because N electronic shall be expected in STM sessions darker as its electronic configuration is $2s^2 2p^3$. **Figure 2 25.b** shows a multiatomic vacancy which induced a reconstruction of a region of 1-2nm. Although a dome-like local configuration can be expected one must take with caution the fact that this region appears brighter –and thus higher- in the STM images as electronic effects are normally occurring in the defective regions of graphene. **Figure 2 25.c** shows a strain-induced lattice dislocation involving at least two unit cells of graphene. It is not clear to us whether or not this structure has C vacancies or graphene-metal bonds. Further studies including theoretical calculations would be desirable in order to fully determine the atomic configuration of this structure.

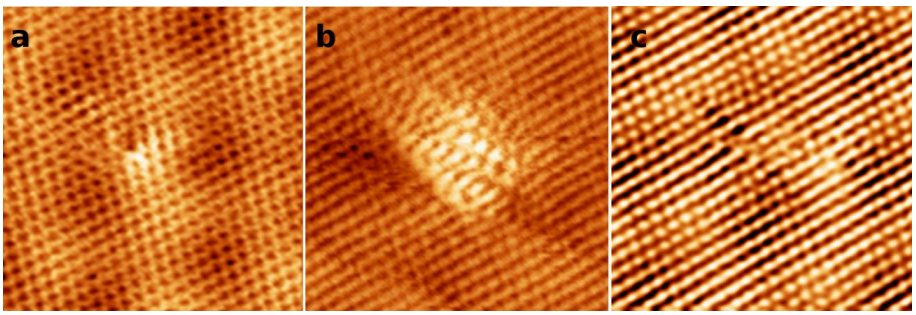

Figure 2 25: *Three 5x5nm^2 images showing 0D graphene defects on Pt(111).* **a**.*10 mV, 3.9nA .* **b**. *10 mV, 2nA.* **c**. *10 mV, 3.9nA*

In **Figure 2 26** we see a pseudo-periodic graphene grain boundary. The structure involves several, unresolved, vacancies and lattice deformations. Interestingly it seems that the grain boundary is periodic, adopting the periodicity of the larger of the two Moirés that separates.

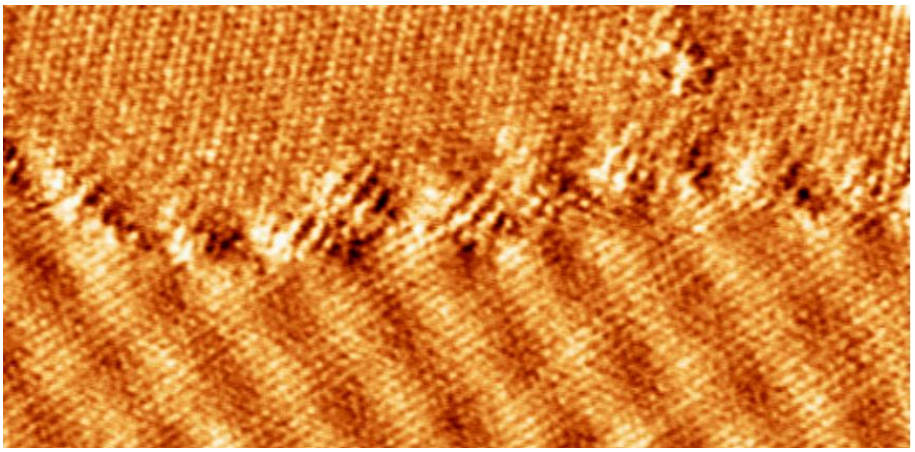

Figure 2 26: *Pseudo periodic G-G edge, the grain boundary follows the periodicity of the lower moiré. 18.4 x 9 nm^2, 2nA, 10mV.*

The possible 1D defects on metals can also be grouped in three categories:

1-Graphene edges: Either they are *step-like* or *border-like* the ending of a graphene sheet is considered as a defect. We already described how *step-like* edges are related to Moiré stability. On the other side the *border-like* edges try to minimize the total energy of the system by chemical functionalization. The two most likely functionalization mechanisms are through H passivation [69] or through covalent bonding with the metallic substrate [70] of the external C atoms.

2-Graphene grain boundaries: These are the junction structures appearing between two rotational domains of graphene. They can be crystalline, as the one found on the surface of Ni(111) [12], pseudoperiodic or amorphous [71]. These structures have attracted an important attention since theoretical works [47] predict exotic transport properties, such as the possibility of being used as valley filters [61] or metallic wires.

3- Graphene folds and wrinkles: Graphene might relax its strain through out of plane deformations. These deformations might be caused by surface defects, such as an atomic step [72], or by thermodynamic effects, such as a

chemical attacks [73] or local carbon accumulation due to the difference between the thermal expansion coefficients between the substrate and the overlayer [74] [75].

In **Figure 2 27** we see two 1D defects on the G/Pt(111) system. This figure tries to show that graphene adjust itself to the conformation which minimizes its energy which somehow might be counterintuitive. Thus in **Figure 2 27 a** we see two domains of graphene that lie in the same Pt(111) terrace but are separated by an amorphous grain boundary. The strain accumulated between the two domains induces the apparition of this defective structure. On the other hand, in **Figure 2 27b** we see that graphene can in some cases run across an atomic step without forming a grain boundary, the only defective structure appearing is an out-of-plane bending on the layer. The slope of the fall will depend on the strain accumulated inside the domain, but this train is not big enough to form any "more defective" (such as vacancies) configuration.

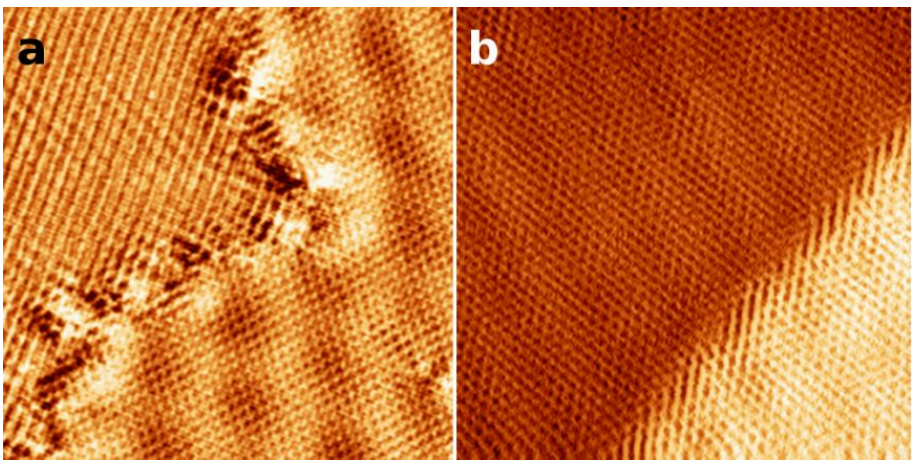

Figure 2 27: *Examples of 1D defective . G-G edge vs. graphene running through a Pt step.* **a** *. 10x10 nm^2 1.9nA, 10mV.* **b** *. 7.5x7.5 nm^2, 8nA, 2mV.*

At last, the remaining possible defective structures are 2-dimensional. These structures are not normally discussed in the literature as graphene itself is 2D. However we believe that we can talk of 2D defects correctly when talking about the two structures that are going to be discussed below.

1-Surface carbides: Surface metal carbides are well known as impurities in surface science. However it has been recently discovered that some 2D surface carbides become graphene under low temperature annealing [76]

following complex intermediate phases and forming interesting graphene-carbide interfaces. In the case of Pt the carbide structures consist normally on small 3D protrusions that grow separated forming *stone*-like clusters in the clean Pt(111) regions . However we can also find these *stones* embedded inside graphene regions, see **Figure 2 28 a**.

2-Graphene Nanobubbles: Graphene can relax its strain excess through formation of dome-like structures. These so-called nanobubbles have attracted an important theoretical attention since the discovery of gauge-related electronic effects in strained graphene [77]. Under this theoretical approach the electrons within three-fold strained graphene feel gauge field analogous to a magnetic field (and therefore called pseudo-magnetic fields [78]). Thus, zero-field landau levels are observed in strained graphene. In particular Pt(111) is a good substrate to form these nanobubbles and pseudomagnetic fields greater than 200T have been observed in G/Pt(111) nanobubbles [42].

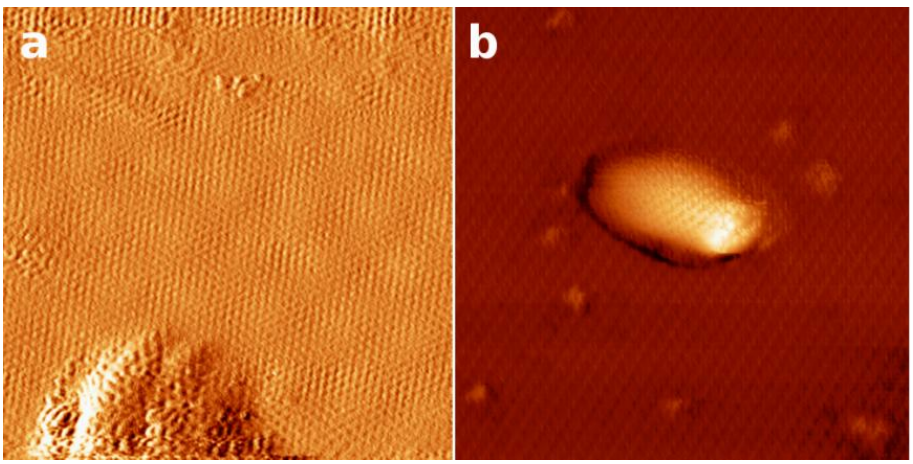

Figure 2 28: *Examples of 2D defective structures.* **a**. *Surface carbide,10x10 nm^2, 8nA, 2mV.* ***b****. Graphene nanobubble, 20x20 nm^2, 0.6nA, 310 mV.*

During our STM experiments we have observed both kinds of structures. We have found carbides forming 3D structures and embedded carbides. We also observed nanobubbles and, although our RT-STM is not the best tool to study the narrow resonances in the DOS, we have measured strange electronic effects around these nanobubbles. For instance in **Figure 2 28 b** we show a nanobubble inside a (√7x√7)R19^o domain; looking carefully we observe that its contour looks deeper than the bare (√7x√7)R19^o terrace.

We believe this is an electronic illusion-rather than a real topographic hole-caused by strain-induced electronic effects.

In conclusion in the present section we have explained a selection of defective structures that are normally related to strain relief mechanisms of G/Pt(111). We have also shown STM images of several of these mechanisms. We believe that the high accumulation of strain due to the apparition of a large number of rotational domains in G/Pt(111) makes this system an ideal testbed to study these graphene defective structures that might be important for future graphene based electronics.

2.8. Conclusions

The aim of this chapter is to characterize epitaxial graphene grown on weakly interacting metallic substrates. For this purpose we have efficiently grown graphene on Pt(111) by means of different carbon containing molecular precursors, from big aromatic molecules, such as C_{60} , to small hydrocarbons, such as propane C_3H_8.

Graphene grows forming rotational domains, i.e. domains with different angles between the G and Pt high symmetry axis. Every possible crystallographic angle result in the formation of a Moiré superstructure. These structures have been extensively studied by means of STM and an original theoretical model.

The model that we developed is based in the search of best matching pairs of surface crystal vectors for every angle between graphene and Pt(111). With these inputs our model predicts the apparition of 22 possible superstructures or Moirés for the case of G/Pt(111). Our model can be exported to other metallic crystalline substrates reproducing the Moirés reported in the literature for these substrates.

Thus, our model minimizes the strain occurring between graphene and substrate arising from the difference between the surface lattice parameters. It does predict the periodicity and apparent angle of every Moiré unit cell suggesting the possibility of metal-overlayer pinning regions within the Moiré unit cell. The most commonly observed Moirés are the ones holding less strain.

Among the possible structures the one holding a bigger strain is the $(\sqrt{3}X\sqrt{3})R30^{o}$, or αG/Pt(111) superstructure, which is observed experimentally occupying large portions of the total areas. We have developed a combined theoretical-experimental approach that determines that this structure consist in an ordered vacancy network in the topmost Pt(111) layer and a graphene layer covalently bound to it.

In order to understand the physical origin of our phenomenological theoretical model we have studied the atomic structure of the bonding regions between graphene and metal steps. These edges follow the crystallographic order of the Moiré and involve graphene normally finishing in a zig-zag configuration.

We have studied to the atomic scale the edge occurring between a Pt step and (√7X√7)R19^{o}, or βG/Pt(111) superstructure. Our combined theoretical and experimental approach shows that the step edge reconstructs exclusively in the Pt side and predicts the presence of an exotic 1D state in one of the two graphene sublattices. This prediction is confirmed experimentally as we observe a 1D structure in the unoccupied states of graphene when inspected with the STM.

Lastly we have presented the defective structures formed upon strain relaxation mechanisms. The formation of some of defective structures can be directly related to strain accumulation between the substrate and the overlayer. In conclusion we have performed a wide structural study of the G/Pt(111) systems and the possible crystalline and defective structures appearing within it.

Bibliography

1. Novoselov, K. S.; Geim, A. K.; Morozov, S. V.; Jiang, D.; Zhang, Y.; Dubonos, S. V.; Grigorieva, I. V.; Firsov, A. A., Electric Field Effect in Atomically Thin Carbon Films. *Science* **2004,** *306* (5696), 666-669.
2. Van Noorden, R., Chemistry: The trials of new carbon. *Nature* **2011,** *469* (7328), 14-6.
3. Bae, S.; Kim, H.; Lee, Y.; Xu, X.; Park, J. S.; Zheng, Y.; Balakrishnan, J.; Lei, T.; Kim, H. R.; Song, Y. I.; Kim, Y. J.; Kim, K. S.; Ozyilmaz, B.; Ahn, J. H.; Hong, B. H.; Iijima, S., Roll-to-roll production of 30-inch graphene films for transparent electrodes. *Nature nanotechnology* **2010,** *5* (8), 574-8.
4. Castro Neto, A. H.; Guinea, F.; Peres, N. M. R.; Novoselov, K. S.; Geim, A. K., The electronic properties of graphene. *Reviews of Modern Physics* **2009,** *81* (1), 109-162.
5. Wintterlin, J.; Bocquet, M. L., Graphene on metal surfaces. *Surface Science* **2009,** *603* (10–12), 1841-1852.
6. Batzill, M., The surface science of graphene: Metal interfaces, CVD synthesis, nanoribbons, chemical modifications, and defects. *Surface Science Reports* **2012,** *67* (3–4), 83-115.
7. Marchini, S.; Günther, S.; Wintterlin, J., Scanning tunneling microscopy of graphene on Ru(0001). *Physical Review B* **2007,** *76* (7), 075429.
8. Vázquez de Parga, A. L.; Calleja, F.; Borca, B.; Passeggi, M. C. G., Jr.; Hinarejos, J. J.; Guinea, F.; Miranda, R., Periodically Rippled Graphene: Growth and Spatially Resolved Electronic Structure. *Physical review letters* **2008,** *100* (5), 056807.
9. Eom, D.; Prezzi, D.; Rim, K. T.; Zhou, H.; Lefenfeld, M.; Xiao, S.; Nuckolls, C.; Hybertsen, M. S.; Heinz, T. F.; Flynn, G. W., Structure and Electronic Properties of Graphene Nanoislands on Co(0001). *Nano letters* **2009,** *9* (8), 2844-2848.
10. Varykhalov, A.; Rader, O., Graphene grown on Co(0001) films and islands: Electronic structure and its precise magnetization dependence. *Physical Review B* **2009,** *80* (3), 035437.
11. Miniussi, E.; Pozzo, M.; Baraldi, A.; Vesselli, E.; Zhan, R. R.; Comelli, G.; Menteş, T. O.; Niño, M. A.; Locatelli, A.; Lizzit, S.; Alfè, D., Thermal Stability of Corrugated Epitaxial Graphene Grown on Re(0001). *Physical review letters* **2011,** *106* (21), 216101.
12. Lahiri, J.; Lin, Y.; Bozkurt, P.; Oleynik, II; Batzill, M., An extended defect in graphene as a metallic wire. *Nature nanotechnology* **2010,** *5* (5), 326-9.
13. Gao, L.; Guest, J. R.; Guisinger, N. P., Epitaxial Graphene on Cu(111). *Nano letters* **2010,** *10* (9), 3512-3516.
14. Sicot, M.; Bouvron, S.; Zander, O.; Rudiger, U.; Dedkov, Y. S.; Fonin, M., Nucleation and growth of nickel nanoclusters on graphene Moir[e-acute] on Rh(111). *Applied Physics Letters* **2010,** *96* (9), 093115.
15. Murata, Y.; Starodub, E.; Kappes, B. B.; Ciobanu, C. V.; Bartelt, N. C.; McCarty, K. F.; Kodambaka, S., Orientation-dependent work function of graphene on Pd(111). *Applied Physics Letters* **2010,** *97* (14), 143114.

16. Coraux, J.; N'Diaye, A. T.; Engler, M.; Busse, C.; Wall, D.; Buckanie, N.; Heringdorf, F.-J. M. z.; Gastel, R. v.; Poelsema, B.; Michely, T., Growth of graphene on Ir(111). *New Journal of Physics* **2009,** *11* (2), 023006.
17. Merino, P.; Švec, M.; Pinardi, A. L.; Otero, G.; Martín-Gago, J. A., Strain-Driven Moiré Superstructures of Epitaxial Graphene on Transition Metal Surfaces. *ACS nano* **2011,** *5* (7), 5627-5634.
18. Martínez-Galera, A. J.; Brihuega, I. n.; Gómez-Rodríguez, J. M., Ethylene Irradiation: A New Route to Grow Graphene on Low Reactivity Metals. *Nano letters* **2011,** *11* (9), 3576-3580.
19. Nilsson, L.; Andersen, M.; Bjerre, J.; Balog, R.; Hammer, B.; Hornekær, L.; Stensgaard, I., Preservation of the Pt(100) surface reconstruction after growth of a continuous layer of graphene. *Surface Science* **2012,** *606* (3–4), 464-469.
20. Nilsson, L.; Andersen, M.; Balog, R.; Lægsgaard, E.; Hofmann, P.; Besenbacher, F.; Hammer, B.; Stensgaard, I.; Hornekær, L., Graphene Coatings: Probing the Limits of the One Atom Thick Protection Layer. *ACS nano* **2012,** *6* (11), 10258-10266.
21. Preobrajenski, A. B.; Ng, M. L.; Vinogradov, A. S.; Mårtensson, N., Controlling graphene corrugation on lattice-mismatched substrates. *Physical Review B* **2008,** *78* (7), 073401.
22. Loginova, E.; Nie, S.; Thürmer, K.; Bartelt, N. C.; McCarty, K. F., Defects of graphene on Ir(111): Rotational domains and ridges. *Physical Review B* **2009,** *80* (8), 085430.
23. Lang, B., A LEED study of the deposition of carbon on platinum crystal surfaces. *Surface Science* **1975,** *53* (1), 317-329.
24. Land, T. A.; Michely, T.; Behm, R. J.; Hemminger, J. C.; Comsa, G., STM investigation of single layer graphite structures produced on Pt(111) by hydrocarbon decomposition. *Surface Science* **1992,** *264* (3), 261-270.
25. Sutter, P.; Sadowski, J. T.; Sutter, E., Graphene on Pt(111): Growth and substrate interaction. *Physical Review B* **2009,** *80* (24), 245411.
26. Gao, M.; Pan, Y.; Huang, L.; Hu, H.; Zhang, L. Z.; Guo, H. M.; Du, S. X.; Gao, H.-J., Epitaxial growth and structural property of graphene on Pt(111). *Applied Physics Letters* **2011,** *98* (3), 033101.
27. Otero, G.; González, C.; Pinardi, A. L.; Merino, P.; Gardonio, S.; Lizzit, S.; Blanco-Rey, M.; Van de Ruit, K.; Flipse, C. F. J.; Méndez, J.; de Andrés, P. L.; Martín-Gago, J. A., Ordered Vacancy Network Induced by the Growth of Epitaxial Graphene on Pt(111). *Physical review letters* **2010,** *105* (21), 216102.
28. Otero, G.; Biddau, G.; Sanchez-Sanchez, C.; Caillard, R.; Lopez, M. F.; Rogero, C.; Palomares, F. J.; Cabello, N.; Basanta, M. A.; Ortega, J.; Mendez, J.; Echavarren, A. M.; Perez, R.; Gomez-Lor, B.; Martin-Gago, J. A., Fullerenes from aromatic precursors by surface-catalysed cyclodehydrogenation. *Nature* **2008,** *454* (7206), 865-8.
29. Horcas, I.; Fernandez, R.; Gomez-Rodriguez, J. M.; Colchero, J.; Gomez-Herrero, J.; Baro, A. M., WSXM: a software for scanning probe microscopy and a tool for nanotechnology. *The Review of scientific instruments* **2007,** *78* (1), 013705.

30. Martínez-Galera, A. J.; Gómez-Rodríguez, J. M., Surface Diffusion of Simple Organic Molecules on Graphene on Pt(111). *The Journal of Physical Chemistry C* **2011,** *115* (46), 23036-23042.
31. Sasaki, M.; Yamada, Y.; Ogiwara, Y.; Yagyu, S.; Yamamoto, S., Moiré contrast in the local tunneling barrier height images of monolayer graphite on Pt(111). *Physical Review B* **2000,** *61* (23), 15653-15656.
32. Moritz, W.; Wang, B.; Bocquet, M. L.; Brugger, T.; Greber, T.; Wintterlin, J.; Günther, S., Structure Determination of the Coincidence Phase of Graphene on Ru(0001). *Physical review letters* **2010,** *104* (13), 136102.
33. Jiang, D.-e.; Du, M.-H.; Dai, S., First principles study of the graphene/Ru(0001) interface. *The Journal of chemical physics* **2009,** *130* (7), 074705.
34. Felici, R.; Pedio, M.; Borgatti, F.; Iannotta, S.; Capozi, M.; Ciullo, G.; Stierle, A., X-ray-diffraction characterization of Pt(111) surface nanopatterning induced by C60 adsorption. *Nature materials* **2005,** *4* (9), 688-92.
35. Stengel, M.; Vita, A. D.; Baldereschi, A., Adatom-Vacancy Mechanisms for the C_{60}/Al(111)-(6×6) Reconstruction. *Physical review letters* **2003,** *91* (16), 166101.
36. Li, H. I.; Pussi, K.; Hanna, K. J.; Wang, L. L.; Johnson, D. D.; Cheng, H. P.; Shin, H.; Curtarolo, S.; Moritz, W.; Smerdon, J. A.; McGrath, R.; Diehl, R. D., Surface Geometry of C_{60} on Ag(111). *Physical review letters* **2009,** *103* (5), 056101.
37. Kobayashi, Y.; Fukui, K.-i.; Enoki, T.; Kusakabe, K.; Kaburagi, Y., Observation of zigzag and armchair edges of graphite using scanning tunneling microscopy and spectroscopy. *Physical Review B* **2005,** *71* (19), 193406.
38. Dong, G. C.; Baarle, D. W. v.; Rost, M. J.; Frenken, J. W. M., Graphene formation on metal surfaces investigated by in-situ scanning tunneling microscopy. *New Journal of Physics* **2012,** *14* (5), 053033.
39. Gunther, S.; Danhardt, S.; Ehrensperger, M.; Zeller, P.; Schmitt, S.; Wintterlin, J., High-temperature scanning tunneling microscopy study of the ordering transition of an amorphous carbon layer into graphene on ruthenium(0001). *ACS nano* **2013,** *7* (1), 154-64.
40. Gao, J.; Yip, J.; Zhao, J.; Yakobson, B. I.; Ding, F., Graphene Nucleation on Transition Metal Surface: Structure Transformation and Role of the Metal Step Edge. *Journal of the American Chemical Society* **2011,** *133* (13), 5009-5015.
41. Phark, S.-h.; Borme, J.; Vanegas, A. L.; Corbetta, M.; Sander, D.; Kirschner, J., Atomic structure and spectroscopy of graphene edges on Ir(111). *Physical Review B* **2012,** *86* (4), 045442.
42. Levy, N.; Burke, S. A.; Meaker, K. L.; Panlasigui, M.; Zettl, A.; Guinea, F.; Neto, A. H. C.; Crommie, M. F., Strain-Induced Pseudo–Magnetic Fields Greater Than 300 Tesla in Graphene Nanobubbles. *Science* **2010,** *329* (5991), 544-547.
43. Nakada, K.; Fujita, M.; Dresselhaus, G.; Dresselhaus, M. S., Edge state in graphene ribbons: Nanometer size effect and edge shape dependence. *Physical review. B, Condensed matter* **1996,** *54* (24), 17954-17961.
44. Yazyev, O. V., Emergence of magnetism in graphene materials and nanostructures. *Reports on Progress in Physics* **2010,** *73* (5), 056501.

45. Tao, C.; Jiao, L.; Yazyev, O. V.; Chen, Y.-C.; Feng, J.; Zhang, X.; Capaz, R. B.; Tour, J. M.; Zettl, A.; Louie, S. G.; Dai, H.; Crommie, M. F., Spatially resolving edge states of chiral graphene nanoribbons. *Nat Phys* **2011,** *7* (8), 616-620.
46. Ugeda, M. M.; Brihuega, I.; Guinea, F.; Gómez-Rodríguez, J. M., Missing Atom as a Source of Carbon Magnetism. *Physical review letters* **2010,** *104* (9), 096804.
47. Yazyev, O. V.; Louie, S. G., Electronic transport in polycrystalline graphene. *Nature materials* **2010,** *9* (10), 806-9.
48. Ruffieux, P.; Cai, J.; Plumb, N. C.; Patthey, L.; Prezzi, D.; Ferretti, A.; Molinari, E.; Feng, X.; Mullen, K.; Pignedoli, C. A.; Fasel, R., Electronic structure of atomically precise graphene nanoribbons. *ACS nano* **2012,** *6* (8), 6930-5.
49. Cai, J.; Ruffieux, P.; Jaafar, R.; Bieri, M.; Braun, T.; Blankenburg, S.; Muoth, M.; Seitsonen, A. P.; Saleh, M.; Feng, X.; Mullen, K.; Fasel, R., Atomically precise bottom-up fabrication of graphene nanoribbons. *Nature* **2010,** *466* (7305), 470-3.
50. Acik, M.; Chabal, Y. J., Nature of Graphene Edges: A Review. *Japanese Journal of Applied Physics 50* (7), 070101.
51. Yazyev, O. V., A Guide to the Design of Electronic Properties of Graphene Nanoribbons. *Accounts of chemical research* **2013**.
52. Girit, C. O.; Meyer, J. C.; Erni, R.; Rossell, M. D.; Kisielowski, C.; Yang, L.; Park, C. H.; Crommie, M. F.; Cohen, M. L.; Louie, S. G.; Zettl, A., Graphene at the edge: stability and dynamics. *Science* **2009,** *323* (5922), 1705-8.
53. Suenaga, K.; Koshino, M., Atom-by-atom spectroscopy at graphene edge. *Nature* **2010,** *468* (7327), 1088-90.
54. Ritter, K. A.; Lyding, J. W., The influence of edge structure on the electronic properties of graphene quantum dots and nanoribbons. *Nature materials* **2009,** *8* (3), 235-42.
55. Tian, J.; Cao, H.; Wu, W.; Yu, Q.; Chen, Y. P., Direct imaging of graphene edges: atomic structure and electronic scattering. *Nano letters* **2011,** *11* (9), 3663-8.
56. Ridene, M.; Girard, J. C.; Travers, L.; David, C.; Ouerghi, A., STM/STS investigation of edge structure in epitaxial graphene. *Surface Science* **2012,** *606* (15–16), 1289-1292.
57. Zhang, Y.; Li, Z.; Kim, P.; Zhang, L.; Zhou, C., Anisotropic Hydrogen Etching of Chemical Vapor Deposited Graphene. *ACS nano* **2011,** *6* (1), 126-132.
58. Gao, J.; Zhao, J.; Ding, F., Transition metal surface passivation induced graphene edge reconstruction. *Journal of the American Chemical Society* **2012,** *134* (14), 6204-9.
59. Stokbro, K.; Engelund, M.; Blom, A., Atomic-scale model for the contact resistance of the nickel-graphene interface. *Physical Review B* **2012,** *85* (16), 165442.
60. Ugeda, M. M.; Fernández-Torre, D.; Brihuega, I.; Pou, P.; Martínez-Galera, A. J.; Pérez, R.; Gómez-Rodríguez, J. M., Point Defects on Graphene on Metals. *Physical review letters* **2011,** *107* (11), 116803.
61. Gunlycke, D.; White, C. T., Graphene Valley Filter Using a Line Defect. *Physical review letters* **2011,** *106* (13), 136806.

62. Rycerz, A.; Tworzydlo, J.; Beenakker, C. W. J., Valley filter and valley valve in graphene. *Nat Phys* **2007,** *3* (3), 172-175.
63. Banhart, F.; Kotakoski, J.; Krasheninnikov, A. V., Structural Defects in Graphene. *ACS nano* **2010,** *5* (1), 26-41.
64. Kim, Y.; Ihm, J.; Yoon, E.; Lee, G.-D., Dynamics and stability of divacancy defects in graphene. *Physical Review B* **2011,** *84* (7), 075445.
65. Kotakoski, J.; Krasheninnikov, A. V.; Kaiser, U.; Meyer, J. C., From Point Defects in Graphene to Two-Dimensional Amorphous Carbon. *Physical review letters* **2011,** *106* (10), 105505.
66. Balog, R.; Jorgensen, B.; Nilsson, L.; Andersen, M.; Rienks, E.; Bianchi, M.; Fanetti, M.; Laegsgaard, E.; Baraldi, A.; Lizzit, S.; Sljivancanin, Z.; Besenbacher, F.; Hammer, B.; Pedersen, T. G.; Hofmann, P.; Hornekaer, L., Bandgap opening in graphene induced by patterned hydrogen adsorption. *Nature materials* **2010,** *9* (4), 315-9.
67. Zhao, L.; He, R.; Rim, K. T.; Schiros, T.; Kim, K. S.; Zhou, H.; Gutiérrez, C.; Chockalingam, S.; Arguello, C. J.; Pálová, L., Visualizing individual nitrogen dopants in monolayer graphene. *Science* **2011,** *333* (6045), 999-1003.
68. Panchakarla, L.; Subrahmanyam, K.; Saha, S.; Govindaraj, A.; Krishnamurthy, H.; Waghmare, U.; Rao, C., Synthesis, structure, and properties of boron-and nitrogen-doped graphene. *Advanced Materials* **2009,** *21* (46), 4726-4730.
69. Park, C.; Yang, H.; Mayne, A. J.; Dujardin, G.; Seo, S.; Kuk, Y.; Ihm, J.; Kim, G., Formation of unconventional standing waves at graphene edges by valley mixing and pseudospin rotation. *Proceedings of the National Academy of Sciences* **2011,** *108* (46), 18622-18625.
70. Li, Y.; Subramaniam, D.; Atodiresei, N.; Lazić, P.; Caciuc, V.; Pauly, C.; Georgi, A.; Busse, C.; Liebmann, M.; Blügel, S.; Pratzer, M.; Morgenstern, M.; Mazzarello, R., Absence of Edge States in Covalently Bonded Zigzag Edges of Graphene on Ir(111). *Advanced Materials* **2013,** *25* (14), 1967-1972.
71. László, P. B.; Philippe, L., Grain boundaries in graphene grown by chemical vapor deposition. *New Journal of Physics* **2013,** *15* (3), 035024.
72. Coraux, J.; N`Diaye, A. T.; Busse, C.; Michely, T., Structural Coherency of Graphene on Ir(111). *Nano letters* **2008,** *8* (2), 565-570.
73. Feng, X.; Maier, S.; Salmeron, M., Water Splits Epitaxial Graphene and Intercalates. *Journal of the American Chemical Society* **2012,** *134* (12), 5662-5668.
74. Zhu, W.; Low, T.; Perebeinos, V.; Bol, A. A.; Zhu, Y.; Yan, H.; Tersoff, J.; Avouris, P., Structure and electronic transport in graphene wrinkles. *Nano letters* **2012,** *12* (7), 3431-3436.
75. Li, X.; Cai, W.; An, J.; Kim, S.; Nah, J.; Yang, D.; Piner, R.; Velamakanni, A.; Jung, I.; Tutuc, E., Large-area synthesis of high-quality and uniform graphene films on copper foils. *Science* **2009,** *324* (5932), 1312-1314.
76. Lahiri, J.; Miller, T.; Adamska, L.; Oleynik, II; Batzill, M., Graphene growth on Ni(111) by transformation of a surface carbide. *Nano letters* **2011,** *11* (2), 518-22.

77. Guinea, F.; Katsnelson, M.; Geim, A., Energy gaps and a zero-field quantum Hall effect in graphene by strain engineering. *Nature Physics* **2009,** *6* (1), 30-33.
78. Low, T.; Guinea, F., Strain-induced pseudomagnetic field for novel graphene electronics. *Nano letters* **2010,** *10* (9), 3551-4.

Chapter 3.
Epitaxial graphene on SiC(0001)

In order to use the already existing semiconductor based industry for microfabrication of new integrated circuits based on 2D materials, a non-metallic substrate results necessary to decouple the intrinsic semimetallic transport properties of the ad-layer from those –normally dominating- of the substrate. In a moment where Si-based technology is reaching its fundamental limits, the high mobility of electrons in graphene, even under high electric fields [1], together with the fact that its electronic properties are very robust, even at ambient conditions [2] , makes graphene a possible solution to keep increasing the speed and quantity of transistors per chip. For instance ballistic transport at room temperature in the submicron legth-scale can be achieved on this material and therefore a graphene-based ballistic transistor can be, in principle, fabricated [3].

Graphene microelectronics has its intrinsic drawbacks. For instance the absence of a bandgap complicates the design of such transistors. Moreover the production methodologies implemented up to now have several limitations. HOPG mechanical exfoliation [4] is well suitable for producing small –up to several μm- high purity flakes. Graphene oxide reduction produces high quantities of -relatively high- chemically modified graphene sheets [5]. Graphene on polycrystalline copper is nowadays the most promising production method of freestanding graphene [6] but the resulting product is more suitable for being used as transparent conducting electrodes in touch-screen devices than in microelectronics. Graphene grown on single crystal metals produces high quality large area sheets but the price of the substrate makes this method only suitable for academic studies. In order to be scalable for a future graphene-based electronics, cheap and stable substrates are desirable. Among the current main production methods there is only one that fulfills the requirements –large production scale, low price, high domain area, high crystalline quality, and ease to handle- necessary for a potential graphene-based microelectronics: epitaxial graphene on single crystal silicon carbide (SiC).

It was in 2004, short after graphene was isolated for first time in Manchester, when C. Berger *et al*. noticed that the graphitic layers that had been previously observed epitaxially growing on SiC(0001) (see for example a 1997 review in [7]) behave as graphene [8]. In its pioneering work C. Berger *et al*. showed that the electrons in G/SiC(0001) behave as in a 2D electron gas with high electron mobility over large scales, and that the system could be successfully patterned by conventional lithography in order to create devices. After this finding, further developments have been achieved and transistors up to 100GHz have been patterned onto wafer-scale epitaxial

graphene [9] [10] and integrated circuits have been successfully developed onto SiC wafers [11].

However, in the present section we will not focus on the possible devices and applications of this system but rather on the structural modification of the G/SiC(0001) upon molecular deposition. For this purpose we have characterized all the possible surface reconstructions appearing on this material under UHV conditions and we have chosen two different characteristic molecular species to deposit onto it: one belonging to the group of very weakly interacting adsorbates – C_{60}- and the other belonging to the group of highly reactive and highly interacting adsorbates – atomic hydrogen (H)-. We have performed a combined theoretical-experimental atomistic characterization of the C_{60}/G/SiC(0001) system and H/G/SiC(0001) and compared the main interactions between them as well as with other similar systems.

SiC is a compound present in the nature in the form of the mineral form of moissanite. This mineral is extremely rare on earth but extraordinary abundant in space where it is synthesized in the vicinities of carbon-rich asymptotic giant branch stars. It can crystallize in a zinkblende structure-cubic SiC, historically called β-SiC- or a wurtzite structure –hexagonal symmetry, also known as α-SiC-. There are more than 170 identified polytypes of SiC depending on the stacking of the layers [12]. The most common ones according to the current production techniques are the 3C-SiC, 2H-SiC, 4H-SiC and 6H-SiC. In **Figure 3 1** we show the crystallographic unit cell of two different polytypes. One can see that the 6H-SiC unit cell includes 6 Si-C layers. We have used both 3C and 6H polytypes during the studies of this thesis, however only results from 6H-SiC(0001) samples are presented.

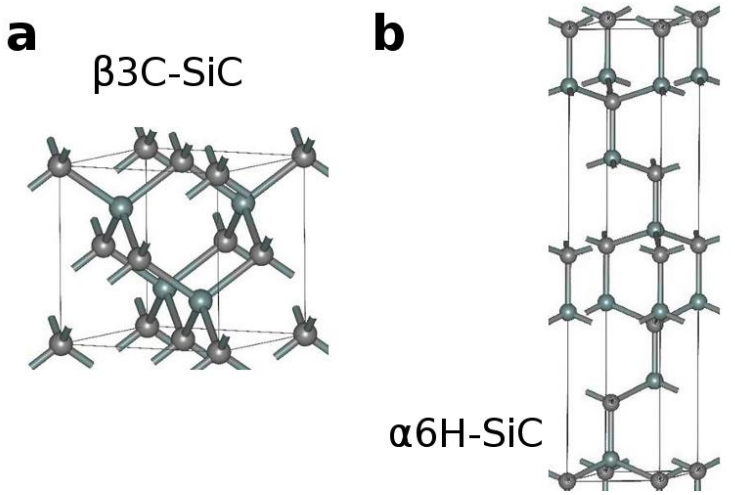

Figure 3 1: *Crystal unit cells of the two most common polytypes of SiC.* **a***. 3C-SiC.* **b***. 6H-SiC.*

There are some good reviews about SiC surfaces. Every one of these works is focused on different aspects of this material. The information therein has been very helpful during the realization of this thesis and it is referred all along this chapter. The reader is therefore kindly invited to read the following references for further understanding of SiC [12] [7] [13] [14] [15] [16] [17] [18] [19] [20].

3.1. 6H-SiC(0001): high temperature surface reconstructions

The as-received samples are not suitable for performing atomic scale studies because they are covered by a native SiO_2 layer on the polished side that prevents the surface for experimentation. A process for removing this protective layer is necessary. The cleaning protocol used during this thesis is as follows: Prior to all, the SiC platelets need to be cut apart from the wafer with the help of a diamond tip and mounted onto the specific sample holders. Then the sample needs to be slowly annealed, ramping up the temperature while keeping the pressure in the 10^{-10} mbar range. This induces a sample, and annealing-stage, degasification that results necessary in order to obtain low pressures during the high temperature flashes that are forthcoming. After this degassing procedure we turn on the –already degassed- Si evaporation. The most important step of the process consists in evaporating while SiC annealing; this is shown in **Figure 1 21** where a picture of the interior of the UHV chamber during the process is presented. The sample is mounted in a refractory metal sample holder, in this case Ta, and is annealed at 1100K while a Si evaporator, placed 15 cm in front of the sample, is kept at 1500K. This Si evaporation temperature at the abovementioned distance yields an approximate evaporating rate of 1ML/s. The flux, however, has not been precisely calibrated (for example with the help of a quartz balance) as the exact value is not important. The Si deposition is only necessary in order to maintain the Si stoichiometry of the SIC sample during the SiO_2 removal. Several combined cycles of Si evaporation and annealing are normally needed in order to obtain large terraces of high-quality reconstruction. Every Si evaporation while SiC annealing cycle is typically 10-15 min long. Normally one need to perform 3 to 6 cycles in order to clean the surface, although if the base pressure is high (>$5x10^{-9}$mbar) one may need more of them.

The usual way to check the cleanliness of the surface is with the help of LEED instrumentation. The sample, when introduced in the UHV chamber exhibits a faint 1x1 LEED pattern. After several cycles of SI evaporation while annealing a sharp 3x3 pattern arises. Interestingly, this pattern appears much before the sample is well suited for performing scanning probe microscopy studies, and only when the pattern is very sharp and the background very faint the terraces are well developed. Once the sample has this well developed 3x3 pattern, further annealing increasing the temperature yield to the different reconstructions-($\sqrt{3}x\sqrt{3}$)R30º, ($6\sqrt{3}x6\sqrt{3}$)R30º, and graphene- without the need of any Si surplus or any other UHV additional process.

For having a complete view of the G/SiC system we must briefly introduce another main preparation method. Several groups instead of UHV treatment use *ex-situ* Argon (Ar) assisted graphitization of the SiC(0001) samples. The method was described by K.V. Emtsev *et al.* [21] and consist in H-etching followed by an 1950K annealing of the sample into 900 mb of Ar. The samples prepared following this method normally present very large graphene terraces and morphologically superior graphene. The explanation to this improvement in the quality is explained because higher temperatures are achievable under Ar atmosphere prior to Si depletion. No Si depletion is observed in near-atmospheric pressures of Ar until 1800K as it exists a non negligible probability that an outgoing SI atom gets reflected back to the surface by collision with Ar atoms. We must underline that we have not used these ex-situ samples in any of our experiments, but the more conventional- and still high quality resulting- UHV method was used in our experimental sessions.

In **Figure 3 2** we see the mesoscopic characterization of the 6H-SiC(0001) sample. The as-received sample was investigated with SEM and AFM. It does not result surprising to find that the polished side appears smoother than the unpolished side of the wafer. In the **Figure 3 2 a** the only visible item are small spots, probably dust grains, in the limit of the resolution of the microscope, the scratches of the polishing process are not resolved with the SEM. In the **Figure 3 2 b** we see that the unpolished side appears rough even under a smaller amplification, indicating that the cut of the wafers is a relatively harsh process that leaves the surface in a very disordered configuration. In the AFM images of the polished side we see, that the as-received sample is full of scratches in all directions. These trenches arise as the grains of the polishing powder attack the surface, mainly covered of SiO_2 and probably amorphous carbides. We show on **Figure 3 2 d** an AFM image of the same surface (same scanning area size) after UHV graphitization and the comparison results surprising: in the treated sample the atomic steps of the terraces are clearly resolved (while on the as-received only the scratches are visible) forming intricate shapes.

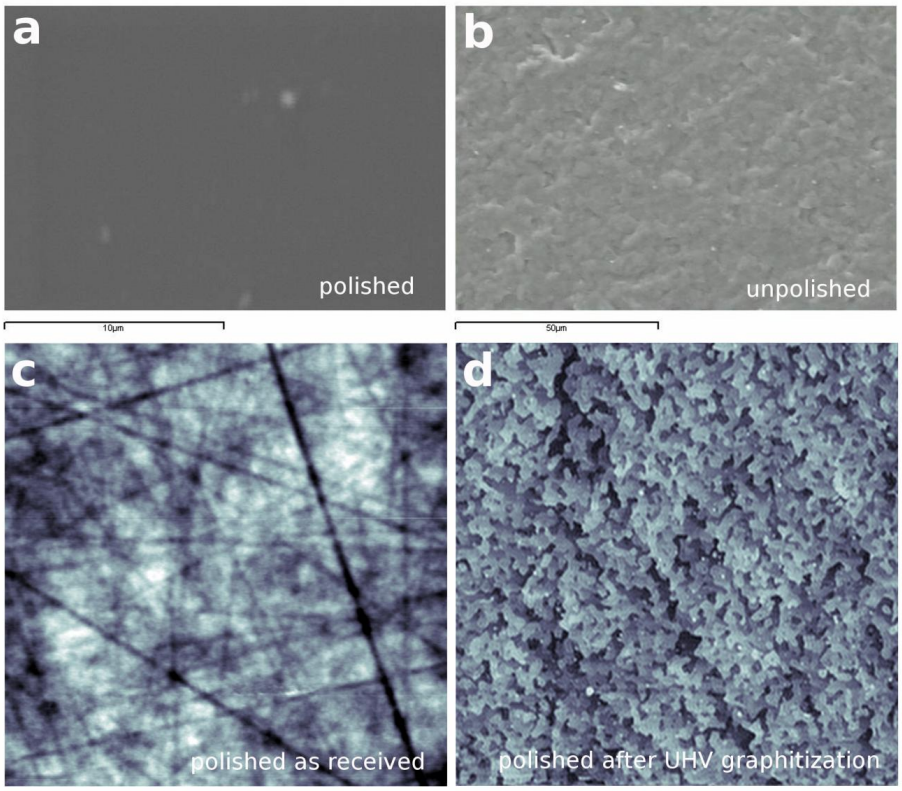

Figure 3 2: a. *SEM image of the polished side of an as-received 6H-SiC(0001) wafer, the scale bar is underneath the image.* **b**. *SEM image of the unpolished side of an as-received 6H-SiC(0001) wafer, the scale bar is underneath the image*. **c**. *AFM image of the polished side of an as-received 6H-SiC(0001) 10x10 µm^2*. **d**. *AFM image of the 6H-SiC(0001) sample (polished side) after UHV treatment. The atomic terraces are resolved, 10x10 µm^2.*

In the following sub-section we will introduce, when possible, the LEED, LEEM, XPS and STM characterization of the different C-rich SiC(0001) reconstructions induced upon temperature. We have characterized these structures as a reference for subsequent molecular depositions or treatments. The relatively Si-rich reconstructions,(3x3) and (√3x√3)R30^o, are described in similar detail in the Appendix.

a. (6√3x6√3)R30°/SiC(0001) or buffer layer.

If the temperature of the annealing is higher than 1450K, Si depletion from the crystal surface increases. Eventually the surface changes its reconstruction and a (6√3×6√3)R30° LEED pattern develops. This change corresponds to the appearance of quasi-periodic (6×6) reconstruction in some regions of the surface. This surface structure was reported in 1975 through LEED observations [22] and first STM images were performed in 1996 [23] [24] by two independent groups. They reported a mixture of three reconstructions, the (√3x√3) and two psuedoperiodic reconstructions with approximate periodicities of 6x6 and 5x5 respectively, from Fourier analysis of experimental STM images.

(6√3x6√3)R30°, quasi-(6x6), buffer layer or zero layer graphene (ZLG) are different names for the same structure. The exact atomic structure of this surface reconstruction is hard to determine because its pseudo-periodic behavior; from a theoretical point of view it is hard to handle because the large amount of atoms involved in the surface unit cell, and some groups use artificially smaller unit cells to perform their simulation of the (6√3×6√3)R30° structure [25] [26]. Nevertheless, experimental and theoretical groups have proposed some atomic configurations involving the presence of C in sp^2 (graphene) configuration covalently bound to the uppermost SiC layer. Some of these proposed atomic models have been suggested by Chen *et al.* [27], Rutter *et al*. [28] and Riedl et al. [29]. From an experimental point of view, the commensurability of graphene with the SiC substrate and the resulting periodicity of the atomic termination of the surface posses a doubly interesting behavior. When inspected with local techniques, such as STM or nc-AFM it presents a overall (6×6) quasi-periodicity (although the dangling bonds of the buffer layer and the graphene corrugation are normally also resolved), while when studied with diffraction tools a (6√3×6√3)R30° pattern emerges. These ambiguous observations have been put together by the atomic model of Kim *et al*. [30]. They proposed that this layer consist of a mesh of C atoms arranged in a honeycomb lattice, analogously to graphene, but contrary to it, some of the resulting semi-filled π-orbitals being covalently bound to the atoms of the next layer buried underneath and preventing the formation of a developed π band. A similar model proposed by Varchon et al. [31] show that the covalently bonded graphene sheet in the buffer layer is highly corrugated. However one must notice that the simulated STM images for these models are in modest agreement with the STM images obtained experimentally, and dangling bonds do not appear in the simulated images. More recently,

another theoretical-experimental work proposed the presence of hexagon-pentagon- heptagon defects breaking the honeycomb symmetry of this structure and thus opening a gap, in good agreement with the ARPES results [32]. To the best of our knowledge there is not a clear consensus on the atomic structure of this reconstruction although there exist several works "*solving the long-standing problem of the interfacial structure of epitaxial graphene on SiC(0001)*". Just as an example we would like to bring the attention to the works performed during the present year about this topic, as they present clear contradictions with the previous literature [33] [34] .

In **Figure 3 3** we show three STM images of different scales of this reconstruction. In the large scale image we see features spaced following the 6x6 pseudoperiodicity; it has an approximate unit cell length of 19 Å and grows in terraces of 10-100 nm. When inspected with atomic resolution (see **Figure 3 3 c**) we find structures known as dangling bonds. This atomic protrusion arises from an extended atomic orbital of the former (√3x√3)R30º periodicity. The height variation of these dangling bonds is what produces the superperiodicity of 19 Å. The surface looks very defective at both scales –atomic and superperiodicity- and there are missing atomic dangling bonds as well as missing trimmers all over the surface when inspected with STM. The atomic structure of this reconstruction is formed by three nonequivalent sublattices of (√3x√3)R30º coexisting on the surface. Every of these sublattices is shifted with respect to the other two, and forms a complex network of nonequivalent positions. The trimmers arise when three atoms, one atom belonging to each sublattice, appear together, in the vertex of the trimmers.

On (6√3x6√3)R30º, no graphene atomic resolution can be achieved despite the honeycomb carbon lattice covering the structure. When scanning with a bias voltage near the Fermi level the measurement gets unstable and crashing the tip is a very likely scenario. Out of this voltage range, the main features are the dangling bonds and the quasi-(6x6). On the other hand obtaining graphene corrugation on single layer graphene is normally obtained at bias close to the Fermi level. And out of this voltage range the main attributes are very similar to those of the underlying 6√3x6√3)R30º. STM images of SLG at high bias are very similar to STM images of the buffer layer itself. Graphene and buffer layer both have the quasi-6x6 superperiodicity and distinguish them can be difficult as tip artifacts might induce confusion between both reconstructions. The strong bias dependence of the G/SiC surface makes the identification of the surface structures not trivial in some cases.

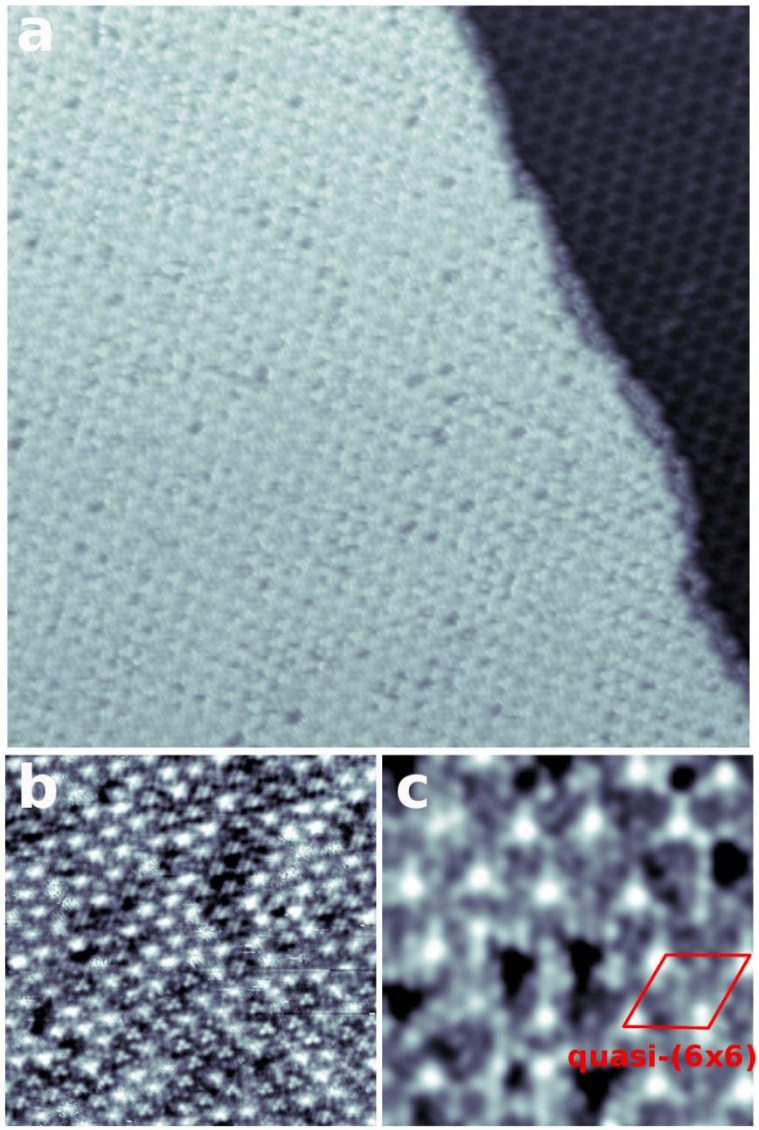

Figure 3 3: *STM images of the (6√3x6√3)R30º reconstruction.* **a**. *50x50 nm^2 , 0.0nA, -1200mV.* **b**. *25x25 nm^2, -1 nA, -2400mV.* **c**.*10x10 nm^2, -1nA, 1000mV.*

The XPS spectra of this structure are presented in **Figure 3 4**. In the overview we can check that the C1s peak has bigger intensity than the Si-related peaks, thus indicating ,in principle, that the surface has become richer in carbon due to the Si depletion. The C1s/Si2p ratio is now 1.15 and

the peaks still seem to be single component centered at 283.5 eV (these experiments were performed with an X-Ray Al-anode , so the resolution is not as good as the synchrotron spectra and the Si doublet is not resolved). However a strong asymmetry in the C1s peak reveal the existence of a developing second component at higher energies; let us remember that the C1s component related to sp^2 bonding hybridization appears at 284.8 eV [35]. Therefore this second component most likely comes from graphitic carbon that is starting to form on the surface of the reconstruction. On the other hand the maximum of the Si2p peak is slightly shifted towards higher energies up to 101.4 eV and a single component is resolved. This spectrum corresponds to a surface with a very low degree of graphitization as can be inferred from the C1s peak.

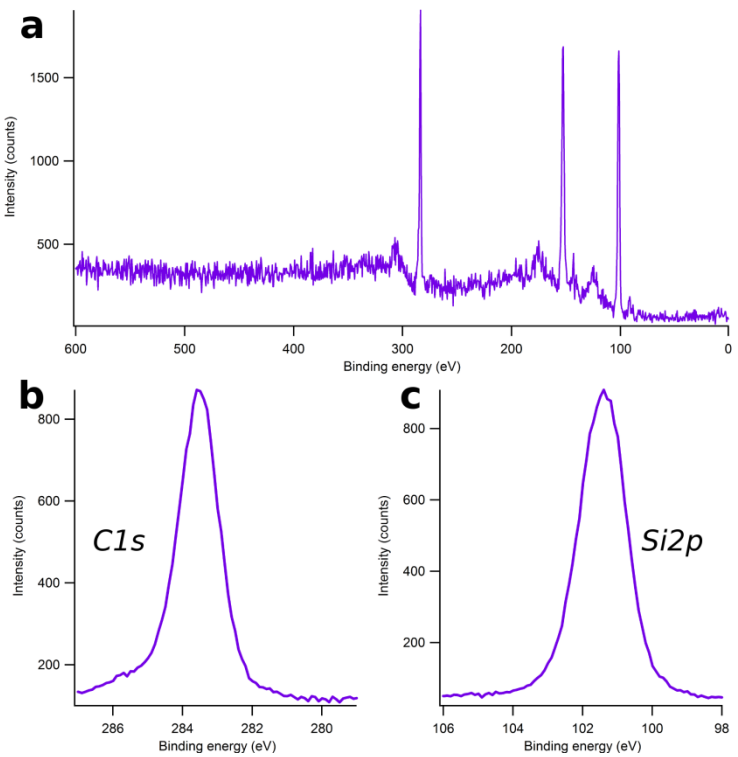

Figure 3 4: *XPS spectra of (6√3x6√3)R30° surface using an Al Kα anode (1486.6 eV) as X-ray source and hence the rather low quality .* **a***. Overview for comparing the relative intensity of the C1s and Si2p and Si2s peaks.* **b***. detail of the C1s peak, only one component appears at an energy corresponding to carbide, although a small component at higher energies starts to be noticeable.* **c***. Si2p peak.*

The LEED pattern of this reconstruction is very instructive. The experimental pattern is shown in **Figure 3 5** together with an explanation of the observed dots. The complexity of the spot arrangement has fostered several interpretations. However, most of them involve the presence of more than one atomic reconstruction on the sample´s surface. The sketch remarks the origin of each of the observed dots, highlighting the coexistence of SiC (1x1), faint graphene dots, (√3x√3)R30º, (6√3x6√3)R30º, (6x6) and quasi-(5x5) on the same surface preparation. It is interesting to comment that most of the nominal (6√3x6√3)R30º spots are not normally visible, but only a small amount of them are clearly resolved. An interesting LEED I(V) analysis of this pattern is presented in [36].

Another point that shall be commented on the LEED pattern is the evolution of the inner points of the characteristic diamonds appearing around the (√3x√3)R30º spots. The √3 spots are dominating in intensity until the quasi-5x5 spot appears. They coexist during a small range of temperatures, and thus C/Si ratio (an experimental pattern of this coexistence can be seen in **Figure 3 6 b**). If we continue annealing only the quasi-(5x5) remains (**Figure 3 6 c**) and eventually where several layers of graphene are developed none of them can be observed.

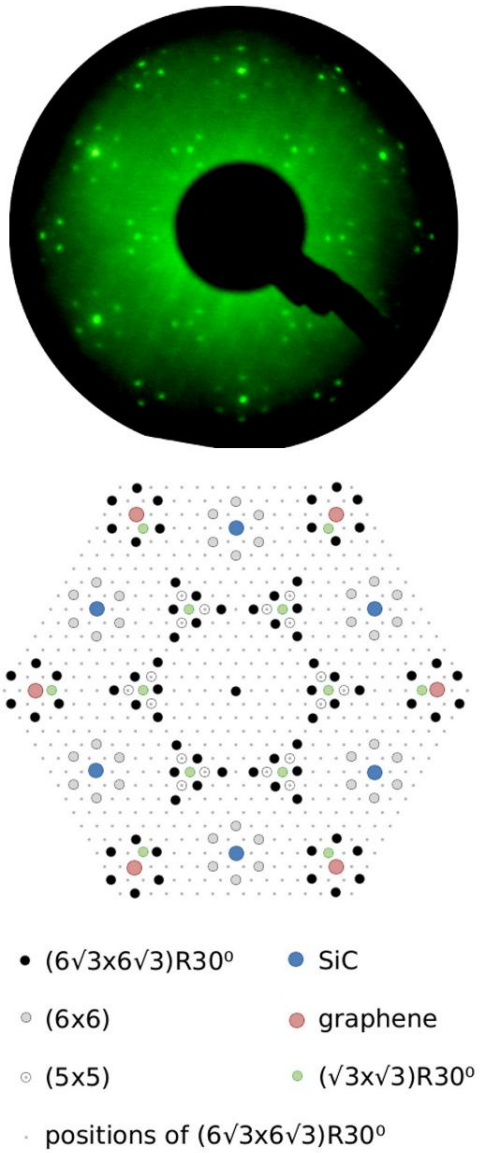

Figure 3 5: *LEED pattern of the (6√3x6√3)R30° structure at 140eV. The theoretical explanation of the pattern is adapted from ref.*[20]

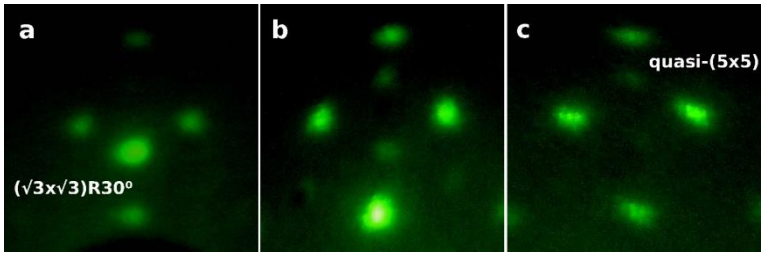

Figure 3 6: *Evolution of the inner diamond with temperature (and/ or time) as the (√3x√3)R30º spot- the one inside the diamond in the lower half- disappears and the quasi-5x5 spot – the one inside the diamond in the upper half- appears. In b. we see an intermediate step where both structures coexist in the LEED pattern. The images correspond to different samples and electron energies.*

b. Quasi-(5x5)/SiC(0001)

The quasi-5x5 superstructure is intimately related to the (6√3x6√3)R30º reconstruction. Both reconstructions appear under the same preparation methodology, but quasi-(5x5) appears occupying small regions of the surface. This reconstruction is scarcely appearing in STM sessions and therefore most people have considered it as a defective surface structure. It results difficult to quantify its partial coverage as it frequently appears in small patches inside the dominant (6√3x6√3)R30º. Anyway, it can also appear occupying regions of several tenths of nm. The quasi-(5x5) internal structure consist in set of atoms forming flower-like structures of 2-7 dangling bonds. As we have introduced before, the (6√3x6√3)R30º surface can be seen in terms of the sum of three (√3x√3)R30º nonequivalent lattices. According to this perspective, the quasi-(5x5) appears as islands of dangling bonds belonging to the same sublattice. The average distance between the protrusions is 5 lattice unit cells. In **Figure 3 7** we show a representation of this. One of the (√3x√3)R30º lattices is represented in **Figure 3 7 b** as an array of white dots. We can notice that the maxima of the dangling bonds coincide with the marked dots for some of the flowers, we have marked these dots with blue circles in **Figure 3 7 c**. The rest of the flowers maxima appear respectively in the positions of the other nonequivalent (√3x√3)R30 lattices, that are depicted in **Figure 3 7 c** as green and red circles shifted hexagonal lattices. All the dangling bonds within a single rosette belong to the same

(√3x√3)R30^{o} sublattice and surrounded by a region appearing lower in the STM images. The fist neighbor flowers from a green island are red and blue flowers, and the same occurs for the other combinations.

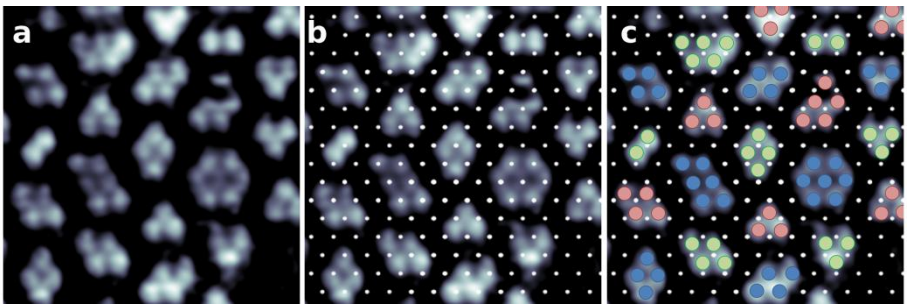

Figure 3 7: *Explanation model of the quasi-(5x5) superstructure .***a***. The STM image as recorder (filtered for ease the visualization).* **b***. One of the three sublattices is represented with white dots, the other two sublattices correspond to the middle of the triangles, on a when the triangles are looking upwards, and the other when the triangle are looking downwards. Every sublattice is represented with a different color: blue, green, and red.***c***. The tree lattices are represented.*

In **Figure 3 8** we show STM images of this superstructure. In **Figure 3 8 b** and **c** we show for the first time, up to our knowledge, the existence of the graphene intercalation between the quasi-5x5 structure. The graphene mesh is visible in the STM images in the dark regions between the rosettes as a small regular corrugation with 2.4Å periodicity. One explanation is a graphene sheet on top of the quasi-5x5 reconstruction, but other options shall be taken in consideration, such as graphene intercalated between the quasi-5x5 structures or even graphene under the quasi-5x5 structure. We believe that proving the existence of graphene between some islands of quasi-5x5/SiC(0001) is a demonstration that a rich pull of surface structures are possible on the SiC hexagonal surface and that most of them are not understood nowadays despite the big amount of scientific literature devoted to the topic. Further atomic-scale studies are necessary in order to fully understand the SiC high-temperature reconstructions.

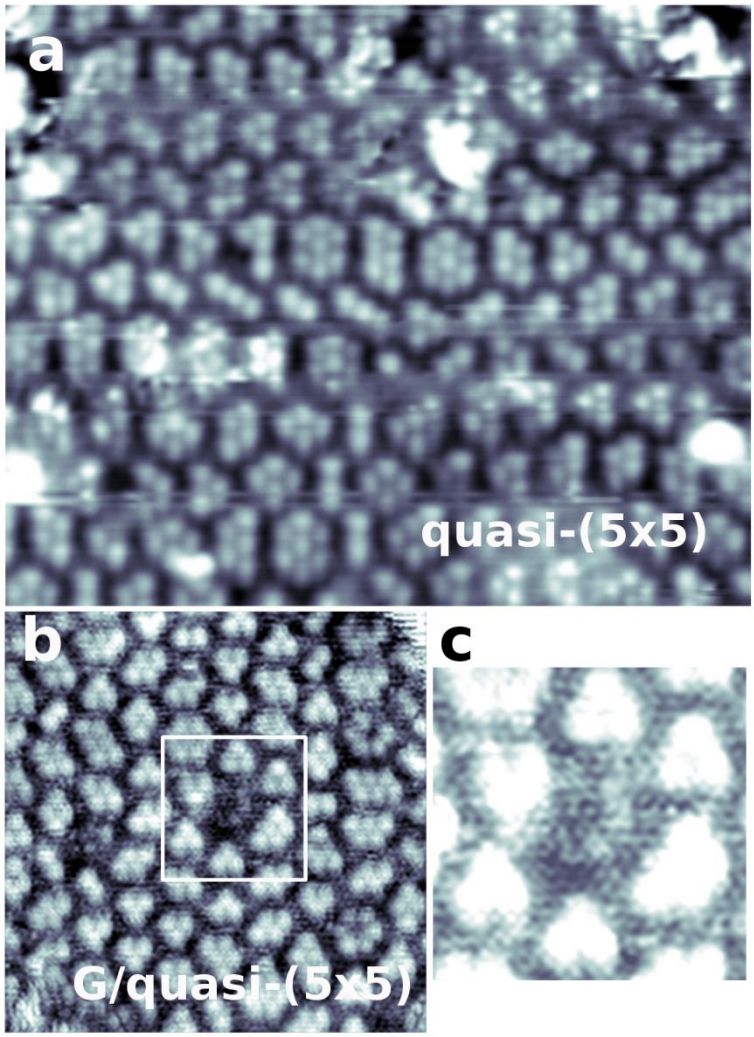

Figure 3 8: *STM images of the quasi-(5x5)/SiC(0001) reconstruction and the G/quasi-(5x5)/SiC(0001).* **a**. *20x16 nm^2, -3400mV.* **b**. *In this image the reconstruction is covered by a graphene overlayer, the white square marks the region highlighted in c, 14x14 nm^2, -400mV.***c.** *Detail of the b image corresponding to the white square in b, where the graphene lattice is visualized as a small corrugation, 5x5 nm^2 , -400mV.*

c. SLG/SiC(0001)

Graphite has been described on top of SiC(0001) surface by means of STM measurements as soon as 1991 by C.S. Chang *et al.* [37] and it was described before in 1975 by means of LEED and AES experiments [22]. In the work of Chang, the authors present atomically resolved images of a 6x6 structure with a smaller periodicity of 2.5Å on top of it; they correctly describe the structure as a graphite monolayer incommensurately grown on the Si-terminated surface of the SiC sample. This finding was presented soon after the invention of the STM and reveals that the SLG/SiC system is a stable phase of the surface that is relatively easy to measure. However, despite its brilliant origins, the full characterization of the SLG on buffer layers structure is still missing –most likely due to the absence of a true crystalline order- [34].

In **Figure 3 9** we present big scale STM images of a graphene covered terrace bigger than 100nm long. In these zoom-in series we observe that the collision of two nonequivalent domains of the underlying $(6\sqrt{3}x6\sqrt{3})R30^{o}$ structure forms a defective structure. This defective structure appears as a region where there is no underlying SiC substrate and thus the graphene layer is somehow suspended on a hole. In this defective region there are no subsurface artifacts that obscure the imaging of the pure graphene sheet and thus the honeycomb structure is nicely resolved. The line defect appearing o the **Figure 3 9 c** results from the coalescence of two shifted domains of the quasi-6x6 structure; once must notice that the lower regions of the two domains of the superstructure face each other but they cannot reconstruct.

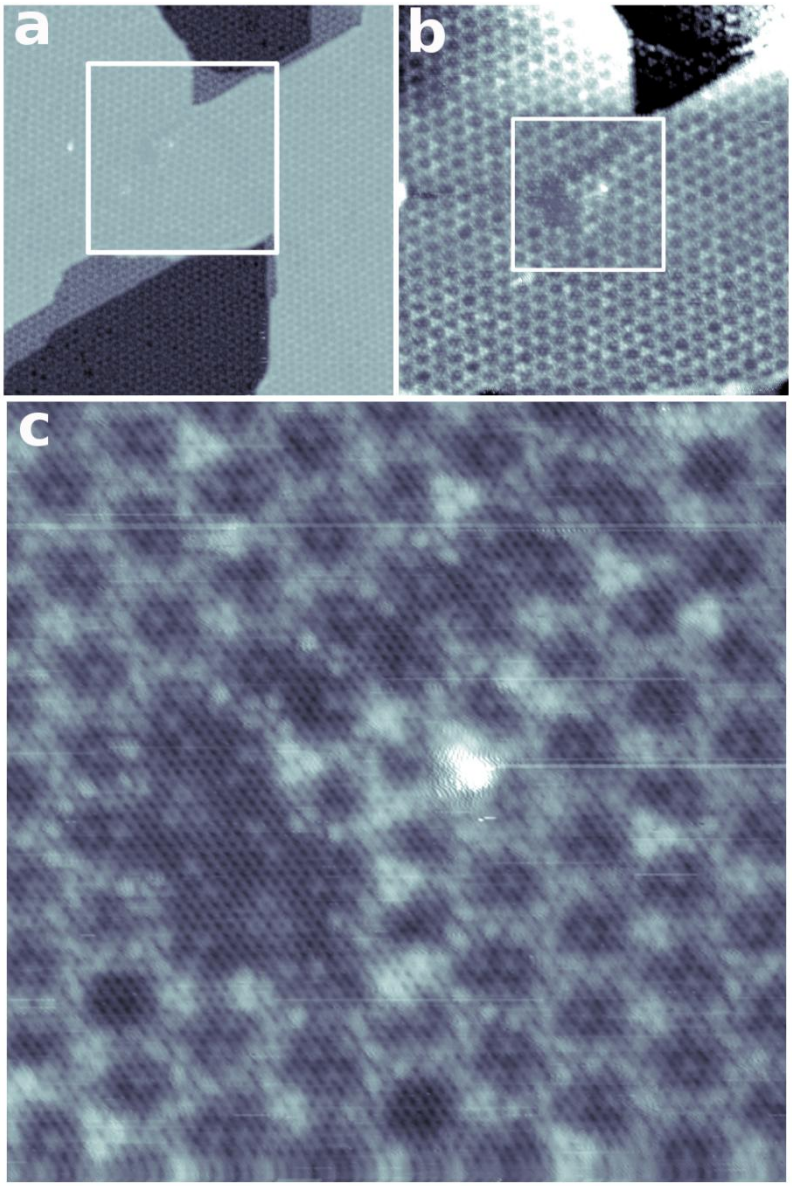

Figure 3 9: *STM images of single layer graphene on SiC(0001). The white square marks the region magnified in the contiguous image.* **a***. 100x100 nm^2,-1100mV.* **b***. 40x40nm^2,-1100V.* **c***. 15x15 nm^2,-1100V. In this image a defective zone is shown where there are missing subsurface atoms of the buffer layer, most likely due to the conjunction of two nonequivalent domains of the substrate.*

Epitaxial graphene on SiC present very interesting electronic characteristics. The first thing an STM experimentalist note when measuring this surface is that it exist a strong bias dependence on the STM images. Depending on the bias voltage graphene change from being almost invisible to becoming the most notable feature observed on the surface [38]. The subsurface dangling bonds, on the other hand, pass from being the most distinguishable feature to become severely screened by the graphitic layer which is on top. This bias dependent effect is related to the density of states of the 2D material and the Si substrate dangling bonds. In **Figure 3 10** we present a series of STM images of the same region at different tunneling bias. We observe how graphene becomes transparent at energies well above or below E_F [28]. Local spectroscopic measurements show a gap of ≈100meV [38] centered in the E_F ; this gap is most likely originated from the SiC substrate- .

Another interesting electronic effect is the defect-induced (√3x√3)R30º pattern on graphene due to intervalley scattering. This (√3x√3)R30º pattern shall not be confused with the (√3x√3)R30º SiC surface reconstruction. This purely electronic effect arises in the proximities of defects and vacancies as well as zig-zag and arm-chair edges [39]. This structure is very easily spotted on the G/SiC surface, while the interaction with other substrates , typically metallic, makes this purely electronic effect more difficult to find in G/metals than on G/SiC. This effect is explained in terms of quantum interferences between electrons belonging to each of the two nonequivalent sublattices in the k-space, i.e. each of the two nonequivalent Dirac-cones and is considered to be a fingerprint of π-like states close to the Fermi level [40]. The valley degeneracy is being related to the apparition of a conserved number analogous to the spin called the pseudo-spin. Under this formalism the (√3x√3)R30º pattern can be studied in terms of intervalley scattering or pseudospin rotation [39]. In **Figure 3 11** we present STM images of an arm-chair edge a zig-zag edge as well as point defects presenting scattering effect.

Figure 3 10: *(right page) Serie of STM images of the same atomic región 7x7 nm^2showing the bias dependence of the SLG/SiC(0001). When scanned at bias near the Fermi edge (100mV) the main feature is the graphene lattice, while scanned at higher bias (400mV) the subsurface buffer layer structure is revealed.*

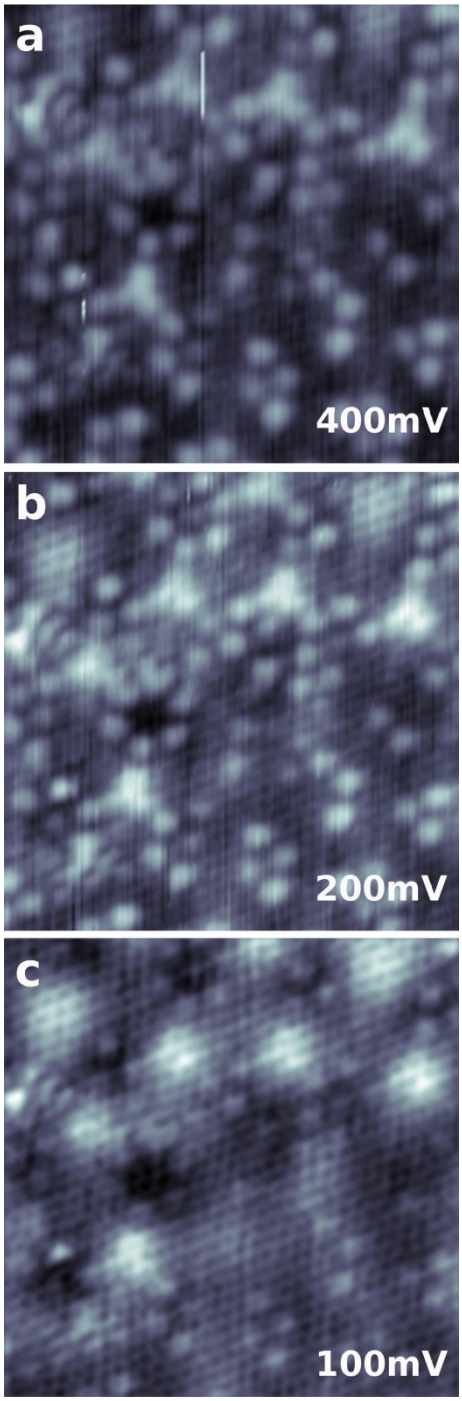
a
400mV
b
200mV
c
100mV

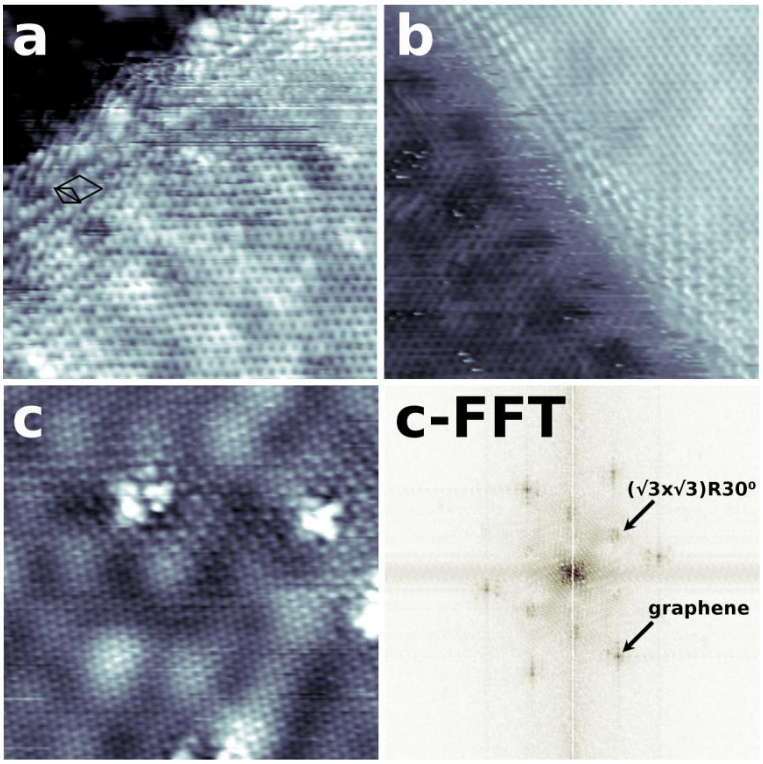

Figure 3 11: *STM images of the (√3x√3)R30° electronic interference pattern of:* ***a****. arm chair edge 8.4x8.4nm² V=100mV.* ***b****. Zig-Zag edge, 8.4x8.4nm² V=-100mV . c. Punctual defective region, 8.4x8.4nm² V=400mV, and a fast Fourier transform of the c image where the graphene dots and the (√3x√3)R30° dots are clearly spotted.*

In **Figure 3 12** we present a high resolution image of a small region of graphene. This image is performed during a lapse where our tip presented an exceptional characteristic that is normally called "giant corrugation" [41]. With this resolution, apparent heights within a single graphene unit cell can exceed the 2Å – for a lateral distance of 2.4 Å. This effect is poorly understood and several hypotheses have been proposed. However, we believe that it most likely involves the presence of some sort of small molecule or adsorbate– for example an H_2 molecule- attached to the apex of the scanning tip. This supposition is based in the recent results on CO (carbon monoxide) functionalized tips where an exceptional resolution of adsorbed organic molecules is achieved [42] and some experimental-theoretical evidences pointing towards hydrogen attached to the scanning tip as the source of the improved resolution [43]. Our supposition is that a

single molecule – of unknown nature- from the residual gas in the UHV chamber is confined between the tip and the surface as the lines of the electric field prevents its desorption. This involuntary functionalization do not usually last very long as any surface impurity, such as for example an atomic step, is normally enough for losing the giant corrugation resolution.

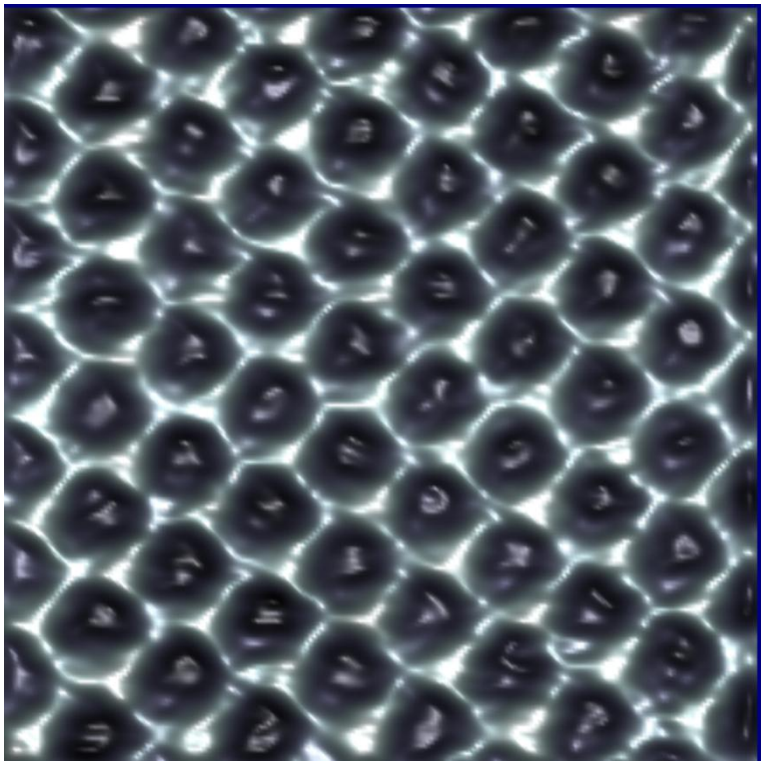

Figure 3 12: *3D representation of a high resolution image of graphene scanned under giant corrugation conditions. 2x2 nm^2, -1 nA, -100mV.*

In order to identify the chemical nature of our samples we have combined our STM results with syncrchrotron radiation photoelectron spectroscopy experiments measured in SuperESCA beamline in ELETTRA syncrotrone (Trieste, Italy) [44]. In **Figure 3 13** we present the overview spectrum of the sample annealed at 1400K recorded with a photon energy of 600eV. It results obvious at a first sight than now the C1s peak dominates the spectra, however because the photon energy is not the same than the one used for the previosly shown spectra (where a X-ray gun with an Al-Mg anode was used) the comparision between the diferent reconstructions can not be done directly.

It is important ot notice that the resolution that can be obtained in a syncrotron facility in XPS experiments is much better than the resolution that can be obtained in the in-house experiments. Therefore much more chemical information can be extracted from these spectra.

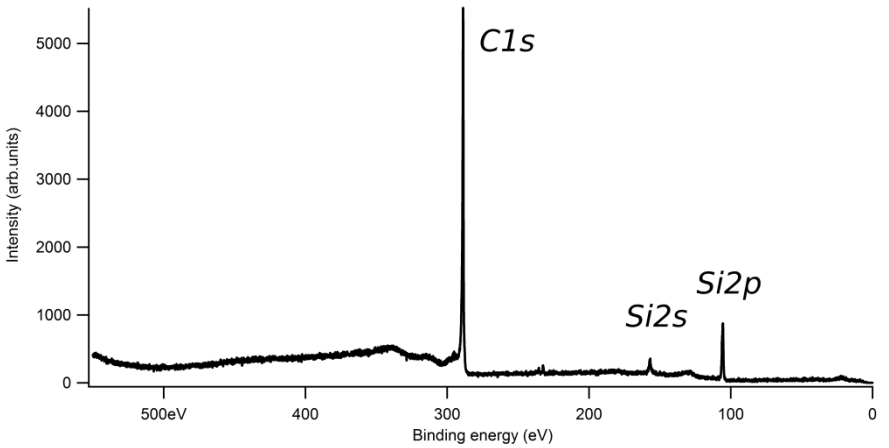

Figure 3 13: *Synchrotron radiation XPS overview spectra of the SiC sample annealed at 1400K recorded with a photon energy of 600 eV*

Synchrotron-based high resolution spectroscopy permits us to decompose the peaks into its basic curve-components; every component reflects a particular electronic environment (i.e. bonding configuration) and results from the convolution of a purely quantum Lorentzian energy distribution (FWHM 0.12-0.2 eV) with a Gaussian distribution (FWHM 0.4-0.7 eV). However, the carbon chemistry is very rich and the interpretation of the C1s spectra is not straightforward. The components corresponding to sp^2 and sp^3 bonding configurations measured for pure graphite and pure diamond respectively appear at very similar binding energies.

We have decomposed the C1s XPS peak of the as-grown G/SiC sample in 5 different basic components without using any asymmetry parameter. SiC is a wide gap semiconductor and therefore we use symmetrical peaks for the fitting. In **Figure 3 14** we show the C1s and Si2p photoelectron peaks decomposed in its basic components. The component appearing at 284.83 eV can be directly assigned to the graphene contribution (or C atoms in sp^2 configuration)[20], and is the biggest contribution to the C1s core level peak, with its 58.2% of the total area. This component is also important for calibration of the energy width, since it is narrow enough to test the

Lorentzian and Gaussian widths with a high precision. The components located at lower binding energies than the main peak (in our case 283.98 eV) are attributed normally to carbides, and we assign them to the C in the SiC bulk crystal. There are three other components at higher binding energies, which can in principle be assigned to different configurations of C atoms in the superficial rearrangement that takes place upon surface reconstruction. We assign these XPS components to surface related peaks [45] [46] [21] and name them with an S. in the way that follows: S.C-Si 1 at 285.26 eV, S. C-Si 2 at 285.73 and S. C-Si 3 at 286.4 respectively. We will later discuss the validity of this assumption.

The Si2p peak presents interesting information as well. The Si2p peak can be decomposed in 5 components, every of them consisting of a Si doublet. The binding energies of these components are 101.45 eV, 101.85 eV, 100.9 eV, 100.4 eV and 102.4 eV. The Si bonding configuration of every of these components is not straightforward, but we will try to elucidate the origin of every component of the Si2p curve. In the literature each group assigns components differently, Riedl *et al*. [20] describe the component resulting from Si-C bonds is located at 100.6 eV and the component arising from Si bonded to H atom is at 100.9 eV, they also assign a single component for the buffer layer located at higher energy. Johansson *et al*. in its seminal work about photoelectron spectroscopy of SiC surfaces were able to decompose their Si2p peak of the (6√3×6√3)R30° surface in four different components. They assign two of them, 101.4 eV and 100.7 eV to silicon in bulk configuration and the other two located at lower energies, -1.16 eV and -0.39 eV respectively, to surface components. In our analysis we have a better agreement with the work of Johansson et al., as we also find two bulk components at similar energies, 100.9 eV and 102.4 eV. However we find components at higher energies that we assign to surface-related silicon. We must emphasize, again, that to the best of our knowledge there is not a standard assignment of XPS components for the Si2p peak of G/SiC(0001) due to the complexity of the system and due to the difference in resolution between the different experimental setups used by the different authors.

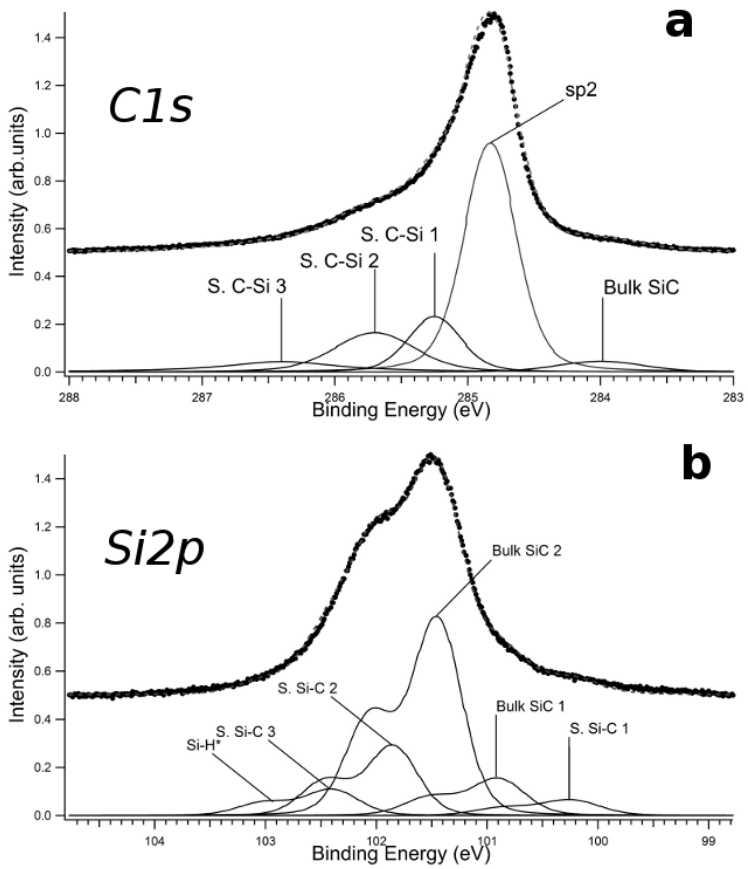

Figure 3 14: **a.** *XPS spectrum of the C1s peak of G/SiC sample annealed at 1400K measured at a photon energy of 400eV.* **b**. *XPS Spectrum of the Si2p peak of G/SiC sample annealed at 1400K measured with a photon energy of 150eV.*

It is important to notice that the surface stoichiometry changes very fast at these high temperatures. In a very narrow gap of temperatures the surface reconstruction changes very much and, as far as we know, there is not a clear consensus on the role of the duration of the annealing. As an example of this fast changes in the SiC in this temperature range we present the consecutive μ-LEED patterns of one sample annealed at different temperatures. As we see in **Figure 3 15** the LEED pattern of the electron-illuminated region changes critically in a temperature range of only 50K. For this high temperature annealing it seems that the partial pressure just on the vicinities of the surface results very important, as the gas molecules

populating this region will prevent that other atoms from the surface to evaporate from the material.

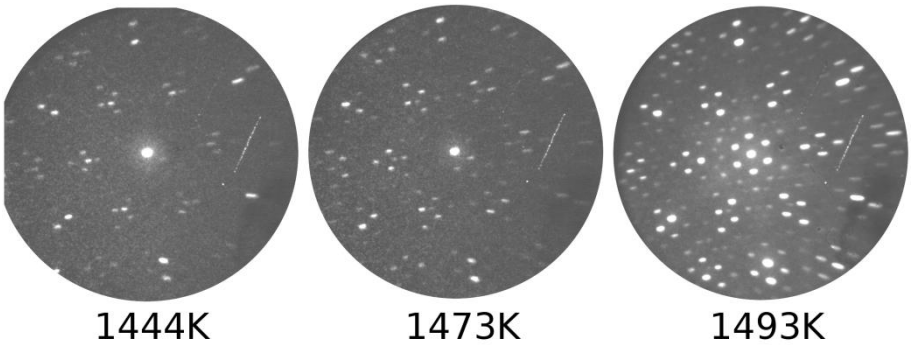

Figure 3 15: *μ-LEED pattern of the surface annealed at slightly different temperatures, showing great variation in a small temperature range.*

We have also characterized the clean SLG/SiC(0001) surface by means of LEEM measurements. This instrument is extremely useful in order to characterize graphenic systems as it can easily measure the precise number of graphene layers appearing onto the SiC surface or, in the case of graphene on metal systems, it results and appropriate tool for measuring the crystallographic angle between graphene and substrate [47]. For graphene grown on SiC it was found that the electron reflectivity curve shows a nice oscillation behavior with the kinetic energy of the impinging electrons and as a function of the number of graphene layers [45]. In **Figure 3 16i Error! No se encuentra el origen de la referencia. c** we present curves corresponding to three different domains appearing on the sample after annealing at 1525K. An image serving as an example of the typical LEEM measurements is presented in **Figure 3 16 a**. Three different contrasts can be distinguished at this energy and at some energies two contrast might look very similar–it is important to notice that the system reflectivity is severely dependent on the electron energy-, to ease the visualization we have marked every of these contrasts by enclosing them in colored polygons. Thus we have three regions: the red, the blue, and the grey ones. In order to know to which structures we can correlate these domains we need to perform a LEEM I(V) measurement and measure the reflectivity (brightness) of every domain depending on the electron energy. This is what is shown in **Figure 3 16 c** where three different reflectivity trends are clearly resolved. It is possible to relate the number of minima with the number of graphene layers and thus the blue domains would

correspond to bilayer graphene, the red domains to (6√3x6√3)R30^{o} and the white dominating background can be correlated with single layer graphene, with partial coverage for 1525K in good agreement with the previous literature [48]. Thus we can conclude that after annealing at1525K around 60% of the sample is SLG, 20% BLG and 20% buffer layer.

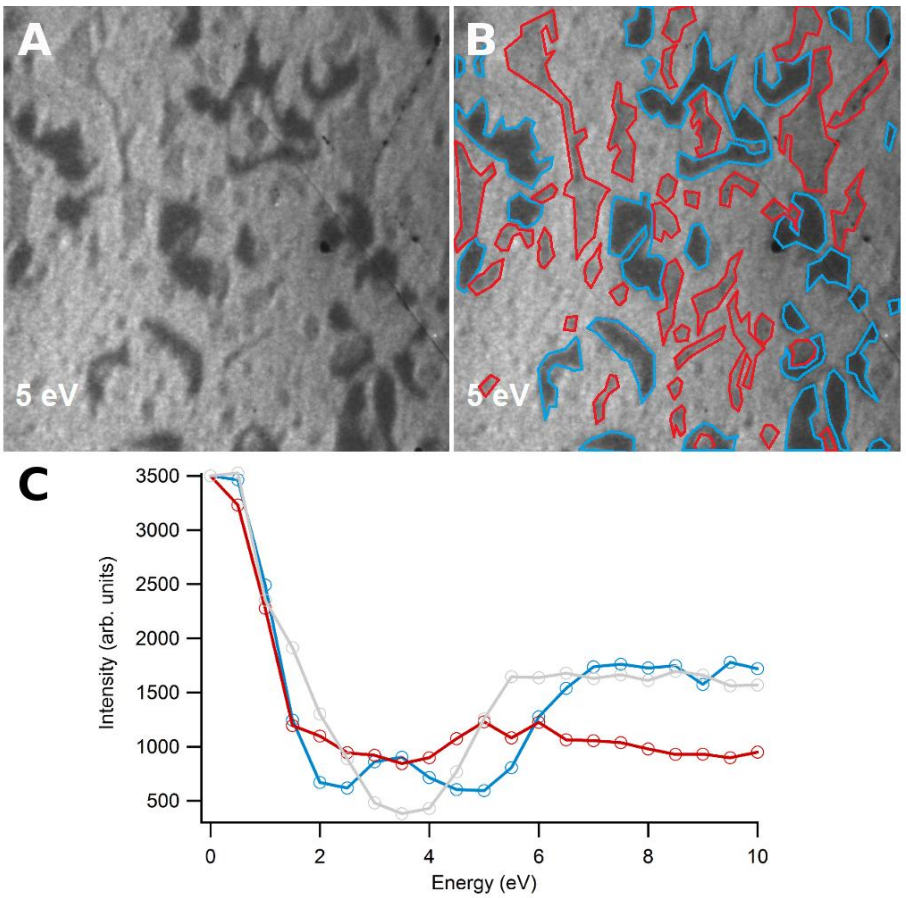

Figure 3 16: a & b. *LEEM imagse of a sample annealed at 1525K where three different contrasts are visible when using 5eV electrons for imaging it. The right side presents the same image where the different contasts have been highlighted for ease the visualization.* **c***. reflectivity curves for the colored regions in the images showing a correlation between the number of minima and the number of stacked graphene layers. 2x2µm^2.*

At last, we have not only realized experimental efforts to characterize the SLG/SiC system, but we have also performed theoretical calculations of the

substrate in order to fully characterize to the atomic scale the system. However the full determination of the exact atomic positions by means of DFT results very difficult to determine due to the high number of atoms involved in the unit cell. Up to the date there have been several attempts to perform this calculation and several strategies have been explored [49] [31]. Some works in order to reduce the number computational efforts have modeled the system through a smaller unit cell (for example 5x5 [28] or 3x3 [25]) or by including atomic-scale defects [32]. Up to our knowledge most theoretical approaches realized up to now lack of full reliability when confronted with experimental results – although the most important features are correctly described. Only very recently, some convincing results relating to the growth process have been performed concluding that SiC(0001) act as a template for graphene growth [26]. Moreover the full energy landscape of the different reconstructions –from zero- to trilyer- was calculated [50].

In our calculations we have relaxed a full $(6\sqrt{3}x6\sqrt{3})R30^{o}$ unit cell by two independent methods. First though the use of the efficient localized basis set FIREBALL code, second using a clever approach in order not to obtain spurious solutions of local energy minima. The main results are presented in **Figure 3 17** where the three projections of the relaxed unit cell together with a simulated STM image are presented. The relaxed structure corresponds to a graphene-like layer covalently bound to the topmost Si layer acting as a buffer layer. This layer is highly corrugated with a buckling in the order of Å and its electronic properties are far from those of freestanding graphene. On top of this we have a completely flat graphene layer which is the SLG. The STM simulations do not reproduce the underlying dangling bonds, but they correctly reproduce the 6x6 periodicity. The mean distance between buffer layer and SLG is 3.3Å and the corrugation of the graphene layer is negligible. However, these results should be treated with caution, evermore when they include- as it is the case in here- a big number of atoms. We can see them as a starting point for the understanding of the material and future more precise calculations.

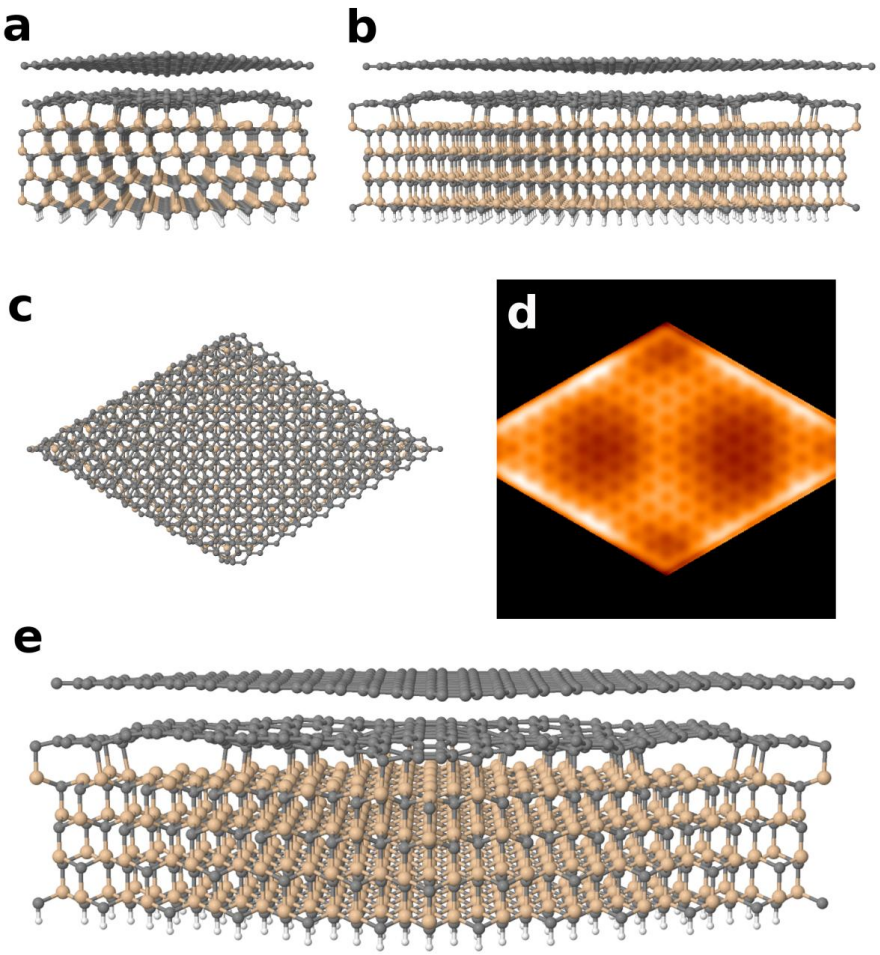

Figure 3 17: *Theoretical schematically presented model of SLG/SiC(0001).* **a***. Lateral side of the unit cell.* **b***. Lateral side of the unit cell.* **c***. Top view of the unit cell. The periodicity corresponds with the one of (6√3x6√3)R30º reconstruction.* **d***. Preliminary results on the simulation of the STM image of the unit cell depicted c. e. Perspective view of the unit cell of the SLG/SiC(0001). Due to time-economy considerations in the DFT calculations only four SiC slabs have been introduced. The lower part of the slab is saturated with atomic H.*

This structure can be seen as the basis for multilayer graphene. The second –and subsequent- layers of graphene are going to stay on top of the first –previous- sheet at a mean distance of around 3,4Å [50]. In the next section we

will briefly introduce the main experimental results obtained for higher order stacking, i.e. structures of SiC involving more than one layer of graphene.

d. BLG/SiC(0001)

It was as soon as 1998 when people noticed that heteroepitaxial graphite could be successfully grown on 6H-SiC(0001) [51]. However, it was not until the characterization of the products resulting from the mechanical exfoliation of HOPG samples in 2004 that multilayer graphenic system on SiC focused the attention of the surface science community. Since that, the multilayer graphene on SiC system has been characterized through means of different techniques such as ARPES,STM,LEED I(V),LEEM… [20] (see for instance the cross-sectional high-resolution transmission electron microscopy observations of Norimatsu and Kusunoki [52]). Usual experiments, involving samples annealed at temperatures in the range 1400-1800K, present coexistence of stackings with different number of layers. Atomic scale microscopy investigations reveal that it is very difficult –if not impossible- to obtain samples where only SLG or BLG exists. Some advances have been performed in the quality of the number of layers by annealing the samples in furnaces with atmospheric Ar atmospheres, but even thought, the most usual result is coexistence of different stackings, as an example of this the surface of **Figure 3 16** where SLG and BLG coexist . Because the intrinsic difficulties in measuring the temperatures in this range it is not a clear consensus on the exact temperature needed for every superstructure. However, there is a clear correlation between the higher annealing temperatures and the coverage of more than one graphene layer. For instance Huang et al. describe monolayer to occur at 1475K, bilayer at 1525K and trilayer at 1575K [53].

We have also noticed the coexistence of several reconstructions on a single sample. In **Figure 3 18** we present LEEM images of a sample annealed at 1525K showing the same region under illumination with different electron energies. As we have already discussed in the previous section bilayer graphene has a double minima reflectivity curve and, it corresponds to the dark regions in the images at 2eV and 5eV or the bright regions in the 3.5 eV image (see **Figure 3 16**). It is important to notice that at energies above 7eV it results very difficult to distinguish it the bilayer from the monolayer domains.

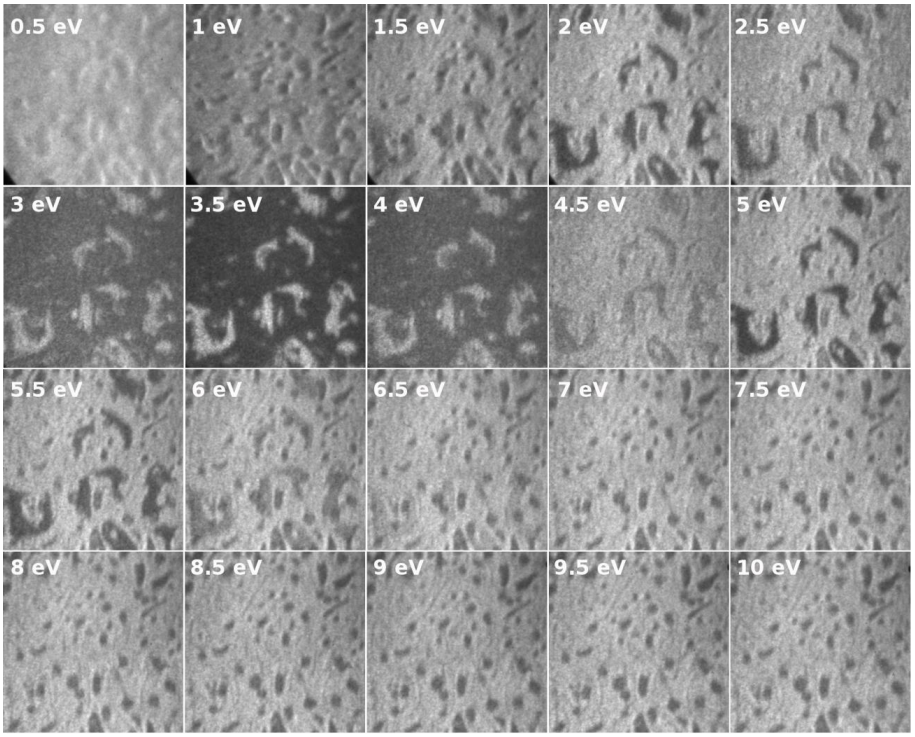

Figure 3 18: *Selected frames of the LEEM I(V) video where islands of bilayer graphene are clearly spotted in 2 eV and 5eV as dark regions and at 3.5 as bright regions.1.5x1.5μm^2.*

We have also characterized BLG by means of STM. Its appearance when scanned with STM conserves the quasi-6x6 periodicity and the honeycomb atomic scale lattice. The main difference is the absence of underlying protrusions from the buffer layer; the typical dangling bonds that dominate when scanning at bias far from the Fermi level, are not longer observed in BLG. This effect is most likely due to electronic screening of these states by the first graphene layer. In **Figure 3 19** we present atomically resolved STM images of bilayer and trilayer graphene. In the bilayer image we see an atomic-scale defect which promotes the apparition of the typical (√3x√3)R30^o intervalley interference pattern in good agreement with previous literature [40]. The trilayer graphene , on the other hand, can be easily distinguished because it no longer conserves the quasi-6x6 superperiodicity. Its electron density appears puzzled and amorphous. It has been described that the atomic honeycomb structure is no longer appearing and that instead the hexagonal atomic symmetry is observed – as for HOPG- [54]. We actually observe this hexagonal behavior in our atomically

resolved images, however we remark that these observations are very dependent on the tip structure and thus they cannot be taken very confident. For instance BLG theoretically should express the hexagonal symmetry, and some experimental works confirmed it, but the actual consensus states that BLG can express both atomic symmetries –hexagonal and honeycomb.

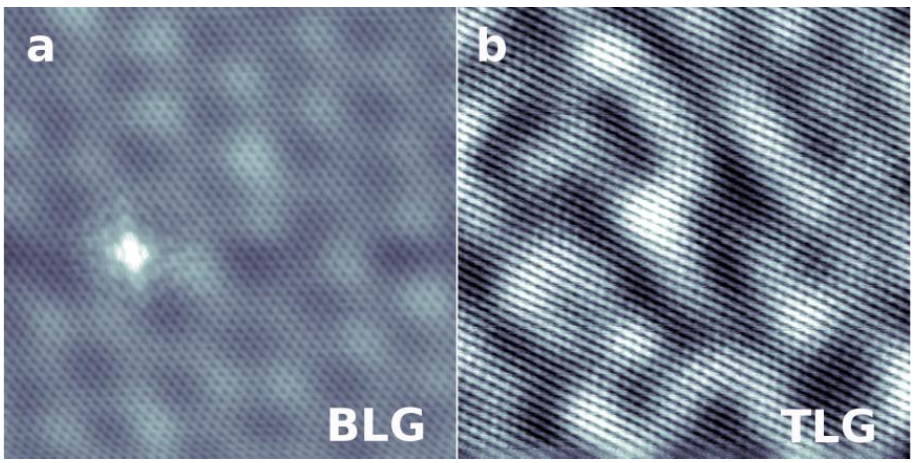

Figure 3 19: *STM images of multilayer graphene on SiC(0001).* **a.** *Bilayer graphene where subsurface buffer layer structures are not visible but the Moiré-like long range pseudoperiodicity is still conserved. An atomic scale defect- probably involving two pentagons- is spotted in the center-left of the image. 10x10 nm^2, -1100mV.* **b**. *A region whose small corrugation of graphene is clearly visible and probably consisting on 3 (or more layers) of stacked graphene, 10x10 nm^2,-1nA, -100mV.*

3.2. H/G/6H-SiC(0001) deposited at 300K

In our effort to fully characterize the graphenic systems grown on SiC we decided to explore the energy landscape through the use of adorbates. Our original idea was to understand the modification of the graphene properties when interacting with adsorbed molecules. For this analysis we need simple probes, i.e. simple adsorbates. Atomic hydrogen is the simplest possible adsorbate that one can imagine and therefore we decided to use it for our experiments. The usual experiment involves the graphitization of the SiC sample, its characterization by means of LEED and XPS prior to deposition, the atomic hydrogen exposure-typically $1x10^{-8}$ mbar during 10 min- by using an H-cracker and keeping the sample at room temperature and after all this processes the H/G/SiC characterization.

In 2006 it was experimentally discovered that atomic hydrogen attaches to graphite (HOPG) in the form of dimmers and small clusters [55] [56] [57], some years later researchers also noticed that a similar behavior appears when hydrogen is adsorbed on single layer graphene on SiC [58] [59]. It appears forming small adsorbate structures with defined geometry. The most common structure according to these works are small dimmers predominantly appearing on the high areas of the quasi-6x6 reconstruction. This behavior can be contrasted with that of H adsorbates on G/Ir(111) of G/Pt(100) where the hydrogen tends to form higher order clusters using the graphene Moiré as a template [60] [61]. Moreover it has also been described intercalation processes with hydrogen passivating the Si dangling bonds within the $(6\sqrt{3}x6\sqrt{3})R30^{o}$ reconstruction beneath graphene and yielding to buffer layer elimination [18] [29] [62]. Under this mechanism the buffer layer becomes SLG and the BLG reconverts to BLG. However there is not a clear understanding on the factors that influence the competition between the hydrogen adsorption and the hydrogen intercalation.

From a theoretical point of view the H/G system has been widely studied. From this perspective H chemisorbs on top of a carbon atom within the mesh and breaks the sp^2 original hibridization towards a sp^3 orbital arrangement. Several aspects of the system have been theoretically investigated [63] [64] [65] [66] [67] [68], including the full hydrogenization – graphane a 2D hydrocarbon [69]-, the combination with nitrogen adsorbates [70] and the colossal enhancement of spin-orbit coupling [71]. Moreover, even some theoretical attempts have been performed on the interplay between hydrogen adsorption and hydrogen intercalation on 6H-SiC(0001) [25], but there is still a lot of open problems on this topic.

In **Figure 3 20** we present large area STM images of atomic hydrogen adsorbates on graphene. In these images we observe two different coexisting substrates, at the right part of both images we observe a rougher substrate where the graphene lattice is visible but the underlying structure is still distinguishable and the underlying protrusions are spotted in the graphene region (see **Figure 3 20 b**). We conclude that the surface on the right part of the images correspond to SLG. On the other hand, the left side of both images has a smoother substrate which still conserves the quasi-6x6 periodicity. The graphene lattice can also be resolved and therefore we estimate this structure to be BLG. Interestingly the hydrogen adsorbates are spotted on both surfaces. This is an expected result as the hydrogen clusters were first reported onto HOPG [55] [56], and therefore nothing could make us to foresee that they would not be observed in BLG. It could appear that the number of H-induced protrusions on BLG are less than on SLG indicating that the sticking coefficient changes as the number of layers increase. However we regret we do not have sufficient experimental results to conclude how exactly the sticking coefficients result altered by the stacking sequence.

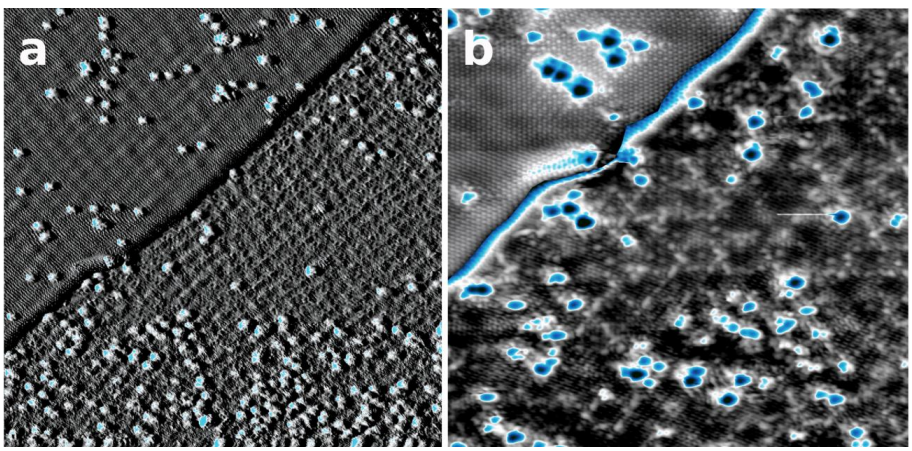

Figure 3 20: *STM images of the H/G/SiC system in a region where bilayer and single layer graphene coexist. H attaches to both reconstructions with a similar sticking factor.* **a**. *V=-0.6V, I=1nA, 40x40nm^2* **.b**. *V=-0.2V, I=1nA, 20x18nm^2. A double color scale is used for this image where both terraces (upper and lower) correspond to different color scales. This image treatment was performed to ease the visualization of the atomic resolution in both surfaces.*

These clusters are chemisorbed structures and thus the bonding between the hydrogen and the carbon atom underneath is very strong. However the strength of this interaction is not as strong as one should expect for a purely chemisorbed system, as the structures can be easily removed under STM scanning. Mild tunneling conditions –voltages near the Fermi level and small currents- are required in order not to desorb the adsorbates during the scanning. This effect can also be used on purpose, as it was noticed by P. Sessi *et al.* [72], and nanopatterning can be achieved by using controlled voltage pulses of bias higher/lower than 3V/-3V (although this values strongly depend on the tip). In **Figure 3 21** we present two consecutive images of the same region before (**a**) and after (**b**) a controlled voltage pulse. The upper left region of the presented graphene region was previously pulsed at high voltages and that is the reason why it looks clean of hydrogen adsorbates. We realized a 4V pulse on the position marked with a white arrow in the **¡Error! No se encuentra el origen de la referencia.** **a** image and we can see in the **Figure 3 21 b** a region of ≈25nm diameter where the adsorbates are no longer present. The diameter of the induced-evaporation area is directly proportional to the voltage used for the pulse, in good agreement with the previous bibliography [72].

This experiment promotes the question of where are these adsorbates going. There is not a clear answer, up to our knowledge, about this point, but some hypothesis can be presented. The most direct one could be that hydrogen result trapped by the tip as it has been described for many other adsorbates, that disappear during STM imaging. Functionalizing tips, by attaching different molecular, and atomic, species to its apex, is a well known process that has been described for many systems. Due to the volatile nature of atomic hydrogen and upon comparison with some previous experimental [55] and theoretical results [66], we believe that the more likely scenario is the tip-induced molecular formation of H_2. Upon electron excess, the atomic hydrogen desorbs and recombines to the more stable molecular form and escape to the gas phase.

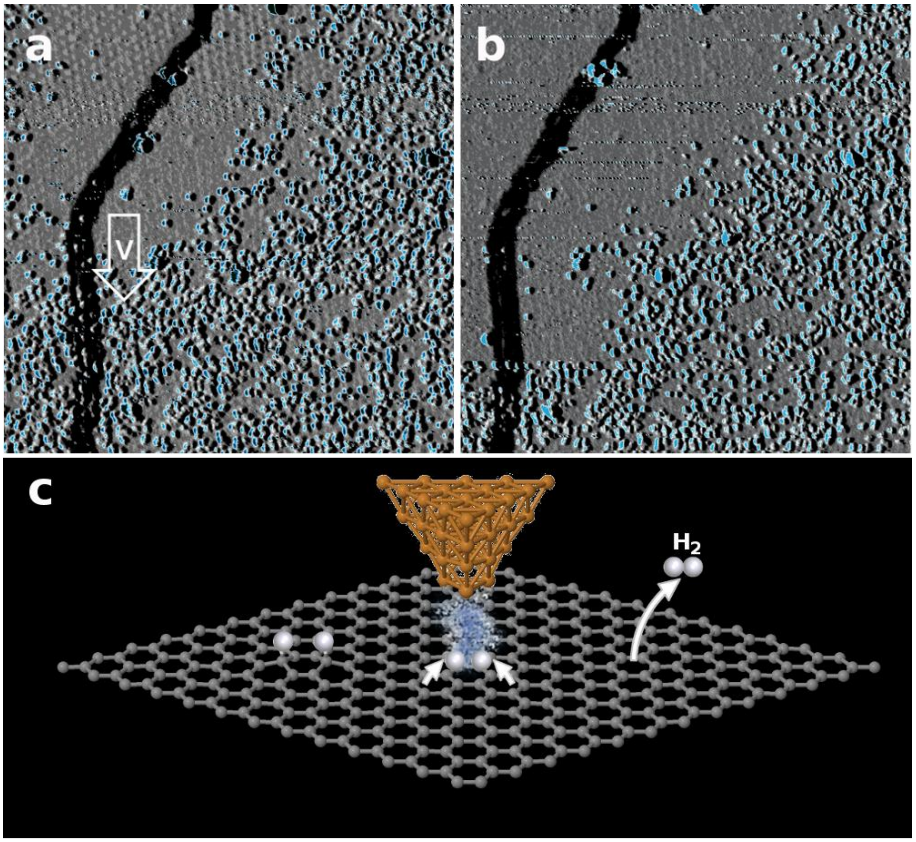

Figure 3 21: *Consecutive STM images of a region of H/G/SiC.* **a***. The white arrow marked with a V represents the place where a voltage pulse of 4 V was performed, V=2.2V, I=1nA, 80x80nm^2.* **b***. In this image we obseve that the voltage pulse has generated a region clean of atomic adsorbates on the surface V=2.2V, I=1nA, 80x80nm^2.* **c***. Schematic representation of the most likely process yielding to hydrogen desorption: H_2 molecular formation and subsequent evaporation upon manipulation.*

Medium scale images, as the one presented in **Figure 3 22,** reveal some intrinsic characteristics of the hydrogen adsorbates. The size and shape of most of them, although is not homogeneous, reveal that only a limited number of atomic scale structures are present in the surface. The graphene regions near these structures reveal the characteristic electronic (√3x√3)R30^o periodicity of intervalley scattering. The mean height of the adsorbates is around 1.7Å, as extracted from a histogram analysis. The clusters seem randomly distributed either isolated or forming higher order 2D-structures without any clear indication of what drives the clustering

process. In **Figure 3 22** there are no less than 350 clusters occupying around 15% of the total area.

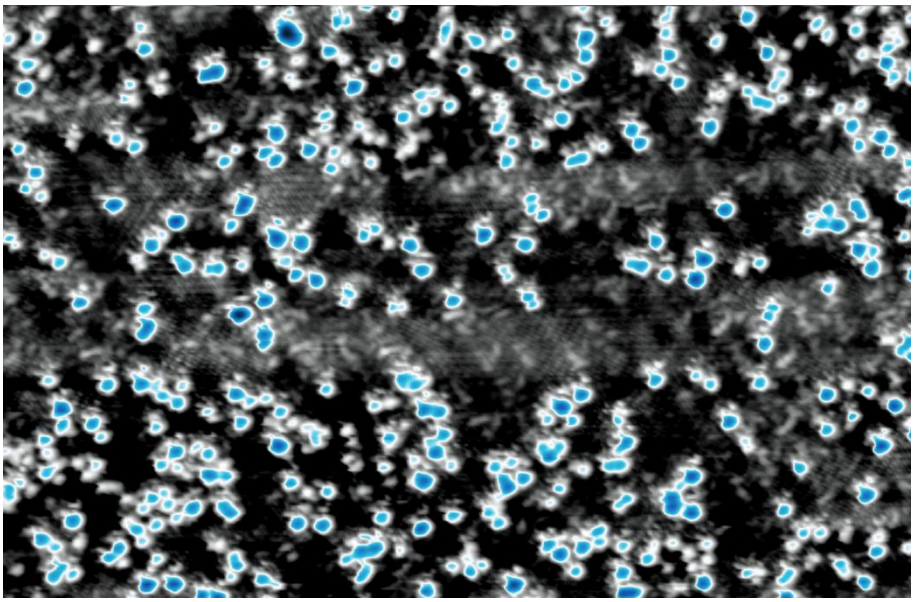

Figure 3 22: *STM image of hydrogen adsorbates on SLG where some identifiable patterns seem repeated. More than 350 clusters appear occupying 15%of the total area. V=-0.1V, I=1nA, 40x26nm^2*

In order to try to determine the most stable adsorption geometries we have performed high resolution STM images (see **Figure 3 23 a**). In these images we observe that only a limited number of atomic scale structures are present, more precisely we can divide the configurations into: small dimmers, big dimmers, ovaloids, trimmers and monomers. In **Figure 3 23 b** we have marked all these structures by enclosing them within colored geometrical lines. Thus the small dimmers are marked with green rectangles, big dimmers with red rectangles, ovaloids with white ellipses, trimmers with yellow triangles and monomers are marked with purple circles. It is very interesting to note that we have atomic resolution on the graphene lattice and the main crystallographic directions are easily distinguished; we can observe that the [11-20] is parallel to the vertical direction of the image. Using this direction as a basis we observe that the three equivalent possible orientations for the small dimmers (0^o, 60^o and 120^o) are observed into the same image. Something similar can be said about trimmers and big dimmers as two equivalent crystallographic

structures are observed. On the other hand this analysis is not so easy to perform on ovaloids as the structures seem somehow affected by the scanning direction (horizontal) and they appear distorted in the images.

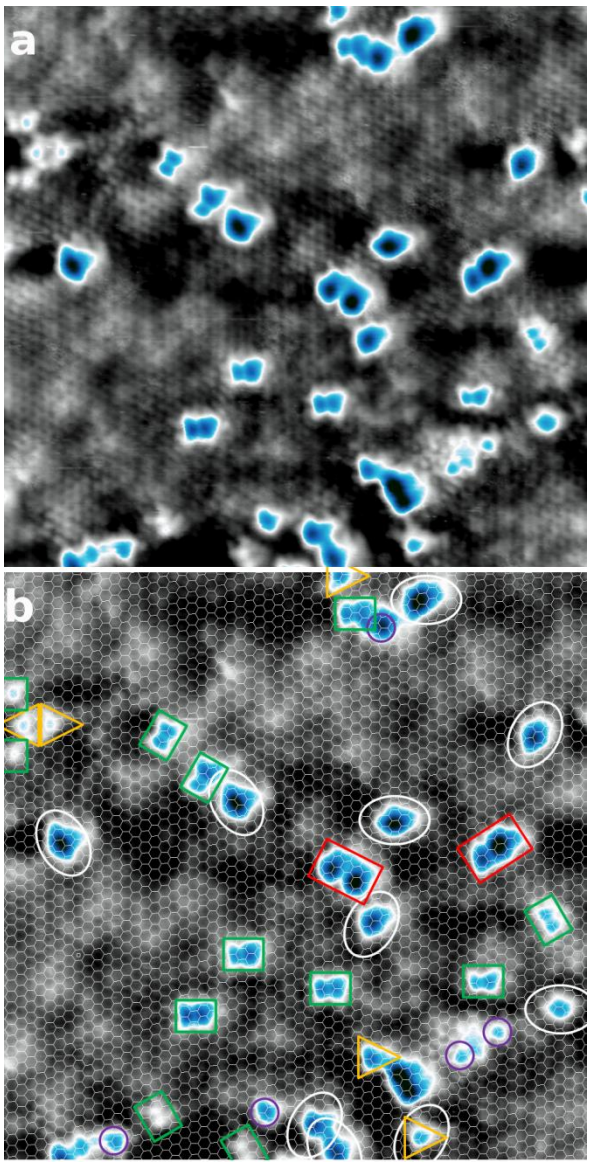

Figure 3 23: *High resolution STM images of hydrogen adsorbates on SLG forming small clusters.* ***a****. V=-0.3V, I=1nA, 12x12nm*^{2}*.* ***b****. Image where the atomic graphene grid has been superimposed and the clusters have been classified by a color code.*

The resolution in **Figure 3 23** is so good that we have tried to determine the exact atomic position of all the atoms in the graphene substrate lattice. This is shown in **Figure 3 23 b** as a small overprinted white honeycomb lattice. The exact positioning of this lattice is a very difficult task as drift effects, as well as other image deformations, result in a situation where the distances are non-homogeneously distorted in the different directions of the surface and in the different parts of the image. This has been done by identifying the hollow position of every ring and by distorting the three different directions of the honeycomb lattice with different correction parameters. We shall remark that we have placed manually many atoms, in order to fully determine the adsorption geometries of the hydrogen clusters with unprecedented resolution.

In **Figure 3 24** we present a smaller STM image where only two of the small dimmers are present and the graphene lattice is clearly resolved. Again in the contiguous image we have placed the graphene atomic grid and an ansatz of where the hydrogen atoms might be atomically positioned – provided that we assume chemisorptions on top of a C atom-. In the following we will constrain our analysis to the determination of the exact atomic structure of these small dimmers. There are three main reasons for this decision: First, because this structure is the most commonly observed during our experiments. Second, because the full determination through comparison with theoretical calculations of all the other structures would demand very computational-costly efforts and we focused on one of them to study the basic concepts of hydrogen chemisorption. And third, because among all the clusters, small dimmers are the most simple ones (i.e. smallest with internal structure).

The small dimmers present two asymmetrical lobes with a mean apparent height of 1.4Å. The distance between the maxima of both lobes is 3.2Å. At a first sight they seem to consist of two hydrogen atoms adsorbed on top of opposed C atoms of a particular ring, but this interpretation results very naïve, as we will discuss, and further DFT investigations are needed to determine the experimental data.

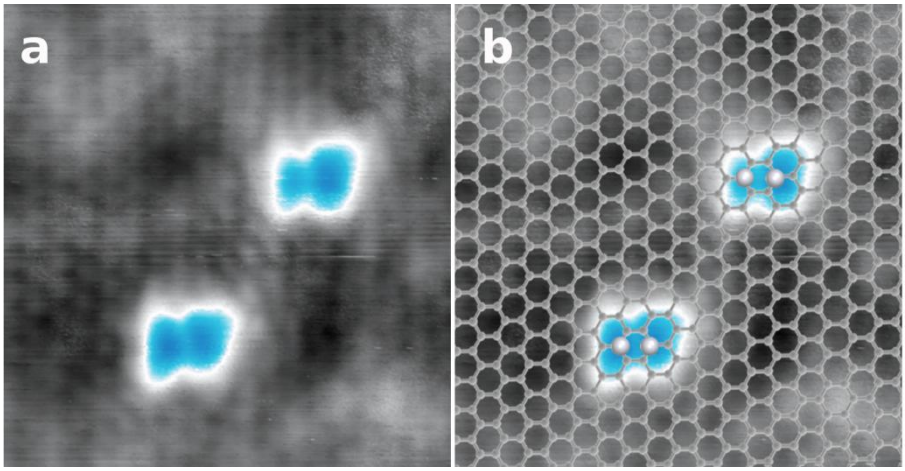

Figure 3 24: *High resolution STM images of hydrogen small dimers on SLG.* ***a****. V=-0.3V, I=1nA, 3.8x3.8nm*^{2}*.* ***b****. Image where the atomic graphene grid has been superimposed and a simple interpretation of where the hydrogen atoms might be chemisorbed have been overimposed*

To fully understand the system we have performed DFT calculations of the different possible theoretical absorption geometries. These configurations are presented in **Figure 3 25** where three different pairs are schematically represented and named according to the usual nomenclature. Thus, the first neighbor pairs are usually called ortho-dimmers (marked in white), the third neighbor pairs are called para-dimmers (marked in green), and the, less described fifth neighbors, we named the short-duo (marked in blue). The theoretical distances are: ortho 1.42Å, para 2.84Å, short duo 4.26Å, to be compared with our experimental value of 3.2 Å. Obviously we have disregarded other options –such as meta-dimmers, or second neighbor configuration- that do not present an orientation according to the experimental observations.

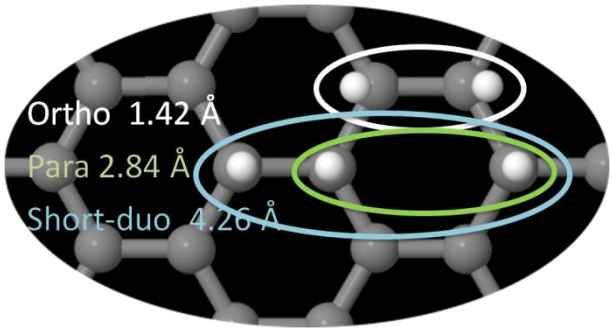

Figure 3 25: *Ball-and-stick model of the discussed dimmer configurations: ortho-dimmers (marked in white), para-dimmers (marked in green), and short-duo (marked in blue). The theoretical distances are: ortho 1.42Å, para 2.84Å, short duo 4.26Å, to be compared with our experimental value of 3.2 Å between lobes maximas.*

In **Figure 3 26** we present simulated STM images of the three described configurations. To ease the comparison we have also presented an experimental image and a modified experimental image with the substrate atomic grid overprinted. These simulations are performed using simple SLG as a substrate and with no buffer layer. This decision was taken in order to speed the calculations and because the role of the underlying buffer layer is not fully understood but believed to be secondary. As we can see the in the simulated images, the ortho-dimmer looks very different from the other two. This structure does not present a deep in between the two hydrogen positions and only one single lobe is resolved. This is true for most theoretical scanning conditions (placing the tip closer to the surface and different bias voltages). On the other hand the short-duo and the para configurations they do present a minimum and an asymmetrical configuration, which is in good agreement with the experimental input. The difference between them is indeed very small and comparison with the experimental data is convincing for any of the two configurations. The energy values for these configurations are -1.4 eV for ortho and -1.1 eV for short duo, indicating an energetic preference towards the ortho configuration.

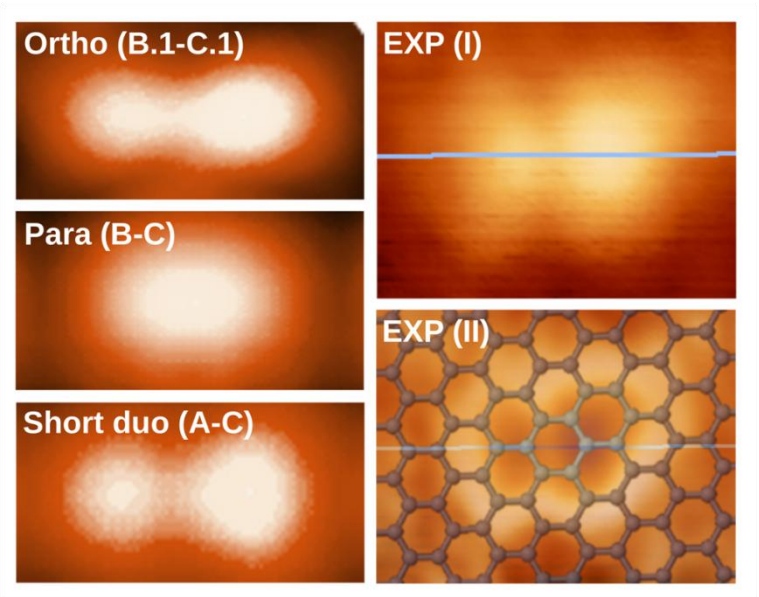

Figure 3 26: *Simulated STM images for the different proposed theoretical configurations of the hydrogen dimmers together with experimental images (with and without grid) for comparison.*

Simple optical comparison between experimental and simulated STM images does not clarify the atomic nature of the hydrogen dimmers. We have performed a profile analysis. The main results are presented in **Figure 3 27** where the theoretical profiles are presented together with the experimental results. Upon this analysis the short duo configuration looks closer to the experimental result than the para-dimmer, but this comparison must be taken with caution as both, the height and the x-y positioning, have absolute errors bigger than the difference between both structures. Moreover the experimental result appears broader than any of the proposed configurations and this yields us to the question of why is this happening, and if this is a tip effect or a intrinsic property of the hydrogen adsorbates on graphene. For this purpose we have separated the contribution to the density of states (DOS) of every of the C atoms of the substrate. These results are presented in **Figure 3 28.**On the left panel we show a comparison of DOS for the chemisorbed H, its first neighbor carbon, C_1, and its three equivalent second neighbor carbon, C_2. It comes as a surprise that, at the voltages used in the experiment, the main contribution to the STM image comes in fact from C_2 followed by C_1 and only marginally from H. Therefore the chemisorption of a single hydrogen produces in

experimental STM images intrinsically extended features of several Å of diameter, difficulting the determination of the precise position of the H atoms.

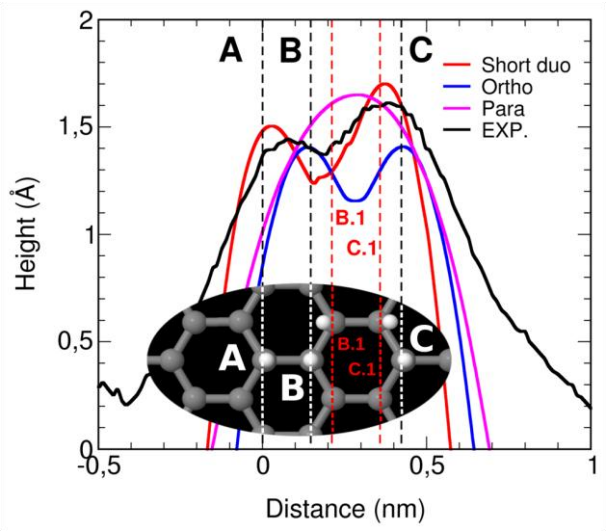

Figure 3 27: *Profile analysis of the different theoretical structures together with the experimental value.*

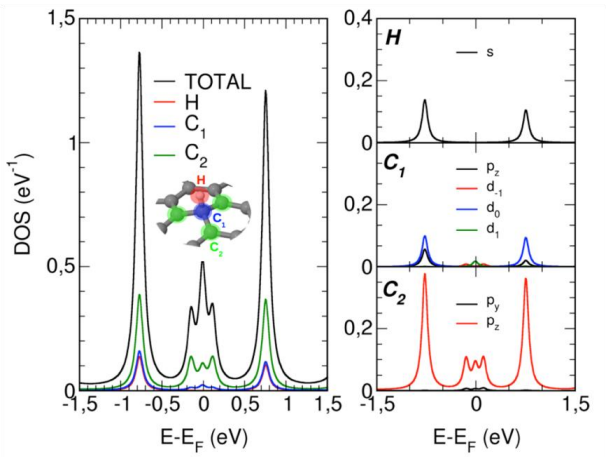

Figure 3 28: *Local density of states projected on a single chemisorbed H and its first and second carbon neighbors (C_1 and C_2)*

In conclusion we present STM images with unprecedented resolution of the hydrogen small cluster structures that appear onto SLG upon atomic hydrogen exposition. We combined the experimental results with theoretical calculations to fully determine the exact adsorption geometries of the most often found short dimmers. However, calculations show that the STM images present an important electronic effect, extended to the vicinity of the adsorbed adatom. This system is intrinsically complex to be described through STM simulations and only energetic configurations can determine the most favored structure. Upon these considerations the experimental short dimmers shall be related to para-dimmers. However, we believe the main result of this section is that the difficulty of identifying hydrogen clusters has been long underestimated.

The high resolution XPS spectrum of the C1s peak of a highly graphitized sample gives some insights into the chemical modification of the system upon hydrogen deposition. In **Figure 3 29** we present the C1s peak of the same surface before and after hydrogen exposition (2 min, $4x10^{-7}$ mbar). We observe that the chemical configuration is altered as the maxima of the peak slightly decreases in intensity and get shifted towards lower binding energies.

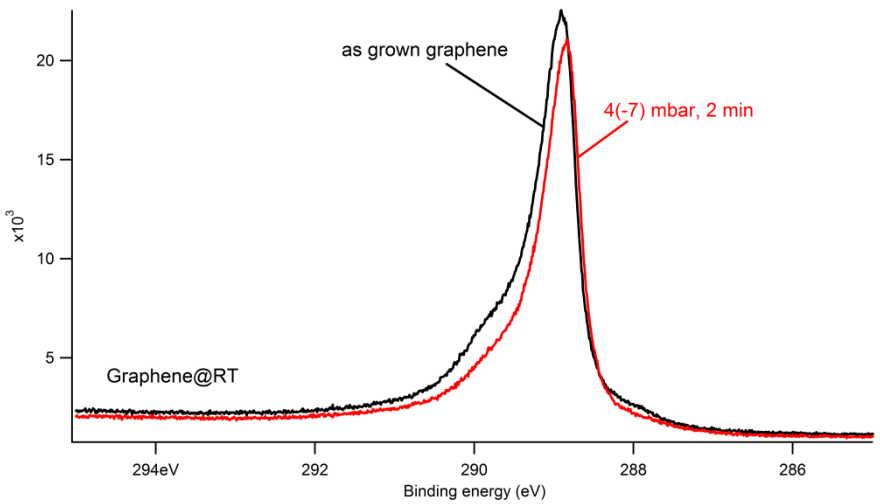

Figure 3 29: *Syncrotron based XPS spectra f a sample prior and after hydrogen deposition.*

3.3. C_{60}/G/6H-SiC(0001)

Mechanical stability, friction, or adhesion are among the physical properties that strongly depend on the strength of van der Waals (vdW) interactions. This is also true for the nanoscale. The nucleation and growth of molecular surface structures involve dynamic processes such as diffusion, molecular rotations, or conformational changes, which rely also on vdW intermolecular interactions [73] [74]. Moreover, self-assembly and adsorption studies focus on determining the preferred adsorption site and configuration, the adsorbate-adsorbate interaction, and the distance between the adsorbate and substrate (e.g., Ref. [75]). There is an increasing interest in the role of vdW interactions of organic molecules on graphite and other surfaces [76].

Generally, long-distance forces as vdW are not described by the most widely used DFT functional). Thus, in many of the works performed until now they are simply not included. However, when planar systems of carbon-based materials are in question, they require a different approach to the interplay between intermolecular (lateral) and adsorbate-substrate (vertical) interactions in determining the properties of ordered molecular structures. To evidence the important role of the vdW interactions in adsorption processes we have chosen a system of a very weakly interacting substrate and adsorbate, single-layer graphene (SLG) and fullerenes (C_{60}) [77]. The fact that both materials consist exclusively of carbon atoms arranged in an atomically thin planar mesh without H or any other atoms inside the atomic structure that could lead to long-range H-bond interactions makes this system a good prototype for a demonstration of the effect of these forces at a molecular level.

Thus, we consider the C_{60} on SLG grown on 6H-SiC(0001) [78] [7] [53] as a model system to test the strength of the vdW forces and mutual interactions that occur between neutral inert nanostructures. C_{60} adsorbed on surfaces generally tend to form hexagonal close-packed arrangements [79] in order to optimize their lateral interactions. In very recent studies of C_{60} molecules deposited on SLG epitaxially grown on metal [80] [81], it has been shown that the interaction between the molecules and the substrate, and consequently the molecular arrangement, is ruled by the Moiré unit cell. The C_{60} coming to the surface are trapped in potential wells of the Moiré valleys where the substrate SLG is more reactive, thus forming pinning centers for the other molecules that arrange in between. In contrast to these studies, we found a much weaker interaction of the C_{60} with the SLG grown on 6H-SiC(0001),

which lead us to a workbench to discuss the origin of the bonding mechanism in weakly interacting systems. Very recently a study of a very similar system appeared [82], which characterizes the basic behavior of the C_{60} on a graphene layer at 6H-SiC(0001) near to one monolayer coverage and studies its electronic properties based on scanning tunneling spectroscopy.

We employed a variable temperature scanning tunneling microscope (VT-STM) and DFT-vdW calculations [83] [84] [85] to prove that this system is solely governed by vdW forces. We determined the adsorption geometry of the molecules and we observed their collective motion. We also show that including vdW contribution in the calculations is necessary in order to fully describe theoretically the interaction between the sp^2 systems. To compare *in-situ* the interactions of fullerenes (C_{60}) with SLG and with the 6x6 we intentionally kept the SLG coverage below 1 ML, which resulted in a coexistence of SLG with the quasi-6x6 and quasi-5x5 reconstructions.

Behavior of C_{60} molecules deposited on the surface at room temperature has some noteworthy aspects. Absence of C_{60} on the SLG layers at room temperature is a clear indication that the molecules on the 6x6 are in a lower energy configuration than on SLG. The **Figure 3 30 a** shows C_{60} that literally escaped from SLG to the quasi-6x6 at room temperature conditions. Consequently these C_{60} remained trapped in a form of stable planar dendritic islands with the highest concentration of the molecules around the step edges, similarly to other studies [86] [87]. On the other hand, the depositions performed at 40K permit the perfectly ordered islands of C_{60} form on the SLG (**Figure 3 30 b**), most likely because the C_{60} are unable to cross the diffusion barrier at the SLG boundaries.

STM images of submonolayer coverage of C_{60} molecules deposited at room temperature (RT) onto a 6H-SiC(0001) substrate partly covered with SLG show slightly disordered close-packed hexagonal planar islands of C_{60} exclusively on the SiC buffer layer. That is, neither islands nor single molecules were spotted on the areas covered by SLG, because adsorbed C60 diffuse out of the SLG regions. On the contrary, when we evaporate C60 on the sample kept at a low temperature of 40 K (LT), STM images show the formation of C60 epitaxial structures on SLG in the form of well-ordered planar islands with a configuration that seems to have a twofold symmetry. **Figure 3 31 a** and **b** show the STM topography of islands on both types of surfaces and adsorbed molecules in detail.

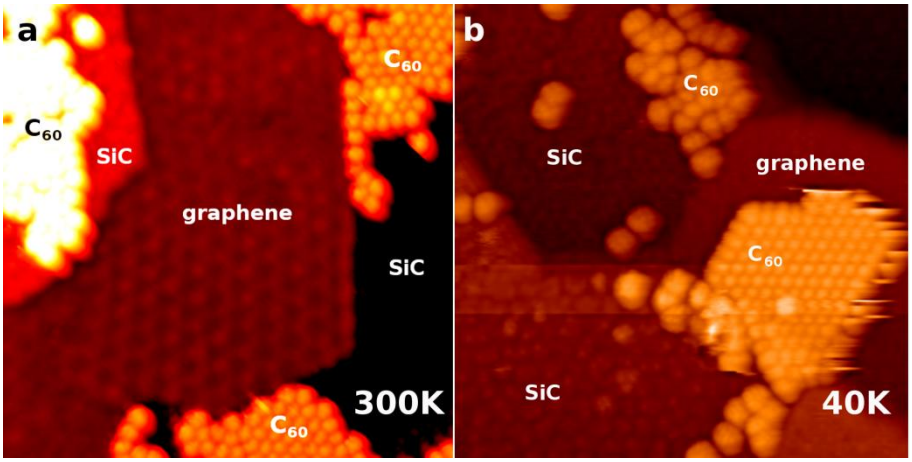

Figure 3 30: *STM topography images of C_{60} deposited on a mixture of SiC(0001) phases at a) room temperature, with the C_{60} islands exclusively on the quasi-6x6 phase and b) at 40 K with C_{60} islands forming also on SLG. The molecules adopt higher order on the SLG compared to the molecules on 6x6. Both images have 30x30 nm^2 and were taken at 1.5V bias voltage and 100 pA tunnelling current*

At first glance the properties of the C_{60} islands on quasi-6x6 (**Figure 3 31 b**) are very similar to the ones reported before at RT [86] [87]. The molecules inside the island are present in various orientations. Different molecular orbitals (MO) are exposed to the probe during scanning. The internal electronic structure appearing in the STM images of C_{60} has been extensively studied and it relates the aspect of the fullerene with the orientation. Normally the bright lobes within the molecule appear on the pentagons of the C_{60} molecule. In the C_{60} islands on quasi-6x6 the molecules seem randomly orientated (see **Figure 3 31 b** ,and **Figure 3 32**) .Their corrugation is 0.45 Å rms and the base apparent height is 7.2($\pm$0.5) Å . On larger scales, two quasiperiodic arrangements could be found corresponding to a pair of twin domains appearing at $\pm 20^{\circ}$ (with 1^{o} error) with respect to 6x6. The measured orientation matrix respect the substrate is: $\begin{pmatrix} 12 & 2 \\ -2 & 10 \end{pmatrix}$

On the other hand, the C_{60} islands on SLG in **Figure 3 31 a** show lower corrugation (0.28 Å rms), a considerably denser packing, and an almost perfect intramolecular order. According to the FFT power spectrum of the STM image in the inset of **Figure 3 31 a**, the C_{60} molecules arrange in a 4x4 commensurate superstructure with respect to the SLG lattice. As a rule, the islands are hexagonally shaped with edge angles of 120^{o}, which is an

expected kind of behavior, since it has been already observed in the first layer of C_{60} on highly oriented pyrolitic graphite [88]. The profile analysis of the islands gives an apparent height of 8.8(±0.3) Å and interestingly does not show medium-scale corrugation that could be expected due to the underlying quasi-6x6 corrugation of the SLG.

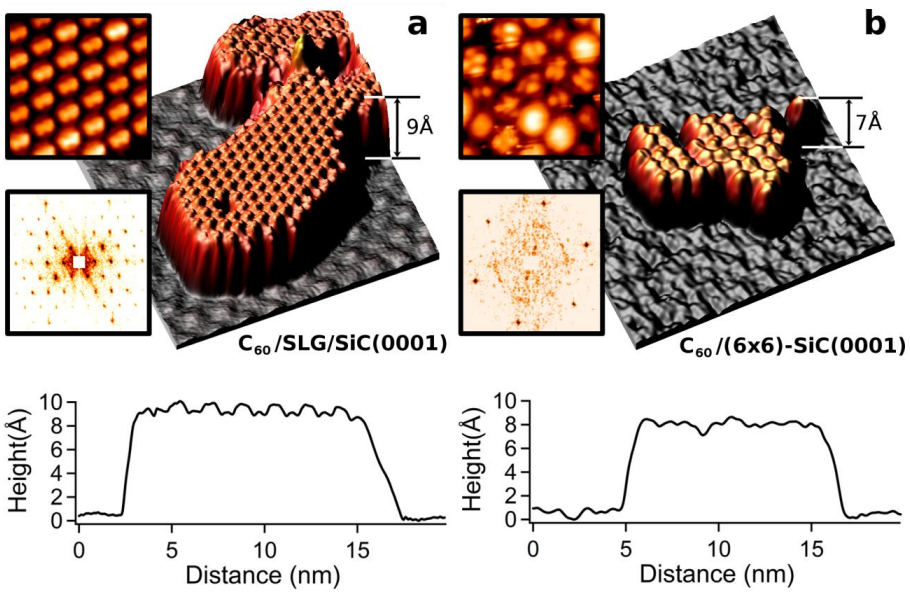

Figure 3 31: *Three-dimensional (3D) representation of 20x20 nm² empty states STM topography on C_{60} islands and their corresponding profiles.* **a**.*SLG at 600mV, 100pA, with a 5x5 nm² detail and FFT power spectrum of the entire area showing a clear 4x4 pattern of the close-packed arrangement of the molecules on SLG.* **b**.*(6x6)-SiC(0001) recorded at 1000mV, 100pA and a 5x5 nm² detail and FFT power spectrum of the entire area. Both images were obtained at 40K.*

The detail in the inset of **Figure 3 31 a** shows submolecular resolution, which suggests the adsorbed molecules on SLG are all equally oriented. The intramolecular structure of each C_{60} consists of two bright lobes that shall correspond to charge excess within their MO, which may be considered as a fingerprint for their orientation [79] [89] [90]. The most intense features are usually assigned to the C60 pentagons. However, in our case, the MO contrasts are slightly varying between subsequent STM images while maintaining the overall character. **Figure 3 32** evidences changes of the

probe itself and prevents us from directly relating the observed contrast to any expected MO of C_{60} molecules previously reported [79] [89] [90]. To unambiguously determine the correct orientation of the molecules on the surface based on these data, we have to assume a C_{60} being picked up by the reactive metallic tip apex before the acquisition of the images, since this process is commonplace, especially in LT STM sessions—e.g. Refs. [91] and [92]. Therefore, the observed STM contrast on the MO is most likely influenced by imaging of a C_{60} by another C_{60} adsorbed on the tip apex.

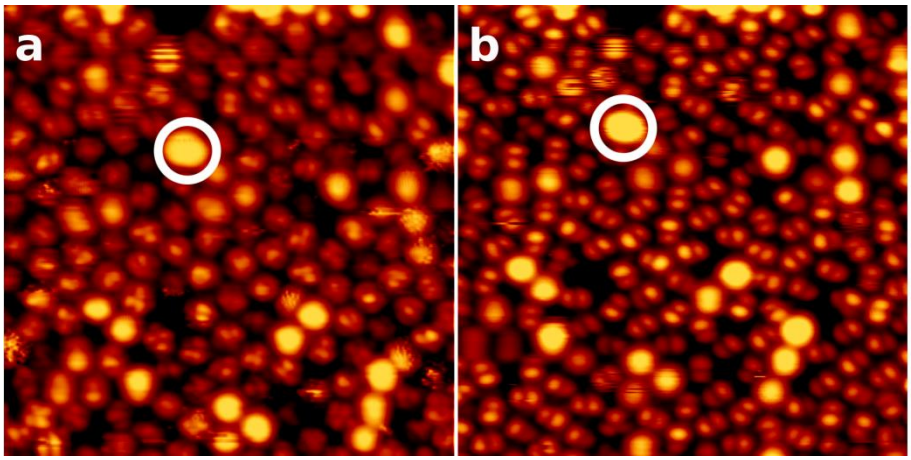

Figure 3 32: *Consecutive STM images where different contrasts are obtained for the same molecular layer. a. Metallic tip. b. Probably a C_{60} tip. The white circle marks a reference to ease the visualization.*

Consequently, the most important questions that arise from the experiment are about (i) the detailed role of the vdW in the well-ordered 4 × 4 C_{60}/SLG system and (ii) the orientation of the C_{60} with respect to the SLG lattice.

We performed extensive DFT-vdW calculations in order to understand the role of the vdW in stabilizing this structure. Several groups have developed DFT-based calculations including the vdW interaction [83] [93] [94] [95]. Here we use the LCAO-S^2 previously applied to SLG and graphene-likematerials [84] [83]. In this formalism, we consider two contributions. The first arises from the small overlaps between the electronic wave functions of the C_{60} and the SLG, leading to an electronic repulsion, and the second, which is the vdW interaction itself, is due to oscillating dipoles in both interacting systems. These two contributions are treated in perturbation theory from a DFT calculation using the FIREBALL code [85]. This method takes into account

particularly the π-π interactions since the corresponding overlaps are the dominant effect in this weakly interacting system. The underlying SiC buffer layer was neglected, since the expected energy contribution to the C60 total energy due to the vdW interaction is at least an order of magnitude lower than the contribution due to the presence of SLG, considering the large separation of SLG and the buffer layer [96].

In the calculations we considered more than 20 different adsorption geometries of C_{60}/SLG in a 4x4 periodicity. These calculations have confirmed that the energetically most favorable structures are indeed those with a high symmetry. To discriminate the contribution of the vdW forces in the global structure, we made DFT calculations with and without incorporation of the vdW forces. The most stable structures among all the probed adsorption sites and molecular orientations are presented in **Table 3 1**.

The molecular orientations are labeled by a C_{60} feature exposed to the surface and the angle of rotation around the *z* axis (perpendicular to the surface plane) with respect to the diagonal of a 1x1 unit cell of SLG (see **Figure 3 34**). Thus, the 6:6/0º orientation corresponds to an adsorption of a C_{60} by a dimer shared between two adjacent hexagons parallel to a C-C bond in SLG; the 6:6/30º is identical to the 6:6/0º rotated by 30º around the *z* axis; hex/0º is a hexagon aligned with the SLG hexagons, etc. There are three possible adsorption sites of high symmetry on the SLG: on top of a C atom (adatom), in the center of a hexagon (hollow), and above the center of a C-C bond (dimer). The same nomenclature is used here for both the orientation of C60 on SLG as for the orientation of the C60 on the metallic tip used for the STM simulation

In **Table 3 1** we see that the lowest total energy (E_{vdW}) structure calculated including the vdW interaction is the 6:6/30º in a hollow site of SLG, which is used as the reference value for the relative energy of adsorption (E_{vdW}). The closest structure in terms of energy is the 6:6/0º, also in a hollow site, with a total energy higher by 6.44 meV/C_{60}. Taking into account that the experiments were performed at 40 K, the thermal energy is about 3 meV, which is approximately half of the difference between the two most favorable structures. Consequently, the system at 40 K should prefer the hollow6:6/30º adsorption geometry over the hollow 6:6/0º. The rest of the structures present values of the total energy that are much larger, indicating the strong influence of the C_{60} orientation with respect to each other in the value on the vdW interaction. Remarkably, the main difference

in the total energy comes from the molecule-molecule interactions ($E_{C60-C60}$) rather than from the interaction with the surface ($E_{C60-SLG}$), which is only slightly modified when the molecule is placed with a different orientation. As the $E_{C60-C60}$ differs for each adsorption orientation, it has the ultimate role in the final value of the E_{vdW}. Charge transfer from the surface to a C_{60} is negligible, amounting to ≈0.03 electrons/C_{60}, which has been suggested recently [82].

Interestingly, when we perform the total energy calculations without the vdW interactions (E_{DFT}), all four structures result about the same energy (with differences less than 3 meV/C_{60}) and therefore the orientation of the molecules in the islands on the surface would not have any particular preference under our experimental conditions. The introduction of the vdW interaction results in a considerable reduction of theC_{60}-SLG distance (d_{vdW} compared to d_{DFT}). That is a clear indication that the vdW interactions cannot be neglected in any similar system.

C_{60} orientation SLG adsorption site	6:6/30° Hollow	6:6/0° Hollow	Hex/0° Adatom	Hex/0° Dimer
d_{DFT} (Å)	3.4	3.3	3.5	3.6
E_{DFT} (eV)	− 0.006	− 0.006	− 0.004	− 0.004
d_{vdW} (Å)	2.7	2.7	2.9	2.9
$E_{C60-C60}$ (eV)	− 0.880	− 0.871	− 0.680	− 0.645
$E_{C60-SLG}$ (eV)	− 1.007	− 1.010	− 1.019	− 1.016
E_{vdW} (eV)	− 1.887	− 1.881	− 1.696	− 1.659
ΔE_{vdW} (eV)	0.000	+0.006	+0.189	+0.226

Table 3 1: *Total energy values per C_{60} for the various orientations in a 4x4 SLG supercell, with and without considering vdW interactions (E_{vdW} and E_{DFT}) and the associated equilibrium distances d_{vdW} and d_{DFT}. E_{vdW} is the sum of two contributions: the cohesion energy between the C_{60} molecules, $E_{C60-C60}$, and the interaction energy between a C60 and the SLG substrate, $E_{C60-SLG}$. The structure with the lowest energy value is taken as a reference for calculation of the reative total energy.*

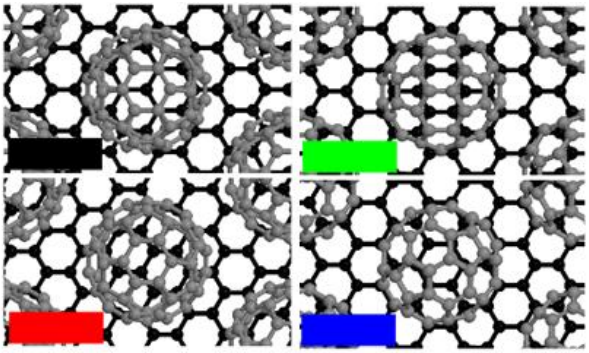

Figure 1: *Set of the most energetically favorable model structures fot C60 adsorptionon graphene.* ***Black****: Hex/0º Adatom.* ***Green****: 6:6/0º Hollow.* ***Red****: Hex/0º Dimer.* ***Blue****: 6:6/30º Hollow*

Aware that the total energy difference between 6:6/30º and 6:6:/0º is very small, we performed STM simulations for these adsorption geometries to elucidate which is the structure observed experimentally [97]. A set of 60 tips consisting of a pyramid of 35 metal atoms and a C_{60} molecule attached to the apex in various geometries has been used as a probe over both candidates. The calculated images were carefully compared to the experimental images with varying contrast. We found the agreement only for the structures based on the 6:6/30º orientation, as in the example in **¡Error! No se encuentra el origen de la referencia.**, where the best agreement is obtained for the 6:6/30º imaged with appropriate orientations of the C_{60} on the tip apex. The couples of bright lobes in the images systematically correspond to a pair of pentagons linked by a dimer between two hexagons, which is crucial to decide the mutual orientation of the molecules in the 4x4 structure. The calculated images are all similar to an image produced by a simple metallic tip, somewhat modified by the effect of the MO of a rotated C_{60} on the tip. Considering the high probability of having a C_{60} on the tip apex leads us to inevitably conclude that any spectroscopic information obtained by scanning tunneling spectroscopy on this system can be significantly distorted. In particular, the width of the gap between the highest occupied and lowest unoccupied states of a C_{60} is likely to be overestimated [82].

The resulting images were carefully compared with the experimental data for various types of submolecular contrasts over the most stable structure for the surface - the 6:6/30°. The corresponding tip models presented in our work are: 6:5/90°, 6:5/30°, atom/0°. From the identified positions of the C_{60}

it is possible to deduce that the movements of the C_{60} on the apex have rather a character of rolling around the axes perpendicular to the substrate. The bias of the STM simulation that reproduced the detailed features of the real STM topography was 1.0V. A purely metallic tip was also tried to simulate the images but it could not reproduce the variety of the observed features. The theoretical simulation is schematically represented in **Figure 3 33**. The comparison between simulated STM images and the experimentally obtained ones is presented in **Figure 3 34**.

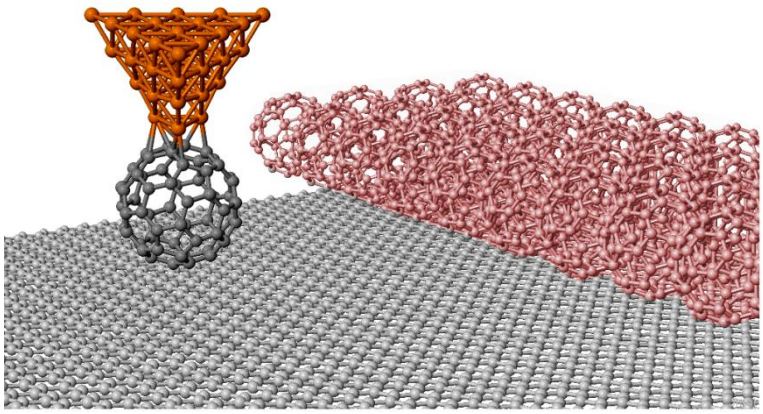

Figure 3 33: *Schematically representation of the best agreement model according to the experimental observations. The C_{60} form a 4x4 ordered close-packed superstructure on top of SLG. A C_{60} molecule is attached to the scanning tip.*

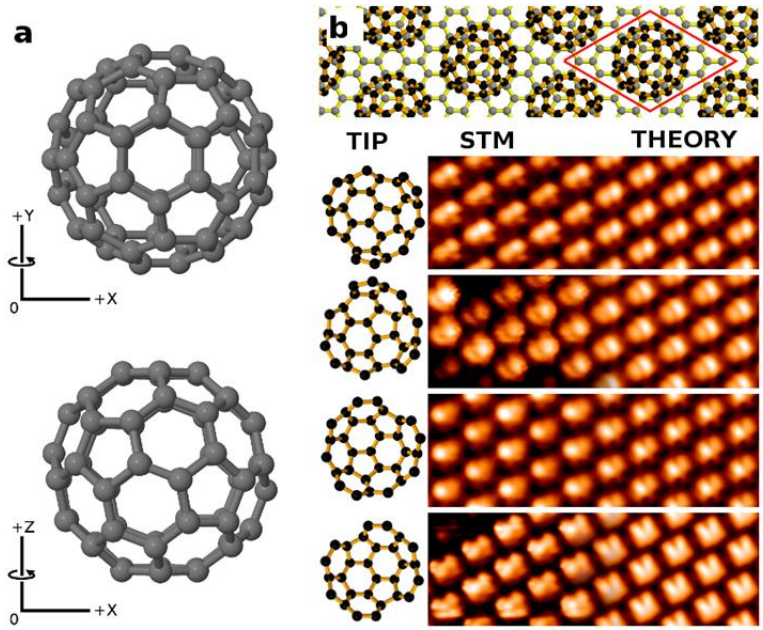

Figure 3 34: a. *A reference molecule used for the generation of C60 orientations. The rotations around the axes x and z define the nomenclature of the orientation, respectively, e.g. 70-30.* **b**.*Simulation of STM images on the model structure (top part) using a C60 tip in various orientations compared and matched with the experimentally observed types of contrast obtained on one C60 island on SLG.*

So far, we have pointed out the dominance of vdW intermolecular attraction between the C_{60} molecules on SLG. Due to a distinct decay and strength of this force one can expect a qualitatively different dynamical behavior of the molecules in this system. Movement of a single molecule away from the islands is highly unfavorable, because it has to overcome the energy barrier created by the vdW interactions with the nearest neighbors, but it will likely occur along the edge of an island. We observed such a process and it was enhanced by interactions with the scanning tip. We successfully attempted to observe C_{60} diffusion in an experiment by means of fast and reiterate scanning of the same region. Surprisingly, the islands that were not pinned by any defects (step edge, impurity, etc.) revealed a much faster mode of mass transport. **Figure 3 35** shows a sequence of tip-induced changes undergone by an island consisting of 50 C_{60} molecules. The observed area contains two pinned and thus rather stable islands A and C, plus a free and a very mobile island B which is apparently directed by the sense of the scanning, i.e., alternating upwards and downwards.

Importantly, the shape of A and C does not change strongly from one image to the next. That means the C_{60} migration along the island edges is slow and not many events are missed. A consequent interpretation of the movement of B is only possible by collective motion, as seen in the images between the time stamps 2:48 and 8:24, where both the shape of the island and the number of its molecules remain preserved. Island A serves only as a pivot point as B is changing its orientation with the substrate by 30°. By such rotation of the island, the unit cell is temporarily changed to $(\sqrt{3}x\sqrt{3})R30^{o}$ C_{60} coincident with a 7 × 7 SLG. A diffusion barrier of a C_{60}/SLG is inherently very low and the attractive force between the C_{60} caused by the vdW interactions can reach over distances of several SLG unit cells. Consequently, in the absence of a strong site-specific bonding mechanism, the cohesion force between C60 molecules is the crucial factor in the stability of the islands.

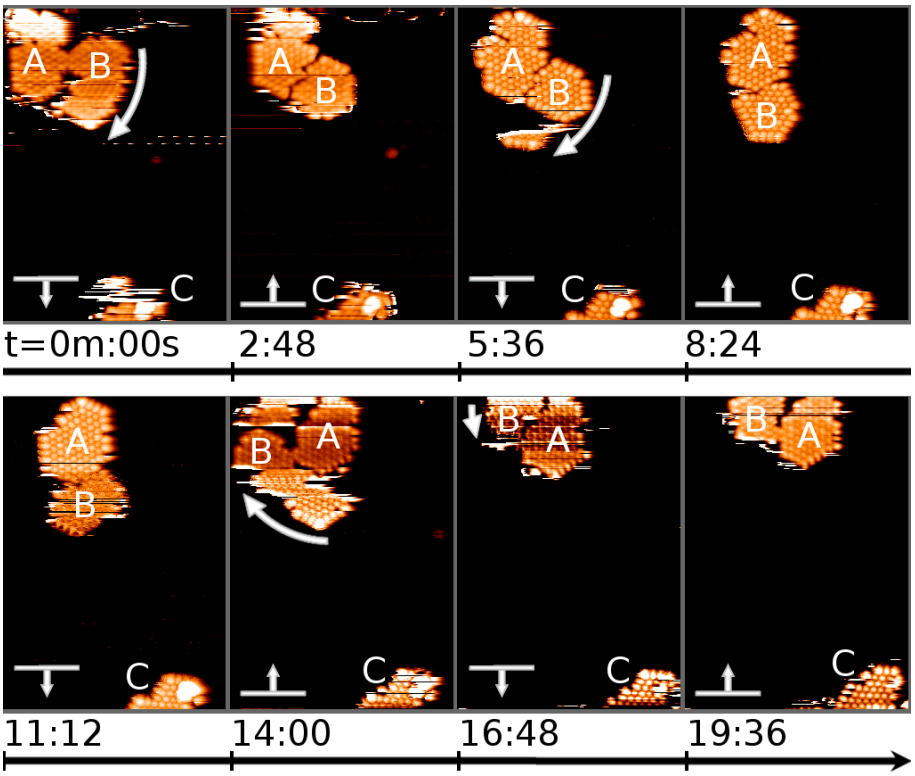

Figure 3 35: *Sequence of STM topographic images taken at 1500mV and 100pA on SLG with three islands of C_{60}. Islands A and C are pinned by a step edge and a surface defect respectively. The whole island B is undergoing*

movements (marked by curved arrows) that apparently conserve the overall shape between 2:48 and 8:24. The movements of the island are apparently correlated with the direction of scanning (denoted by vertical arrows with horizontal bars).

In the sequence in the **¡Error! No se encuentra el origen de la referencia. a-c** we present some evidence of single C_{60} diffusion along the island step edges. Most likely the molecules are migrating along the island boundaries as it was imaged in the **¡Error! No se encuentra el origen de la referencia. d**. The image shows only one half of a fullerene, repeatedly appearing above the edge of an island. The most likely interpretation of this effect is a movement of the C_{60} caused by the scanning probe, since the position and movements of the mobile molecule are correlated with the position and scanning direction of the probe. Logically a molecule in the corner position is less bound to the island and is more prone to movement. This mechanism leads to a gradual change of the island shape during the imaging, but may also occur spontaneously.

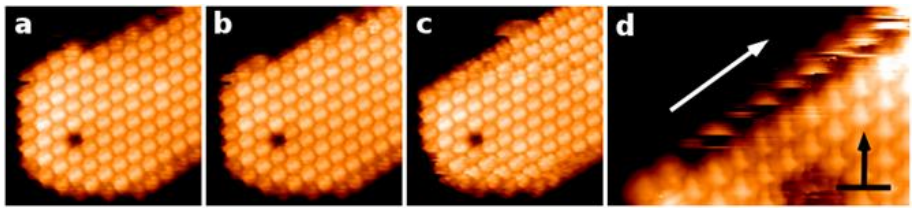

Figure 3 36: a-c. *12x12 nm^2 STM topography sequence showing transport of C_{60} molecules one-by-one.* **d**. *movement of one C_{60} along the island boundary (white arrow) caught in one 11x 7nm^2 image scanned from the bottom to the top (black arrow). All data taken at 600mV bias voltage and 100pA tunnelling current.*

In conclusion, the C_{60}/SLG behaves as a prototype of a decoupled adsorbate system governed by vdW forces. Advanced formalism, including vdW forces, is necessary for a successful determination of the correct adsorption geometry of the molecules. Our results show that the orientation of the molecule within the structure plays a major role in the total energy evaluation. The collective movement of small molecular islands demonstrates the dominant role of the vdW interactions in this system and the decoupling of the C_{60} from the substrate. The agreement of the experimental observation with the total energy and STM image calculations indicates the need for including vdW to account for the weak interactions in sp^2 compounds.

3.4. Conclusions

In this chapter we have studied by means of surface science techniques the different structures that appear onto the 6H-SiC(0001) surface. Form the silicon-rich 3x3 reconstruction and (√3x√3)R30º structures to the carbon-rich (6√3x6√3)R30º , graphene, and multilayer graphitic structures. For this purpose we have made use of high resolution STM images, XPS spectra, LEED and LEEM analysis, AFM, and theoretical calculations.

Graphene grows on top of a buffer layer with (6√3x6√3)R30ºquasi-periodicity in large terraces and in coexistence with (6√3x6√3)R30º regions and BLG terraces. The graphene produced by this method conserves its electronic properties very close to that of freestanding graphene. We have take profit of this situation to investigate the adsorption mechanisms of two different adsorbates on quasi free standing graphene – as opposed of G/metals where the underlying substrate normally plays a role.

In order to comprise the whole interaction range of possible adsorbates we have chosen a strongly interacting adsorbate – atomic hydrogen- and a weakly interacting adsorbate – fullerenes.

Atomic hydrogen on graphene forms cluster of a reduced number of atoms chemisorbed on top of carbon atoms of the graphene lattice. This chemisorption breaks the hybridization of the graphene carbon atoms from the original sp^2 towards sp^3, inducing the apparition of electronic states in the first and second neighbors of the hydrogenated carbon atom.

The atomic clusters, although chemisorbed, are very weakly bounded to the graphene surface and can be very easily evaporated under tip-induced desorption by highly interacting scanning conditions or voltage pulses.

On the other hand, the carbon pure C_{60} molecules deposited onto graphene at room temperature tend to escape from the graphene terraces and diffuse towards the, more reactive, (6√3x6√3)R30º regions. When C_{60} is deposited at 40K close-packed molecular islands are observed onto graphene. Observation of collective movements of fullerene islands and single molecules around the island edges points out the weak coupling to the substrate and the importance of the cohesion forces within this system.

The islands are exclusively bound by van der Waals interactions and the experimentally determined adsorption geometry of the molecules is

computationally confirmed only if van der Waals corrections are included in the calculation formalism. The relative orientation of fullerenes in their close-packed arrangement is found to be a crucial factor for determining the total energy.

Bibliography

1. Novoselov, K. S.; Geim, A. K.; Morozov, S. V.; Jiang, D.; Katsnelson, M. I.; Grigorieva, I. V.; Dubonos, S. V.; Firsov, A. A., Two-dimensional gas of massless Dirac fermions in graphene. *Nature* **2005,** *438* (7065), 197-200.
2. Schedin, F.; Geim, A. K.; Morozov, S. V.; Hill, E. W.; Blake, P.; Katsnelson, M. I.; Novoselov, K. S., Detection of individual gas molecules adsorbed on graphene. *Nature materials* **2007,** *6* (9), 652-5.
3. Geim, A. K.; Novoselov, K. S., The rise of graphene. *Nature materials* **2007,** *6* (3), 183-91.
4. Novoselov, K. S.; Geim, A. K.; Morozov, S. V.; Jiang, D.; Zhang, Y.; Dubonos, S. V.; Grigorieva, I. V.; Firsov, A. A., Electric Field Effect in Atomically Thin Carbon Films. *Science* **2004,** *306* (5696), 666-669.
5. Eda, G.; Fanchini, G.; Chhowalla, M., Large-area ultrathin films of reduced graphene oxide as a transparent and flexible electronic material. *Nature nanotechnology* **2008,** *3* (5), 270-4.
6. Bae, S.; Kim, H.; Lee, Y.; Xu, X.; Park, J. S.; Zheng, Y.; Balakrishnan, J.; Lei, T.; Kim, H. R.; Song, Y. I.; Kim, Y. J.; Kim, K. S.; Ozyilmaz, B.; Ahn, J. H.; Hong, B. H.; Iijima, S., Roll-to-roll production of 30-inch graphene films for transparent electrodes. *Nature nanotechnology* **2010,** *5* (8), 574-8.
7. Mårtensson, P.; Owman, F.; Johansson, L. I., Morphology, Atomic and Electronic Structure of 6H-SiC(0001) Surfaces. *physica status solidi (b)* **1997,** *202* (1), 501-528.
8. Berger, C.; Song, Z.; Li, T.; Li, X.; Ogbazghi, A. Y.; Feng, R.; Dai, Z.; Marchenkov, A. N.; Conrad, E. H.; First, P. N.; de Heer, W. A., Ultrathin Epitaxial Graphite: 2D Electron Gas Properties and a Route toward Graphene-based Nanoelectronics. *The Journal of Physical Chemistry B* **2004,** *108* (52), 19912-19916.
9. Berger, C.; Song, Z.; Li, X.; Wu, X.; Brown, N.; Naud, C.; Mayou, D.; Li, T.; Hass, J.; Marchenkov, A. N.; Conrad, E. H.; First, P. N.; de Heer, W. A., Electronic Confinement and Coherence in Patterned Epitaxial Graphene. *Science* **2006,** *312* (5777), 1191-1196.
10. Lin, Y.-M.; Dimitrakopoulos, C.; Jenkins, K. A.; Farmer, D. B.; Chiu, H.-Y.; Grill, A.; Avouris, P., 100-GHz Transistors from Wafer-Scale Epitaxial Graphene. *Science* **2010,** *327* (5966), 662.
11. Lin, Y.-M.; Valdes-Garcia, A.; Han, S.-J.; Farmer, D. B.; Meric, I.; Sun, Y.; Wu, Y.; Dimitrakopoulos, C.; Grill, A.; Avouris, P.; Jenkins, K. A., Wafer-Scale Graphene Integrated Circuit. *Science* **2011,** *332* (6035), 1294-1297.
12. Starke, U., Atomic Structure of Hexagonal SiC Surfaces. *physica status solidi (b)* **1997,** *202* (1), 475-499.
13. Heinz, K.; Bernhardt, J.; Schardt, J.; Starke, U., Functional surface reconstructions of hexagonal SiC. *Journal of Physics: Condensed Matter* **2004,** *16* (17), S1705.
14. Thomas, S., Passivation of hexagonal SiC surfaces by hydrogen termination. *Journal of Physics: Condensed Matter* **2004,** *16* (17), S1755.
15. Fabrice, A., Atomic scale study of the chemistry of oxygen, hydrogen and water at SiC surfaces. *Journal of Physics D: Applied Physics* **2007,** *40* (20), 6201.

16. Hass, J.; Heer, W. A. d.; Conrad, E. H., The growth and morphology of epitaxial multilayer graphene. *Journal of Physics: Condensed Matter* **2008,** *20* (32), 323202.
17. Starke, U.; Riedl, C., Epitaxial graphene on SiC(0001) and SiC(000-1): from surface reconstructions to carbon electronics. *Journal of Physics: Condensed Matter* **2009,** *21* (13), 134016.
18. Virojanadara, C.; Yakimova, R.; Zakharov, A. A.; Johansson, L. I., Large homogeneous mono-/bi-layer graphene on 6H–SiC(0 0 0 1) and buffer layer elimination. *Journal of Physics D: Applied Physics* **2010,** *43* (37), 374010.
19. Sprinkle, M.; Hicks, J.; Tejeda, A.; Taleb-Ibrahimi, A.; Fèvre, P. L.; Bertran, F.; Tinkey, H.; Clark, M. C.; Soukiassian, P.; Martinotti, D.; Hass, J.; Conrad, E. H., Multilayer epitaxial graphene grown on the SiC(000-1) surface; structure and electronic properties. *Journal of Physics D: Applied Physics* **2010,** *43* (37), 374006.
20. Riedl, C.; Coletti, C.; Starke, U., Structural and electronic properties of epitaxial graphene on SiC(0 0 0 1): a review of growth, characterization, transfer doping and hydrogen intercalation. *Journal of Physics D: Applied Physics* **2010,** *43* (37), 374009.
21. Emtsev, K. V.; Bostwick, A.; Horn, K.; Jobst, J.; Kellogg, G. L.; Ley, L.; McChesney, J. L.; Ohta, T.; Reshanov, S. A.; Rohrl, J.; Rotenberg, E.; Schmid, A. K.; Waldmann, D.; Weber, H. B.; Seyller, T., Towards wafer-size graphene layers by atmospheric pressure graphitization of silicon carbide. *Nature materials* **2009,** *8* (3), 203-7.
22. Van Bommel, A. J.; Crombeen, J. E.; Van Tooren, A., LEED and Auger electron observations of the SiC(0001) surface. *Surface Science* **1975,** *48* (2), 463-472.
23. Owman, F.; Mårtensson, P., The SiC(0001)6√3 × 6√3 reconstruction studied with STM and LEED. *Surface Science* **1996,** *369* (1–3), 126-136.
24. Li, L.; Tsong, I. S. T., Atomic structures of 6H□SiC (0001) and (0001̄) surfaces. *Surface Science* **1996,** *351* (1–3), 141-148.
25. Lee, B.; Han, S.; Kim, Y.-S., First-principles study of preferential sites of hydrogen incorporated in epitaxial graphene on 6H-SiC(0001). *Physical Review B* **2010,** *81* (7), 075432.
26. Inoue, M.; Kageshima, H.; Kangawa, Y.; Kakimoto, K., First-principles calculation of 0^{th}-layer graphene-like growth of C on SiC(0001). *Physical Review B* **2012,** *86* (8), 085417.
27. Chen, W.; Xu, H.; Liu, L.; Gao, X.; Qi, D.; Peng, G.; Tan, S. C.; Feng, Y.; Loh, K. P.; Wee, A. T. S., Atomic structure of the 6H–SiC(0 0 0 1) nanomesh. *Surface Science* **2005,** *596* (1–3), 176-186.
28. Rutter, G. M.; Guisinger, N. P.; Crain, J. N.; Jarvis, E. A. A.; Stiles, M. D.; Li, T.; First, P. N.; Stroscio, J. A., Imaging the interface of epitaxial graphene with silicon carbide via scanning tunneling microscopy. *Physical Review B* **2007,** *76* (23), 235416.
29. Riedl, C.; Coletti, C.; Iwasaki, T.; Zakharov, A. A.; Starke, U., Quasi-Free-Standing Epitaxial Graphene on SiC Obtained by Hydrogen Intercalation. *Physical review letters* **2009,** *103* (24), 246804.

30. Kim, Y.; Ihm, J.; Yoon, E.; Lee, G.-D., Dynamics and stability of divacancy defects in graphene. *Physical Review B* **2011,** *84* (7), 075445.
31. Varchon, F.; Mallet, P.; Veuillen, J. Y.; Magaud, L., Ripples in epitaxial graphene on the Si-terminated SiC(0001) surface. *Physical Review B* **2008,** *77* (23), 235412.
32. Qi, Y.; Rhim, S. H.; Sun, G. F.; Weinert, M.; Li, L., Epitaxial Graphene on SiC(0001): More than Just Honeycombs. *Physical review letters* **2010,** *105* (8), 085502.
33. Hu, T. W.; Ma, F.; Ma, D. Y.; Yang, D.; Liu, X. T.; Xu, K. W.; Chu, P. K., Evidence of atomically resolved 6 x 6 buffer layer with long-range order and short-range disorder during formation of graphene on 6H-SiC by thermal decomposition. *Applied Physics Letters* **2013,** *102* (17), 171910.
34. Iski, E. V.; Yitamben, E. N.; Gao, L.; Guisinger, N. P., Graphene at the Atomic-Scale: Synthesis, Characterization, and Modification. *Advanced Functional Materials* **2013,** *23* (20), 2554-2564.
35. Diaz, J.; Paolicelli, G.; Ferrer, S.; Comin, F., Separation of the sp^{3} and sp^{2} components in the C1s photoemission spectra of amorphous carbon films. *Physical Review B* **1996,** *54* (11), 8064.
36. Riedl, C.; Starke, U.; Bernhardt, J.; Franke, M.; Heinz, K., Structural properties of the graphene-SiC(0001) interface as a key for the preparation of homogeneous large-terrace graphene surfaces. *Physical Review B* **2007,** *76* (24), 245406.
37. Chang, C. S.; Tsong, I. S. T.; Wang, Y. C.; Davis, R. F., Scanning tunneling microscopy and spectroscopy of cubic β-SiC(111) surfaces. *Surface Science* **1991,** *256* (3), 354-360.
38. Brar, V. W.; Zhang, Y.; Yayon, Y.; Ohta, T.; McChesney, J. L.; Bostwick, A.; Rotenberg, E.; Horn, K.; Crommie, M. F., Scanning tunneling spectroscopy of inhomogeneous electronic structure in monolayer and bilayer graphene on SiC. *Applied Physics Letters* **2007,** *91* (12), 122102.
39. Park, C.; Yang, H.; Mayne, A. J.; Dujardin, G.; Seo, S.; Kuk, Y.; Ihm, J.; Kim, G., Formation of unconventional standing waves at graphene edges by valley mixing and pseudospin rotation. *Proceedings of the National Academy of Sciences* **2011,** *108* (46), 18622-18625.
40. Mallet, P.; Varchon, F.; Naud, C.; Magaud, L.; Berger, C.; Veuillen, J. Y., Electron states of mono- and bilayer graphene on SiC probed by scanning-tunneling microscopy. *Physical Review B* **2007,** *76* (4), 041403.
41. Kawai, S.; Kawakatsu, H., Surface-relaxation-induced giant corrugation on graphite (0001). *Physical Review B* **2009,** *79* (11), 115440.
42. Gross, L.; Moll, N.; Mohn, F.; Curioni, A.; Meyer, G.; Hanke, F.; Persson, M., High-Resolution Molecular Orbital Imaging Using a p-Wave STM Tip. *Physical review letters* **2011,** *107* (8), 086101.
43. Martínez, J. I.; Abad, E.; González, C.; Flores, F.; Ortega, J., Improvement of Scanning Tunneling Microscopy Resolution with H-Sensitized Tips. *Physical review letters* **2012,** *108* (24), 246102.

44. Abrami, A.; Barnaba, M.; Battistello, L.; Bianco, A.; Brena, B.; Cautero, G.; Chen, Q. H.; Cocco, D.; Comelli, G.; Contrino, S.; DeBona, F.; Di Fonzo, S.; Fava, C.; Finetti, P.; Furlan, P.; Galimberti, A.; Gambitta, A.; Giuressi, D.; Godnig, R.; Jark, W.; Lizzit, S.; Mazzolini, F.; Melpignano, P.; Olivi, L.; Paolucci, G.; Pugliese, R.; Qian, S. N.; Rosei, R.; Sandrin, G.; Savoia, A.; Sergo, R.; Sostero, G.; Tommasini, R.; Tudor, M.; Vivoda, D.; Wei, F. Q.; Zanini, F., Super ESCA: First beamline operating at ELETTRA. *Review of Scientific Instruments* **1995,** *66* (2), 1618-1620.
45. Virojanadara, C.; Syväjarvi, M.; Yakimova, R.; Johansson, L. I.; Zakharov, A. A.; Balasubramanian, T., Homogeneous large-area graphene layer growth on 6H-SiC(0001). *Physical Review B* **2008,** *78* (24), 245403.
46. de Lima, L. H.; de Siervo, A.; Landers, R.; Viana, G. A.; Goncalves, A. M. B.; Lacerda, R. G.; Häberle, P., Atomic surface structure of graphene and its buffer layer on SiC(0001): A chemical-specific photoelectron diffraction approach. *Physical Review B* **2013,** *87* (8), 081403.
47. Man, K. L.; Altman, M. S., Low energy electron microscopy and photoemission electron microscopy investigation of graphene. *Journal of Physics: Condensed Matter* **2012,** *24* (31), 314209.
48. Taisuke, O.; Farid El, G.; Aaron, B.; Jessica, L. M.; Konstantin, V. E.; Andreas, K. S.; Thomas, S.; Karsten, H.; Eli, R., Morphology of graphene thin film growth on SiC(0001). *New Journal of Physics* **2008,** *10* (2), 023034.
49. Kim, S.; Ihm, J.; Choi, H. J.; Son, Y.-W., Origin of Anomalous Electronic Structures of Epitaxial Graphene on Silicon Carbide. *Physical review letters* **2008,** *100* (17), 176802.
50. Nemec, L.; Blum, V.; Rinke, P.; Scheffler, M., Thermodynamic Equilibrium Conditions of Graphene Films on SiC. *Physical review letters* **2013,** *111* (6), 065502.
51. Forbeaux, I.; Themlin, J. M.; Debever, J. M., Heteroepitaxial graphite on 6H-SiC(0001): Interface formation through conduction-band electronic structure. *Physical Review B* **1998,** *58* (24), 16396-16406.
52. Norimatsu, W.; Kusunoki, M., Transitional structures of the interface between graphene and 6H–SiC (0 0 0 1). *Chemical Physics Letters* **2009,** *468* (1–3), 52-56.
53. Huang, H.; Chen, W.; Chen, S.; Wee, A. T. S., Bottom-up Growth of Epitaxial Graphene on 6H-SiC(0001). *ACS nano* **2008,** *2* (12), 2513-2518.
54. Lauffer, P.; Emtsev, K. V.; Graupner, R.; Seyller, T.; Ley, L.; Reshanov, S. A.; Weber, H. B., Atomic and electronic structure of few-layer graphene on SiC(0001) studied with scanning tunneling microscopy and spectroscopy. *Physical Review B* **2008,** *77* (15), 155426.
55. Hornekær, L.; Šljivančanin, Ž.; Xu, W.; Otero, R.; Rauls, E.; Stensgaard, I.; Lægsgaard, E.; Hammer, B.; Besenbacher, F., Metastable Structures and Recombination Pathways for Atomic Hydrogen on the Graphite (0001) Surface. *Physical review letters* **2006,** *96* (15), 156104.
56. Hornekær, L.; Rauls, E.; Xu, W.; Šljivančanin, Ž.; Otero, R.; Stensgaard, I.; Lægsgaard, E.; Hammer, B.; Besenbacher, F., Clustering of Chemisorbed H(D) Atoms on the Graphite (0001) Surface due to Preferential Sticking. *Physical review letters* **2006,** *97* (18), 186102.

57. Hornekær, L.; Xu, W.; Otero, R.; Lægsgaard, E.; Besenbacher, F., Long range orientation of meta-stable atomic hydrogen adsorbate clusters on the graphite(0 0 0 1) surface. *Chemical Physics Letters* **2007,** *446* (4–6), 237-242.
58. Balog, R.; Jørgensen, B.; Wells, J.; Lægsgaard, E.; Hofmann, P.; Besenbacher, F.; Hornekær, L., Atomic Hydrogen Adsorbate Structures on Graphene. *Journal of the American Chemical Society* **2009,** *131* (25), 8744-8745.
59. Guisinger, N. P.; Rutter, G. M.; Crain, J. N.; First, P. N.; Stroscio, J. A., Exposure of Epitaxial Graphene on SiC(0001) to Atomic Hydrogen. *Nano letters* **2009,** *9* (4), 1462-1466.
60. Balog, R.; Jorgensen, B.; Nilsson, L.; Andersen, M.; Rienks, E.; Bianchi, M.; Fanetti, M.; Laegsgaard, E.; Baraldi, A.; Lizzit, S.; Sljivancanin, Z.; Besenbacher, F.; Hammer, B.; Pedersen, T. G.; Hofmann, P.; Hornekaer, L., Bandgap opening in graphene induced by patterned hydrogen adsorption. *Nature materials* **2010,** *9* (4), 315-9.
61. Ulstrup, S.; Nilsson, L.; Miwa, J. A.; Balog, R.; Bianchi, M.; Hornekær, L.; Hofmann, P., Electronic structure of graphene on a reconstructed Pt(100) surface: Hydrogen adsorption, doping, and band gaps. *Physical Review B* **2013,** *88* (12), 125425.
62. Watcharinyanon, S.; Virojanadara, C.; Osiecki, J. R.; Zakharov, A. A.; Yakimova, R.; Uhrberg, R. I. G.; Johansson, L. I., Hydrogen intercalation of graphene grown on 6H-SiC(0001). *Surface Science* **2011,** *605* (17–18), 1662-1668.
63. SljivanCanin, Z.; Rauls, E.; Hornekaer, L.; Xu, W.; Besenbacher, F.; Hammer, B., Extended atomic hydrogen dimer configurations on the graphite(0001) surface. *The Journal of chemical physics* **2009,** *131* (8), 084706.
64. Casolo, S.; Lovvik, O. M.; Martinazzo, R.; Tantardini, G. F., Understanding adsorption of hydrogen atoms on graphene. *The Journal of chemical physics* **2009,** *130* (5), 054704.
65. Ferro, Y.; Teillet-Billy, D.; Rougeau, N.; Sidis, V.; Morisset, S.; Allouche, A., Stability and magnetism of hydrogen dimers on graphene. *Physical Review B* **2008,** *78* (8), 085417.
66. McKay, H.; Wales, D. J.; Jenkins, S. J.; Verges, J. A.; de Andres, P. L., Hydrogen on graphene under stress: Molecular dissociation and gap opening. *Physical Review B* **2010,** *81* (7), 075425.
67. Huang, L. F.; Cao, T. F.; Gong, P. L.; Zeng, Z.; Zhang, C., Tuning the adatom-surface and interadatom interactions in hydrogenated graphene by charge doping. *Physical Review B* **2012,** *86* (12), 125433.
68. Šljivančanin, Ž.; Andersen, M.; Hornekær, L.; Hammer, B., Structure and stability of small H clusters on graphene. *Physical Review B* **2011,** *83* (20), 205426.
69. Sofo, J. O.; Chaudhari, A. S.; Barber, G. D., Graphane: A two-dimensional hydrocarbon. *Physical Review B* **2007,** *75* (15), 153401.
70. Tsetseris, L.; Pantelides, S. T., Molecular doping of graphene with ammonium groups. *Physical Review B* **2012,** *85* (15), 155446.
71. Gmitra, M.; Kochan, D.; Fabian, J., Spin-Orbit Coupling in Hydrogenated Graphene. *Physical review letters* **2013,** *110* (24), 246602.

72. Sessi, P.; Guest, J. R.; Bode, M.; Guisinger, N. P., Patterning graphene at the nanometer scale via hydrogen desorption. *Nano letters* **2009,** *9* (12), 4343-7.
73. Stadler, C.; Hansen, S.; Kroger, I.; Kumpf, C.; Umbach, E., Tuning intermolecular interaction in long-range-ordered submonolayer organic films. *Nat Phys* **2009,** *5* (2), 153-158.
74. Dickerson, P. N.; Hibberd, A. M.; Oncel, N.; Bernasek, S. L., Hydrogen-Bonding versus van der Waals Interactions in Self-Assembled Monolayers of Substituted Isophthalic Acids. *Langmuir* **2010,** *26* (23), 18155-18161.
75. Hanke, F.; Haq, S.; Raval, R.; Persson, M., Heat-to-Connect: Surface Commensurability Directs Organometallic One-Dimensional Self-Assembly. *ACS nano* **2011,** *5* (11), 9093-9103.
76. Ruiz, V. G.; Liu, W.; Zojer, E.; Scheffler, M.; Tkatchenko, A., Density-Functional Theory with Screened van der Waals Interactions for the Modeling of Hybrid Inorganic-Organic Systems. *Physical review letters* **2012,** *108* (14), 146103.
77. Kroto, H. W.; Heath, J. R.; O'Brien, S. C.; Curl, R. F.; Smalley, R. E., C60: Buckminsterfullerene. *Nature* **1985,** *318* (6042), 162-163.
78. Shin, H.; O'Donnell, S. E.; Reinke, P.; Ferralis, N.; Schmid, A. K.; Li, H. I.; Novaco, A. D.; Bruch, L. W.; Diehl, R. D., Floating two-dimensional solid monolayer of C_{60} on graphite. *Physical Review B* **2010,** *82* (23), 235427.
79. Moriarty, P. J., Fullerene adsorption on semiconductor surfaces. *Surface Science Reports* **2010,** *65* (7), 175-227.
80. Lu, J.; Yeo, P. S. E.; Zheng, Y.; Yang, Z.; Bao, Q.; Gan, C. K.; Loh, K. P., Using the Graphene Moiré Pattern for the Trapping of C60 and Homoepitaxy of Graphene. *ACS nano* **2011,** *6* (1), 944-950.
81. Li, G.; Zhou, H. T.; Pan, L. D.; Zhang, Y.; Mao, J. H.; Zou, Q.; Guo, H. M.; Wang, Y. L.; Du, S. X.; Gao, H.-J., Self-assembly of C[sub 60] monolayer on epitaxially grown, nanostructured graphene on Ru(0001) surface. *Applied Physics Letters* **2012,** *100* (1), 013304.
82. Cho, J.; Smerdon, J.; Gao, L.; Süzer, Ö.; Guest, J. R.; Guisinger, N. P., Structural and Electronic Decoupling of C60 from Epitaxial Graphene on SiC. *Nano letters* **2012,** *12* (6), 3018-3024.
83. Dappe, Y. J.; Ortega, J.; Flores, F., Intermolecular interaction in density functional theory: Application to carbon nanotubes and fullerenes. *Physical Review B* **2009,** *79* (16), 165409.
84. Dappe, Y. J.; Basanta, M. A.; Flores, F.; Ortega, J., Weak chemical interaction and van der Waals forces between graphene layers: A combined density functional and intermolecular perturbation theory approach. *Physical Review B* **2006,** *74* (20), 205434.
85. Lewis, J. P.; Jelínek, P.; Ortega, J.; Demkov, A. A.; Trabada, D. G.; Haycock, B.; Wang, H.; Adams, G.; Tomfohr, J. K.; Abad, E.; Wang, H.; Drabold, D. A., Advances and applications in the FIREBALLab initio tight-binding molecular-dynamics formalism. *physica status solidi (b)* **2011,** *248* (9), 1989-2007.
86. Chen, W.; Zhang, H. L.; Xu, H.; Tok, E. S.; Loh, K. P.; Wee, A. T. S., C60 on SiC Nanomesh. *The Journal of Physical Chemistry B* **2006,** *110* (43), 21873-21881.

87. Chen, W.; Chen, S.; Zhang, H. L.; Xu, H.; Qi, D. C.; Gao, X. Y.; Loh, K. P.; Wee, A. T. S., Probing the interaction at the C60–SiC nanomesh interface. *Surface Science* **2007,** *601* (14), 2994-3002.
88. Liu, H.; Reinke, P., C[sub 60] thin film growth on graphite: Coexistence of spherical and fractal-dendritic islands. *The Journal of chemical physics* **2006,** *124* (16), 164707.
89. Lu, X.; Grobis, M.; Khoo, K. H.; Louie, S. G.; Crommie, M. F., Charge transfer and screening in individual C_{60} molecules on metal substrates: A scanning tunneling spectroscopy and theoretical study. *Physical Review B* **2004,** *70* (11), 115418.
90. Schull, G.; Berndt, R., Orientationally Ordered (7×7) Superstructure of C_{60} on Au(111). *Physical review letters* **2007,** *99* (22), 226105.
91. Schull, G.; Frederiksen, T.; Brandbyge, M.; Berndt, R., Passing Current through Touching Molecules. *Physical review letters* **2009,** *103* (20), 206803.
92. Heinrich, B. W.; Rastei, M. V.; Choi, D. J.; Frederiksen, T.; Limot, L., Engineering Negative Differential Conductance with the Cu(111) Surface State. *Physical review letters* **2011,** *107* (24), 246801.
93. Langreth, D. C.; Dion, M.; Rydberg, H.; Schröder, E.; Hyldgaard, P.; Lundqvist, B. I., Van der Waals density functional theory with applications. *International Journal of Quantum Chemistry* **2005,** *101* (5), 599-610.
94. Tkatchenko, A.; Scheffler, M., Accurate Molecular Van Der Waals Interactions from Ground-State Electron Density and Free-Atom Reference Data. *Physical review letters* **2009,** *102* (7), 073005.
95. Lebègue, S.; Harl, J.; Gould, T.; Ángyán, J. G.; Kresse, G.; Dobson, J. F., Cohesive Properties and Asymptotics of the Dispersion Interaction in Graphite by the Random Phase Approximation. *Physical review letters* **2010,** *105* (19), 196401.
96. Varchon, F.; Feng, R.; Hass, J.; Li, X.; Nguyen, B. N.; Naud, C.; Mallet, P.; Veuillen, J. Y.; Berger, C.; Conrad, E. H.; Magaud, L., Electronic Structure of Epitaxial Graphene Layers on SiC: Effect of the Substrate. *Physical review letters* **2007,** *99* (12), 126805.
97. Blanco, J. M.; Flores, F.; Pérez, R., STM-theory: Image potential, chemistry and surface relaxation. *Progress in Surface Science* **2006,** *81* (10–12), 403-443.

General conclusions

This thesis aims to unravel the atomic scale structures appearing on epitaxial graphene systems and to understand the stable atomic-scale configurations of sp^2 carbon structures appearing on the surface on single crystal samples. For this purpose we have made use of two independent substrates, the silicon carbide (SiC) hexagonal surface and the Pt(111) surface. Both of them are suitable for growing epitaxial graphene, but the growth methodology differs for each surface. Epitaxial growth on SiC(0001) surface is successfully achieved by annealing the samples at temperatures around 1550K. Annealing above this temperature results in multilayer growth. This material contains a significant amount of carbon and no external precursors are needed for graphene nucleation or growth. On the other hand Pt(111) surface needs temperatures around 1100K and an external source of carbon in order to catalyze the growth of graphene. This can be done either by using carbon containing molecular precursors or by surface segregation of embedded carbon in the bulk. In the present thesis only the molecular precursor methodology was studied. Under this methodology the total graphene coverage can be controlled by regulating the amount of precursors deposited on the surface.

Graphene on Pt(111) grows forming islands with several orientations and sizes. Every of these orientations forms a different superstructure known as Moiré patterns. We have investigated from an experimental point of view the total number of Moiré superstructures on Pt(111) and analyzed all the possible Moiré superstructures in the G/Pt(111) system with the help of a model. The model predicts the existence of 22 preferred graphene orientations forming 15 different Moiré superstructures. The model predictions are in good agreement with the experimental observations and the existing scientific literature. Among all the possible Moirés we have performed a combined theoretical-experimental exhaustive characterization of the two smallest reconstructions, this is $(\sqrt{3}x\sqrt{3})R30^{o}$ and $(\sqrt{7}x\sqrt{7})R19^{o}$, and found that the former can be explained in terms of an ordered vacancy network in the outermost Pt layer and graphene relatively strongly bound to it while the latter is described as a van der Waals mediated flat sheath on top of the Pt(111) surface.

Covalently bound graphene-Pt(111) edges have an important role in the determination of stable orientations. The bonding region between carbon and Pt normally forms crystalline one-dimensional heterostructures that present the nucleation seed for graphene growth. We have found that graphene tends to end in zig-zag configuration and this is also true for the G-Pt bonding region, therefore the larger part of strain relaxation takes

place on the Pt side of the heterostructure. We have performed a full characterization of the (√7x√7)R19º-Pt. The electronic characterization brings a unexpected result: the apparition of an exotic 1D electronic state in one of the two graphene sublattices.

0D,1D and 2D graphene defects are the preferred relaxing mechanism for the strain raised from mismatch accumulation in the Moiré superstructures on G/Pt(111). The 0D defects include missing C atoms and inclusion of foreign atomic species into the graphene lattice as well as multiatomic rearrangements. The 1D defects include graphene-graphene pollycristalline borders and graphene-metal heterostructures. And the 2D defects include surface carbides and graphene folds and nanobubbles.

Graphene on SiC(0001) behaves as quasi free-standing graphene and presents very exotic electronic behavior such as intervalley scattering near defects and tunneling transparency under bias voltages far from the Fermi level. We have made use of the G/SiC(0001) to test the reactivity of graphene upon deposition of adsorbates.

Hydrogen on G/SiC(0001) covalently bounds on top of carbon atoms belonging to the graphene lattice and break the hybridization of these surface atoms from the original sp^2 towards an sp^3 orbital rearrangement. It chemisorbs on graphene forming dimmers, trimmers and small 2D clusters with geometrical configurations confined by the honeycomb lattice of the substrate. These adsorbates can be easily removed from the surface by annealing at relatively low temperatures (800K) and even by simple STM scanning or voltage pulses. Upon H adsorption the first and second carbon neighbors get electronically modified inducing the apparition of intrinsically extended structures, making very difficult the exact determination of the atomic position of the chemisorbed H atoms. This system is a prototype of strong interacting graphene adsorbate.

C_{60}/G/SiC(0001) is a prototype of a weakly interacting adsorbates. The molecules deposited at 300K tend to escape from the graphene regions and end immobilized on the (6√3x6√3)R30º terraces. When C_{60} is deposited at 40K hexagonal close-packed (4x4) fullerene islands are observed onto graphene. These molecules are very weakly bounded and result very mobile under STM experiments. DFT calculations show that the molecular islands are mainly bound by van der Waals interactions and reproduce the most stable adsorption site to be 6:6/30º hollow. The intermolecular interaction

and the relative orientation of fullerenes is found to be a driving factor in the determination of the total energy.

Conclusiones generales

Esta tesis tiene como objetivo estudiar las estructuras a escala atómica que aparecen en los sistemas de grafeno epitaxial asi como comprender las configuraciones estables de carbono sp^2 ocurrentes en superficies monocristalinas. Para ello se ha hecho uso de dos sustratos independientes, el carburo de silicio (SiC) y la superficie hexagonal Pt(111). Ambos son adecuados para el desarrollo de grafeno epitaxial , pero la metodología de crecimiento difiere para cada una de las superficies. El crecimiento epitaxial sobre carburo de silicio en la superficie (0001) se logra con éxito por el calentamiento de las muestras a temperaturas alrededor de 1550K . El calentamiento por encima de esta temperatura da como resultado el crecimiento de múltiples capas de grafeno. Este material contiene una cantidad significativa de carbono y no es necesario el uso de precursores externos para la nucleación o el crecimiento de grafeno. Por otro lado, Pt(111) necesita temperaturas de alrededor de 1100K y una fuente externa de carbono con el fin de catalizar el crecimiento de grafeno en su superficie. Esto se puede hacer ya sea mediante el uso del carbono contenido en precursores moleculares o por la segregación hacia la superficie del carbono embebido en el volumen del metal. En la presente tesis sólo se estudió la metodología que utiliza precursores moleculares. En esta metodología la cobertura total de grafeno puede ser controlada mediante la regulación de la cantidad de precursores depositados sobre la superficie.

El grafeno sobre Pt (111) crece formando islas con varias orientaciones. Cada una de estas orientaciones forma una superestructura diferente conocidas como Moirés. Estas estructuras aparecen por la interferencia electrónica entre el sustrato y la sobrecapa, y la corrugación observada combina efectos electrónicos y topográficos. Desde un punto de vista experimental, el número total de superestructuras Moiré sobre Pt(111) es difícil de determinar por lo que se ha hecho uso de un modelo original depara predecir y analizar todas las posibles superestructuras Moiré que apaecen en el sistema G/Pt(111). El modelo se basa en la búsqueda de las posiciones de red con mejor coincidencia entre una hoja de grafeno girada en cualquier ángulo sobre la parte superior de una superficie de Pt(111). El modelo predice la existencia de 22 orientaciones preferentes de grafeno que forman 15 diferentes superestructuras Moiré distintas, esto se debe a que algunas simetrías internas hacen aparecer el mismo Moiré para dos ángulos diferentes. Las predicciones del modelo se encuentran en buen acuerdo con las observaciones experimentales y de la literatura científica existente. Entre todos los Moirés posibles hemos realizado una caracterización exhaustiva teórico-experimental de las dos reconstrucciones más pequeños , que son $(\sqrt{3}x\sqrt{3})$ R30 ^{o} y $(\sqrt{7}x\sqrt{7})$ R19 ^{o}. La

(√3x√3) R30 º puede ser explicada en términos de una red de vacantes ordenadas en la capa más externa de la superficie de Pt y una capa de grafeno fuertemente unida a ella, mientras que (√7x√7) R19 º se describe como una de red de grafeno plana en la parte superior de la superficie de Pt con una interacción mayormente mediada por fuerzas van der Waals.

Los bordes grafeno–Pt(111) covalentemente unidos tienen un papel importante en la determinación de las orientaciones estables . La región de enlace entre el carbono y Pt forma normalmente heteroestructuras unidimensionales cristalinas que representan las zonas de nucleación para el crecimiento de grafeno. Estos bordes también se pueden determinar a partir de nuestro modelo. Hemos encontrado que el grafeno tiende a terminar en zig-zag , esto también es cierto para la región de unión del grafeno con el Pt y, por lo tanto, la mayor parte de la relajación se lleva a cabo en el lado del Pt de la heteroestructura. Hemos llevado a cabo una caracterización completa de la heteroestructura (√7x√7) R19 º-Pt mediante la comparación de imágenes de STM de alta resolución con los cálculos DFT. Los resultados muestran que para esta interfaz en particular, la relajación tienen lugar en el lado del Pt mediante el reajuste de las posiciones de red del Pt y mediante la recolocación de los átomos de Pt exteriores del escalón muy lejos de las posiciones originales. La caracterización electrónica trae un resultado inesperado: la aparición de un estado electrónico 1D en una de las dos subredes de grafeno.

Los defectos en grafeno de 0D , 1D y 2D son el mecanismo de relajación preferido para la capa. Este estrés es debido a la acumulación de falta de coincidencia en las superestructuras Moiré de G/Pt(111). Los defectos 0D pueden ser, entre otros, vacantes atómicas de carbono o la inclusión de especies atómicas extraños en la red de grafeno, así como el reordenamientos de muchos atomos en una zona reducida de la red. Los defectos 1D incluyen bordes policristalinos grafeno-grafeno y heteroestructuras grafeno-metal. Y los defectos 2D incluyen carburos de superficie o los pliegues de grafeno como las nanoburbujas.

El grafeno sobre SiC(0001) se comporta como grafeno cuasi-libre y presenta un comportamiento electrónico muy exótico con efectos elctronicos tales como la dispersión entre valles cerca de defectos o la transparencia túnel bajo voltajes lejos del nivel de Fermi. Esta estructura normalmente coexiste con regiones con la reconstrucción (6√3x6√3)R30º y regiones de bicapa de grafeno en forma de terrazas con tamaños entre 10 y 100nm. La superestructura (6√3x6√3)R30º consiste en una capa de carbono

con hibridación sp^2 en panal de abeja con algunos de sus átomos unidos covalentemente a la fila superior de atomos de Si subyacentes. Esta estructura presenta una periodicidad cuasi-6x6 si se investiga con STM y siempre está por debajo de las regiones de grafeno. Hemos hecho uso de la superficies G/SiC(0001) para probar la reactividad del grafeno con respecto a la deposición de adsorbatos sencillos.

El Hidrógeno sobre G/SiC(0001) se enlaza covalentemente sobre la parte superior de los átomos de carbono pertenecientes a la red de grafeno rompiendo su hibridación desde la sp^2 original hacia un reordenamiento orbital en configuración sp^3. El hidrógeno se quemisorbe formando dímeros trímeros y pequeños clústeres bidimensionales sobre el grafeno 2D cuyas configuraciones geométricas están confinados por el sustrato. Estos adsorbatos se pueden eliminar fácilmente de la superficie calnetando a temperaturas relativamente bajas (800K) y mediante el uso de STM con pulsos de voltaje. Hemos estudiado desde una perspectiva teórica las geometrías de adsorción más estables para la menor de todas estas estructuras, el dímero, y hemos encontrado algunas dificultades intrínsecas para confrontar las imágenes de STM simuladas con las experimentales. La adsorción de hidrógeno modifica electrónicamente la estructura de los primero y segundo vecinos de, lo que hace muy difícil la determinación exacta de la posición atómica de los átomos sobre los cuales el hidrógeno está quimisorbido Este sistema es un prototipo de una fuerte interacción adsorbato grafeno.

El C_{60}/G/SiC(0001) es un prototipo de sistema de adsorbatos débilmente interactuantes. Las moléculas depositadas a 300K tienden a escapar de las regiones de grafeno y acaban ancladas sobre las terrazas de$(6\sqrt{3}x6\sqrt{3})R30^{o}$. Cuando los C_{60} se depositan a 40K se observan islas de fullerenos hexagonales sobre el grafeno. Estas moléculas están muy débiles unidas al substrato y resultan muy fáciles de mover con la punta del STM. Los cálculos DFT muestran que las islas moleculares están unidas exclusivamente por interacciones van der Waals. La geometría de adsorción de las moléculas se confirma computacionalmente sólo si las correcciones van der Waals se incluyen en el formalismo de cálculo. La interacción intermolecular y la orientación relativa de los fullerenos resulta ser un factor determinante en la determinación de la energía total del sistema.